Hydrological simulations at basin scale using distributed model and remote sensing with a focus on soil moisture

By

Ageel Ibrahim Bushara Ahmed

A thesis submitted in partial fulfillment
of the requirements for the degree
of Doctor of Philosophy

in

The Faculty of Engineering
Department of Civil and Environmental Engineering

The University of Trento
April 2011

Doctoral thesis in Environmental Engineering (XXIII cycle)
Defended in April 2011 at the Faculty of Engineering of the University of Trento

Supervisor: Prof Riccardo Rigon (University of Trento, Italy)
Co-supervisor: Prof Mekonnen Gebremichael (University of Connecticut, USA)
External supervisor: Prof Christa D. Peters-Lidard (NASA- GSFC, USA)

Examination Committee

Vincenzo Casulli (University of Trento)
Paolo Burlando (ETH Zürich)
Vladimir Nikora (University of Aberdeen)

University of Trento
Trento, Italy
April 2011

Abstract

Remotely-sensed precipitation and soil moisture products are becoming increasingly important sources of information in earth science system. However, there are still high degree of uncertainties inherited in remotely-sensed precipitation and soil moisture products, and limited studies have focused on evaluation of these products.

In this study, GEOtop model (Rigon et al. 2006), which is physically-based distributed hydrological model, is used to assess the use of remotely-sensed precipitation and soil moisture products for hydrological applications. The study area is Little Washita watershed (583 km^2), Oklahoma, USA. To assess these products, the model has to be first calibrated and validated at different locations in the watershed using extensive ground-based measurements. The Southern Great Plains 1997 (SGP97) and SGP99 Hydrology Experiment are used for model calibration and validation, respectively. The model is reasonably calibrated and validated at watershed scale at different locations in the watershed for: heat fluxes, soil temperature profiles, soil moisture profiles, and streamflows.

Regarding soil moisture evolution, we studied the spatial variability of the near-surface soil moisture from GEOtop simulations and estimates from Electronically Scanned Thinned Array Radiometer (ESTAR). Results show that GEOtop simulations and ESTAR estimates show very different magnitude and spatial patterns of near-surface soil moisture. Spatial patterns derived from GEOtop simulations are in agreement with the previous findings obtained from the same study area using ground-based measurements of soil moisture and theoretical model simulations. We conclude that GEOtop simulation results are more accurate and that ESTAR estimates are not a reliable source of data for characterizing the spatial variability of near-surface soil moisture. GEOtop simulations show that the spatial distribution of near-surface soil moisture is highly controlled by soil texture and river network. Furthermore, we investigated the effect of vegetation, surface roughness, and topography on ESTAR. Results show that there are insignificant effects of vegetation except for interception, surface roughness, and topography on ESTAR. In addition, we investigated the scaling properties of near-surface soil moisture. Results show that near-surface soil moisture has multiscaling behaviour.

On the other hand, spatial soil moisture patterns are studied using geostatistical techniques: Ordinary kriging, external drift kriging and conditional Gaussian simulations (CGSs). Krigings show that soil moisture patterns in the watershed are highly controlled by gradient and cosine aspect. All CGSs clearly show soil moisture patterns. Spatial soil moisture patterns produced by CGSs are much better than the patterns reproduced by kriging algorithms.

Regarding remotely-sensed precipitation products, we have investigated the utility of these products for hydrological simulations during non-winter seasons. Results show that all remotely-sensed precipitation products (Climate Prediction Center's morphing technique (CMORPH), Precipitation Estimation from Remotely Sensed Information using Artificial Neural Networks - Cloud Classification System (PERSIANN-CCS)- and Next Generation Weather Radar (NEXRAD Stage III)) are fairly reproducing the streamflows, but CMORPH often overestimates streamflows. Thus it concluded that all the above mentioned remotely-sensed precipitation products have value for streamflow simulations.

Keywords:

Distributed hydrological model; GEOtop, passive microwave radiometer soil moistures (ESTAR), space-time soil moisture variability, remotely-sensed precipitation, Little Washita watershed.

Acknowledgements

First and foremost, I'm greatly indebted to my supervisors, Prof Riccardo Rigon and Prof Mekonnen Gebremichael, for their supervision and scientific inputs to the research, without whom, this research would not have been possible. Special thanks go to Prof Thomas M. Over for his insights and for his valuable comments. Also special thanks go to Prof Christa D. Peters-Lidard, who acts as external supervisor of my research, for her valuable and useful comments.

Thanks to the GEOtop and to the JGRASS communities: Giacomo, Stefano, Emanuele, Matteo, Daniele, Fabrizio, Han, Cristiano, Ilaria, and Giuseppe for their friendship and support. Special thanks go to Feyera, Menberu, and Dawit, for their help and comments on this research, and for their nice accompany when I was at the University of Connecticut.

I would like to take this opportunity to thank the University of Trento for granting me the scholarship. Also I would like to say thanks to the staff of the University of Trento and to my colleagues and friends who have given me support and help during my research.

Last but not least, I would like to express my gratitude to my wife and my daughter for their patience, support and encouragement throughout the study.

Table of Contents

Abstract ..... **I**
Acknowledgements ..... **III**

Table of Contents ..... **V**

List of figures ..... **VII**

List of tables ..... **XIII**

1 Introduction **1**
1.1 Motivation **1**
1.2 Soil moisture **1**
1.3 Remotely-sensed precipitation **2**
1.4 Objective **3**
1.5 The structure **4**
1.6 Study area **5**
1.7 The GEOtop model **6**

2 Model calibration using Southern Great Plains 1997 (SGP97) hydrology experiment dataset **9**
2.1 Dataset **9**
2.2 Atmospheric forcing to the GEOtop model **10**
2.3 Model initialization and setup **10**
2.3.1 Initial and boundary conditions and parameters derived from literature 10
2.3.2 Procedure of model spin-up 12
2.4 Performance statistics **15**
2.5 Results and discussions **15**
2.5.1 Simulated heat fluxes 15
2.5.2 Simulated soil temperatures 16
2.5.3 Simulated streamflows 20
2.5.4 Simulated soil moistures 21
2.6 Conclusion **25**

3 Model validation using Southern Great Plains 1999 (SGP99) hydrology experiment dataset **27**
3.1 Model initialization and setup **27**
3.2 Results and discussions **29**
3.2.1 Simulated surface fluxes 29
3.2.2 Simulated soil temperatures 31
3.2.3 Simulated soil moistures 32
3.2.4 Simulated streamflows 34
3.3 Conclusion **35**

4 Simulated and ESTAR soil moisture patterns during SGPs **37**
4.1 Simulated and ESTAR soil moisture patterns during SGP97 ..... **37**
4.1.1 Comparison between simulated and ESTAR soil moisture patterns 37
4.1.2 The relationships vegetation, surface roughness, topography, and ESTAR soil moisture 44
4.1.3 The relationships brightness temperatures, soil temperatures and soil moistures 49
4.2 Simulated and ESTAR soil moisture patterns during SGP99 ..... **59**
4.2.1 Comparison between simulated and ESTAR soil moisture patterns 59
4.2.2 The relationships vegetation, surface roughness, topography, and ESTAR soil moisture 61

4.3 Conclusion **64**

5 Characterization of space-time soil moisture variability during SGPs **67**
5.1 Statistical characterization of soil moisture **67**
5.1.1 Soil moisture frequency distributions 67
5.1.2 Standard deviation, coefficient of variation, and skewness 71
5.1.3 Kurtosis of soil moisture 74
5.2 Scaling analysis of simulated and ESTAR soil moistures **76**
5.3 Soil moisture variograms **81**
5.4 Re-thinking the soil moisture assessment in SGP experiments **84**
5.5 Conclusion **85**

6 Comparison of the geostatistical techniques with dynamical modeling **87**
6.1 Setup of soil moisture measurement network **87**
6.2 Results and discussions **90**
6.2.1 Variogram 90
6.2.2 Spatial soil moisture patterns 94
6.2.3 Soil moistures frequency distributions 99
6.3 Sensitivity analysis of the soil moisture network **101**
6.4 Spatial soil moisture using defined neighbourhood **109**
6.5 Conditional Gaussian simulations **113**
6.6 Conclusion **117**

7 Utility of remotely-sensed precipitation products for hydrological simulations **119**
7.1 Remotely-sensed precipitation products **119**
7.2 Setup of simulations **120**
7.3 Performance statistics **122**
7.3.1 Bias ratio and root mean square error 122
7.3.2 Error in peaks 122
7.4 Streamflow simulation for 2003 ..... **123**
7.5 Streamflow simulation for 2007 ..... **127**
7.6 Conclusion **132**

8 Conclusion **135**

9 References **137**

10 Appendices **143**

Appendix A: Simulated and measured soil temperature profiles during SGP97 **143**

Appendix B: Comparison of the geostatistical techniques with dynamical modeling **145**

List of figures

1.1 Little Washita river watershed instrumentation site. 5
1.2 Little Washita watershed properties: a) Digital elevation model [m], b) Soil thickness [mm], c) Soil texture, and d) Landuse classes. All maps have 200m-grid resolutio 6

2.1 Simulated and measured heat fluxes at LW02-NOAA site, for: a) net radiation, b) sensible heat, c) latent heat, and d) ground heat. There were two light rainfall events on July 4 and 15, and heavy rainfall event on July 10, 1997. 16
2.2 Simulated and measured soil temperature profile at LW02-NOAA site for depths: a) top 5cm layer (measurement at 3cm and GEOtop simulations at 2.5cm), b) 10cm, c) 20cm, and d) 60cm from the ground surface. 18
2.3 Simulated and measured soil temperature profile at station 136, at depths: a) 2.5cm, b) 10 cm, c) 15cm, d) 20 cm, and e) 60cm from the ground surface. 18
2.4 Simulated and measured soil temperature profile at station 146, at depths: a) 2.5 cm, b), 15 cm, c) 20 cm, and d) 60cm from the ground surface..... 19
2.5 Simulated and measured soil temperature profile at station 149, at depths: a) 2.5 cm, b) 10 cm, c) 15cm, d) 20 cm, and e) 60cm from the ground surface.19
2.6 Simulated and measured soil temperature profile at station 154, at depths: a) 2.5cm, b) 10 cm, c) 15cm, d) 20 cm, and e) 60cm from the ground surface. 20
2.7 Simulated and measured streamflows at the watershed outlet and the watershed total rainfall. 21
2.8 Simulated and measured volumetric soil moisture profile at LW02-NOAA [see Figs. 1.1 and 1.2] at depths: a) 2.5cm, b) 10 cm, c) 15cm, d) 20cm, and e) 60cm from the ground surface. 22
2.9 Simulated and measured soil moisture of the top 5cm soil layer at: a) LW03, b) LW13, and c) LW21 ground-based measurement sites. The continuous thick lines are the simulated soil moistures. The thin lines are the soil moisture measurements. Thin lines are often broken because of missing measurements. The plot shows that the simulated soil moistures have the same trends of the measurements and within the measurement range. 24

3.1 Little Washita experimental sites on soil type map of the watershed, the map has 200m-grid resolution. 29
3.2 Simulated and measured heat fluxes at LW08 experimental site, for: a) Net radiation, b) Sensible heat, c) Latent heat, and d) Ground heat. 30
3.3 Simulated and measured heat fluxes at LW21 experimental site, for: a) Net radiation, b) Sensible heat, c) Latent heat, and d) Ground heat. 30
3.4 Simulated and measured soil temperature at 10cm depth at: a) LW02, ... 31
3.5 Simulated and measured volumetric soil moistures for the top 5cm soil layer at: a) LW04, b) LW05, c) LW08, d) LW09, e) LW11, f) LW12, g) LW13, h) LW21, i) LW22, and j) LW23 33
3.6 Simulated and measured streamflows at the watershed outlet, and the watershed total rainfall. 35

4.1 Volumetric water content of the top 5cm soil layer for July 1, 2, 3, 11, 12, 13, 14, and 16, 1997, from left to right and from top to bottom, respectively.

Each row (couple) refers to a different day. (right) estimated using ESTAR remote sensor. (left) simulated using GEOtop model. 40
4.2 Left graph shows the mean, standard deviation and CV for the ESTAR and simulated soil moistures, and right graph shows the root mean square error, bias and coefficient of determination of water content [-] for the relationships between ESTAR estimates and GEOtop simulations for the entire watershed and for the top 5cm soil layer. 41
4.3 Statistical moments of simulated and ESTAR soil moisture time series, for the sandy loam (left) and silt loam (right) soils, and for the top 5cm soil layer. Figures a), b) and c) show the mean soil moisture, soil moisture STDEV, and soil moisture CV for sandy loam soil, respectively, while figures d), e), and f) show the mean soil moisture, soil moisture STDEV and soil moisture CV for silt loam soil, respectively. 43
4.4 Sandy loam (left) and silt loam (right) soils superimposed on the watershed DEM. 43
4.5 Simulated and ESTAR soil moisture content time series for the top 5cm soil layer for: a) Soil moisture content for all pixels of silt loam soil, b) Soil moisture content for silt loam in only bare soil, c) Soil moisture content for silt loam in only concave pixels, d) Soil moisture content for silt loam in only convex pixels, e) Soil moisture content of silt loam only in non-channel network pixels, and f) Soil moisture content for silt loam in only channel network pixels..... 45
4.6 Simulated and ESTAR soil moisture content time series for the top 5cm soil layer for: a) Soil moisture content for all pixels of sandy loam soil, b) Soil moisture content for sandy loam in only bare soil, c) Soil moisture content for sandy loam in only concave pixels, d) Soil moisture content for sandy loam in only convex pixels, and e) Soil moisture content of sandy loam in only non-channel network pixels. There are no pixels of ESTAR estimates for only channel network. ESTAR resolution is 800m, while GEOtop simulations have 200m-grid resolution. 46
4.7 Simulated surface runoff depth (mm) on July 11, 12, 13, 14, and 16, 1997, from left to right and from top to bottom, respectively. 48
4.8 Simulated intercepted water on vegetation leaves (mm), on July 11, 1997 (left), and July 16, 1997 (right)..... 49
4.9 Simulated soil moisture versus ESTAR soil moisture for the whole watershed and for the days at which we have ESTAR estimates. 50
4.10 Simulated soil moisture [-] versus the measured brightness temperature [K] for the whole watershed..... 51
4.11 Simulated soil moisture [-] versus the measured brightness temperature [K] in bare soil..... 52
4.12 Simulated soil moisture [-] versus ESTAR soil moistures [-] that are lower than 0.4. 54
4.13 Simulated soil temperature [K] versus brightness temperature [K] for the whole watershed. 55
4.14 Simulated soil temperature [K] versus brightness temperature [K] in bare soil. 56
4.15 Soil emissivity for the 5^{th}, 50^{th} and 95^{th} quantiles for the whole watershed, as derived from equation 4.1..... 57
4.16 Spatial surface emissivity for July 1, 2, 3, 11, 12, 13, 14, and 16, from left to right, and from top to bottom, respectively. 58

4.17 Volumetric water content of the top 5cm soil for July 8, 14, and 20, 1999, from left to right and from top to bottom, respectively. Each row (couple) refers to a different day. (right) estimated using ESTAR [800m resolution]. (left) simulated using GEOtop model [200m resolution]. 60
4.18 a) Root mean square error of water content [-] between ESTAR estimates and simulated soil moisture, and b) Bias between ESTAR estimates and simulated soil moisture for the whole watershed. 61
4.19 Simulated and ESTAR soil moisture time series for the top 5cm soil layer for: a) Soil moisture content for all pixels of silt loam soil, b) Soil moisture content for silt loam soil in only bare soil, c) Soil moisture content for silt loam soil in only concave pixels, d) Soil moisture content for silt loam soil in only convex pixels, e) Soil moisture content of silt loam soil in only non-channel network pixels, and f) Soil moisture content for silt loam soil in only channel network pixels. 63
4.20 Simulated and ESTAR soil moisture series for the top 5 cm soil layer for: a) Soil moisture content for all pixels of sandy loam soil, b) Soil moisture content for sandy loam soil in only bare soil, c) Soil moisture content for sandy loam soil in only concave pixels, d) Soil moisture content for sandy loam soil in only convex pixels, and e) Soil moisture content of sandy loam soil in only non-channel network pixels. There are no pixels of ESTAR estimates for only channel network. 64

5.1 Simulated and ESTAR soil moisture frequency distributions for the top 5cm soil layer for both sandy loam and silt loam soils. Sandy loam (left) and silt loam (right) for July 11, 12, 13, and 14, 1997. On July 11 and for the sandy loam soil, model simulations show that most of pixels have the same high soil moisture level. This is because the sandy loam soil lies along the river network (see Fig. 4.4) and the watershed was saturated. 69
5.2 Simulated and ESTAR soil moisture frequency distributions for the top 5cm soil layer for both sandy loam and silt loam soils. Sandy loam (left), and silt loam (right) for July 8, 9, 14, 15, 19, and 20, 1999. 70
5.3 STDEV, CV, and skewness versus mean soil moisture for the top 5cm soil layer during the SGP97, for sandy loam soil (left) and silt loam soil (right). 72
5.4 STDEV, CV, and skewness versus mean soil moisture for the top 5cm soil layer during the SGP99, for sandy loam soil (left) and silt loam soil (right). The skewness in the main ordinate is for the soil moisture derived from GEOtop simulations, while the skewness in the secondary ordinate is for the soil moisture derived from ESTAR estimates. 73
5.5 Kurtosis versus mean soil moisture for the top 5cm soil layer during the SGP97, for the sandy loam (left) and silt loam (right). a) and c) for simulated soil moistures, while b) and d) are for ESTAR estimates. 75
5.6 Kurtosis versus mean soil moisture for the top 5cm soil layer during the SGP99, for the sandy loam (left) and silt loam (right). a) and c) for simulated soil moistures, while b) and d) are for ESTAR estimates. 75
5.7 Log soil moisture variance versus log area for GEOtop simulations and ESTAR estimates along the transect (Fig. 5.10) for the top 5cm soil layer for: a) July 11, b) July 12, c) July 13, d) July 14, and e) July 16, 1997. 78
5.8 Slopes of the fitting lines in figure 5.7. 78

5.9 Log soil moisture variance versus log area for GEOtop simulations and ESTAR estimates along the transect (Fig. 5.10) for the top 5cm soil layer for: a) July 8, b) July 9, c) July 14, d) July 15, e) July 19, and f) July 20, 1999.. 79
5.10 Soil texture map of the Little Washita watershed showing the transect of soil moisture scaling. 79
5.11 Spatial correlation of soil moisture along the transect (Fig. 5.10) for the top 5cm soil layer for: a) July 11, b) July 12, c) July 13, d) July 14, and e) July 16, 1997. 80
5.12 Spatial correlation of soil moisture along the transect (Fig. 5.10) for the top 5cm soil layer for: a) July 8, b) July 9, c) July 14, d) July 15, e) July 19, and f) July 20, 1999. 80
5.13 Soil moisture variograms of the top 5cm soil layer for the Little Washita watershed for: a) July 11, b) July 12, c) July13, d) July14, and e) July16, 1997. 82
5.14 Soil moisture variograms of the top 5cm soil layer for the Little Washita watershed for: a) July 8, b) July 9, c) July14, d) July15, e) July19, and f) July 20,1999. 84

6.1 Simulated volumetric soil moisture content [-] on July 12, 1997 for the top 5cm soil layer, and the locations of the selected 240 points of the soil moisture network shown in (+). 89
6.2 Experimental variograms of the simulated soil moisture (original map) and the soil moisture of the selected 240-points fitted with spherical models. 90
6.3 Variogram of the soil moisture for the selected 240 points in four directions. 91
6.4 Variogram of the residuals combining all predictors except river network, hydraulic conductivity, and coordinates for EDK, fitted with spherical model. 93
6.5 Simulated and Kriged soil moistures for OK and for EDK using different predictors. 97
6.6 Kriged soil moisture variance [%] obtained using the combination of all predictors except river network, hydraulic conductivity and coordinates as predictor for the EDK. 98
6.7 Soil moisture residuals obtained applying kriging cross validation. The applied kriging is EDK that uses all predictors except river network, hydraulic conductivity and coordinates as predictor. 98
6.8 Soil moisture frequency distributions of the top 5cm soil layer for: a) Simulated soil moisture, b) Selected 240 points, c) OK, d) Elevations, e) Gradient, f) Cosine aspect, g) Wetness index, h) Longitudinal curvature, i) Soil depth, j) Laplacian, k) UK, l) River network, m) Combination of gradient and cosine aspect, n) Hydraulic conductivity, and o) All predictors except slope, river network, hydraulic conductivity, and coordinates. 101
6.9 Locations of soil moisture measurement points for: network A, network B, and Vitel. Network B also includes Vitel network. Vitel network compose of stations: 111, 133, 134, 136, 144, 146, 149, 154, 159, 162, Berg, and NOAA. Stations 111 and Berg are outside the watershed. 102
6.10 Experimental variograms of soil moisture for simulated soil moisture map, network A (network illustrated in section 6.1 and Fig. 6.1), network B (shown in Fig. 6.9), and Vitel network (shown in Fig. 6.9) fitted with spherical models. 104

6.11 Simulated and kriged soil moistures for EDKs obtained using soil moisture network B. 106
6.12 Soil moisture frequency distributions of the top 5cm soil layer for: a) Simulated soil moisture, b) 240-points of soil moisture network A, c) 240-points of soil moisture network B, d) Gradient, e) Cosine aspect, f) Combination of gradient and cosine aspect, h) All predictors except river network, hydraulic conductivity, and coordinates. 107
6.13 Main quantiles of soil moisture for simulated soil moisture map, 240-points of network A, and 240-points of network B. 108
6.14 Main quantiles of soil moisture for 240-points of network B and kriged soil moistures obtained using gradient, cosine aspect, combination of gradient and cosine aspect, and all predictors except river network, hydraulic conductivity, and coordinates as predictors for EDK. In the legend combination refers to the combination of gradient and cosine aspect, while all refers to all predictors except river network, hydraulic conductivity, and coordinates.. 108
6.15 Simulated and kriged soil moistures for OK and EDK using different predictors. Kriged soil moistures are obtained using 40 nearest measurement points. 111
6.16 Soil moisture frequency distributions of the top 5cm soil layer for: a) Simulated soil moisture, b) OK, c) Elevations, d) Gradient, e) Cosine aspect, f) Wetness index, g) Longitudinal curvature, h) Soil depth, i) Laplacian, j) UK, k) Hydraulic conductivity, l) River network, m) Combination of gradient and cosine aspect, and n) All predictors except slope, river network, hydraulic conductivity, and coordinates. 112
6.17 Soil moisture maps obtained using conditional Gaussian simulations and in comparison to the simulated soil moisture map (input). 115
6.18 Frequency distribution of the top 5cm soil layer obtained using conditional Gaussian simulations in comparison to the simulated soil moistures: a) Simulated soil moisture, b) No secondary data is used, c) Elevations, d) Gradient, e) Cosine aspect, f) Wetness index, g) Longitudinal curvature, h) Soil depth, i) Laplacian, j) Coordinates, k) River network, l) Hydraulic conductivity, m) Combination of gradient and cosine aspect, n) All predictors except coordinates, river network and hydraulic conductivity. 116

7.1 Raingauge network and CMORPH grids that are used for the 2007 simulations. 121
7.2 Watershed total precipitation for the period March 26 - July 6, 1997 estimated using different precipitation products. Assimilation refers to bias-adjusted CMORPH precipitation. 124
7.3 Comparison of measured streamflows with the simulated streamflows using precipitation data from: raingauge, NEXRAD, PERSIANN-CCS, CMORPH, and bias-adjusted CMORPH (assimilation), from top to bottom, respectively. 126
7.4 Comparison of simulated streamflows obtained using precipitation data from: raingauge, NEXRAD, CMORPH, PERSIANN-CCS, and bias-adjusted CMORPH (assimilation), in semi-log scale. 127
7.5 Watershed total precipitation for each storm 127
7.6 Runoff depth for each storm 129
7.7 Simulated and measured streamflow hydrographs that are greater than $15 m^3/s$. 130

7.8 Bias ratio (left) and RMSE (right) for each storm. 131
7.9 Peak magnitudes (left), and error in peaks (right). 132
7.10 Peak flow time lag from the measured peak flow, negative time lag means the peak occurred before the measured peak flow and positive time lag means the peak occurred after the measured peak flow. 132

A.1 Simulated and measured soil temperature profile at station 144, at depths: a) 2.5cm, b) 10cm, c) 15cm, d) 20cm, and e) 60cm from the ground surface. 143
A.2 Simulated and measured soil temperature profile at station 159, at depths: a) 2.5cm, b) 10cm, c) 15cm, d) 20cm, and e) 60cm from the ground surface. 144

B.1 Variograms of the residuals fitted with spherical models for the following predictors: a) Elevations, b) Gradient, c) Cosine aspect, d) Wetness index, e) Longitudinal curvature, f) Soil depth, g) Laplacian, h) Coordinates (UK), i) River network, j) Hydraulic conductivity, and k) Combination of gradient and cosine aspect. 145
B.2 Soil moisture variance [%] for ordinary kriging and external drift krigings for different predictors. 147
B.3 Soil moisture residuals from the kriging cross validation, for both ordinary kriging and krigings with external drift using different predictors. 149

List of tables

2.1 Calibrated parameters of landuse properties used in GEOtop model..... 11
2.2 Calibrated parameters of soil hydraulic and thermal properties used in the GEOtop model..... 13
2.3 Landuse and soil textures at the ground-based measurement sites 25

3.1 Measured soil specific gravity for the Little Washita experimental sites..... 34

5.1 Variograms properties of simulated and ESTAR soil moisture during SGP97 82
5.2 Variograms properties of simulated and ESTAR soil moisture during SGP99 83

6.1 Properties of variograms of soil moisture and residuals, and mean of residuals of soil moisture..... 92
6.2 Correlation coefficient for the relationships between volumetric soil moistures and predictors..... 93
6.3 Properties of variograms of soil moisture and residuals for the simulated soil moisture map, network A, network B, and Vitel network, and the mean of residuals of soil moisture. 103

1 Introduction

1.1 Motivation

Remotely-sensed precipitation and soil moisture products are becoming increasingly available across the globe. These products are widely used in earth science system and have wide range of applications e.g., regional scale hydrologic or general circulation models. Notwithstanding their wide use, there are still high degree of uncertainties inherited in remotely-sensed precipitation and soil moisture products, and limited studies have focused on the evaluation of these products.

1.2 Soil moisture

Near-surface soil moisture is a key state variable that determines the partitioning of available energy into latent and sensible heat fluxes, and precipitation into runoff and infiltration. It is known for its high degree of space and time variability, caused by variabilities in atmospheric forcing, topography, land cover and soil texture (e.g., Vereecken et al. 2007). However, scientific knowledge about the nature of variability of soil moisture across different space-time scales is very much limited. The limitation arises from lack of reliable soil moisture data at different space-time scales over large domains.

One way of generating spatially distributed soil moisture data on an experimental (prohibitive costs for operational) level is to fly microwave sensors aboard aircrafts. This approach has been used in large-scale soil moisture field campaigns, such as Washita 92 (Jackson et al. 1995), Washita 94 (Starks and Humes 1996), SGP97 and SGP99 (Famiglietti et al. 1999; Famiglietti et al. 2008), SMEX 02 (Jackson et al. 2004), SMEX 03 (Jackson 2002), SMEX 04 (Jackson et al. 2008) and SMEX 05 (Yilmaz et al. 2008) in which aircraft-based microwave sensors were flown for about a month and in-situ soil moisture measurements were taken at selected sites to develop the microwave-based retrieval algorithms and assess their accuracy. Studies show that while microwave-based algorithms have the potential to provide useful information on the space-time variability of soil moisture, they are also subject to a number of error sources, vegetation effects, temperature depth profile and surface roughness (Crosson et

al. 2005; Ulaby et al. 1983), atmospheric conditions (Drusch et al. 2001), radio-frequency interface (Njoku et al. 2005), topography, and satellite azimuth angle and zenith angle (Flores et al. 2009).

Another convenient (and operational) way of generating spatially distributed soil moisture data is through the use of well-calibrated distributed hydrologic model simulation. The word 'well-calibrated' (i.e. through the use of observed streamflow hydrographs and additional sets of observations, such as, soil moistures, soil temperatures and energy fluxes at multiple points) is critical here, because the traditional way of calibrating hydrological models through the exclusive use of observed streamflow hydrographs at the outlet of the watershed fails to reproduce the spatial pattern of soil moisture across the watershed since the same simulated hydrograph can be obtained by assuming quite different spatial soil moisture patterns.

Both sources of spatial soil moisture data (aircraft-based microwave observation, and well-calibrated hydrologic model simulations) have their own error sources. However, no study to our knowledge has done a comparative study of the soil moisture variability estimates derived from both data sources. Do both data sources yield comparable space-time patterns of soil moisture variability? Or do they give us contradictory results raising alarm on the suitability of one of the data sources?

Furthermore, the spatial soil moisture patterns (e.g., Blöschl and Grayson, 2000) are studied in the watershed using different kriging techniques aiming to establish sustainable network of soil moisture measurements in the watershed.

1.3 Remotely-sensed precipitation

Precipitation is critical element in the hydrological cycle and it varies also very much in space and time, and yet there is no unique reliable instrument can measure precipitation at different spatial and temporal scales. Traditionally, raingauges are widely used to estimate precipitation over land surface. Although there are uncertainties in raingauge measurements, raingauges are considered one of the most reliable instruments for estimating precipitation. However, raingauges are point measurements, and it is costly and time consuming to deploy dense raingauge network over large areas to capture the small-scale precipitation variability. Moreover, it is difficult to deploy raingauges over oceans and water bodies. Alternative methods of estimating precipitation are the use of remote sensing techniques that have the ability to estimate precipitation in uniform

spatial and temporal grids for the whole globe. Precipitation estimation from remote sensing techniques is increasing tremendously in the last years. Remotely-sensed precipitation products, for example, include Climate Prediction Center's morphing technique (CMORPH), Precipitation Estimation from Remotely Sensed Information using Artificial Neural Networks - Cloud Classification System (PERSIANN-CCS), Next Generation Weather Radar (NEXRAD), and Tropical Rainfall Measuring Mission (TRMM) Multi-satellite Precipitation Analysis (TMPA) are widely used for precipitation estimation across the globe. However, the footprint of remotely-sensed precipitation is taken at scales larger than the appropriate scales for the underlying hydrological processes.

The scale discrepancy and the uncertainties inherited in remotely-sensed precipitation hindered the use of remotely-sensed precipitation for hydrological applications. One possibility to know to what extent remotely-sensed precipitation products are suitable for hydrological applications, is to use physically-based distributed hydrological models constrained with dense raingauge network, and other meteorological forcing data. The physically-based distributed models have to be first calibrated and validated on intensive ground field data, such as Southern Great Plains Hydrology Experiment- 1997 (SGP97) and SGP99, constrained with dense raingauge network and other measured meteorological forcing data. Once the physically-based distributed models are reasonably calibrated and validated on intensive ground field data, the raingauge data can be replaced by remotely-sensed precipitation measurements, and then the distributed models can be used to test the utility of remotely-sensed precipitation products for hydrological simulations.

1.4 Objective

The objectives of this research are as follows:

1) To evaluate ESTAR soil moisture products using soil moisture measurements and GEOtop model simulations.
2) To study the spatial and temporal variability of soil moistures using ESTAR estimates and GEOtop simulations.
3) To study the scaling properties of soil moisture.
4) To study the spatial soil moisture patterns using geostatistical techniques.

5) To assess the suitability of remotely-sensed precipitation products for hydrological simulations.

1.5 The structure

This work is structured as follows. In chapter 2, GEOtop model is applied to the Little Washita watershed (583 km^2), Oklahoma, USA, using Southern Great Plains Hydrology Experiment-1997 (SGP97) dataset. The model is calibrated at watershed scale and the results of model simulations against the measured heat fluxes (latent heat, sensible heat, ground heat and net radiation), soil temperature profiles at different locations in the watershed, soil moisture profiles at different locations in the watershed, and streamflows at the watershed outlet are shown. In chapter 3, GEOtop model is applied to the Little Washita watershed, and is validated using Southern Great Plains Hydrology Experiment-1999 (SGP99) dataset. Similar results to that obtained in chapter 2 are shown here, but using SGP99 dataset. Chapter 4 focuses on simulated and ESTAR soil moisture patterns obtained during SGP97 and SGP99. The simulated soil moisture maps for the whole watershed are compared to their corresponding ESTAR soil moisture maps for the days at which we have ESTAR soil moisture estimates. The effect of soil texture on soil moisture variability is also shown. In addition, the effects of topography, vegetation, surface roughness, vegetation-intercepted water, and surface runoff on ESTAR soil moistures are investigated. Chapter 5 deals with the characterization of soil moisture during the SGPs using ESTAR passive microwave radiometer and GEOtop model simulations, using both SGP97 and SGP99 datasets. The relationships between statistical moments of soil moisture against the spatial mean soil moisture are identified. Furthermore, soil moisture scaling is also elaborated in this chapter. The comparison of geostatistical techniques with simulated soil moistures is presented in chapter 6. The roles of terrain indices on soil moisture variability are also investigated. The utility of remotely-sensed precipitation, namely, Climate Prediction Center's morphing technique (CMORPH), Precipitation Estimation from Remotely Sensed Information using Artificial Neural Networks - Cloud Classification System (PERSIANN-CCS)- and Next Generation Weather Radar (NEXRAD), for hydrological simulations are shown in chapter 7. Simulations obtained using remotely-sensed precipitation are compared to the raingauge simulations and to the measured streamflows. Finally, concluding remarks of the whole work are presented in chapter 8.

1.6 Study area

The study area is the Little Washita experimental watershed located in the southwest Oklahoma in the Southern Great Plains region of the USA. The watershed has been operated by the Agricultural Research Service – Grazinglands Research Laboratory (ARS-GRL) since 1961 (Allen and Naney 1991). Little Washita drains about 583 km^2 to the USGS gage #07327550 east of Ninnekah, OK, and landuse is mostly grazing land and winter wheat (Fig. 1.2d). Soil textures range from fine sand to silt loam (Fig. 1.2c), with more than 75% of the watershed having SCS hydrologic soil group B soils (moderately well to well-drained). The more slowly drained soils lay in the western and eastern ends of the watershed with the more sandy soils in the centre. Topography is rolling with minimum elevation of about 300m and maximum elevation of about 500m (Fig. 1.2a). Soils are 0.25 to 1.5m thickness (Fig. 1.2b) and are underlain by sedimentary rocks, primarily sandstone. Climate is considered sub-humid, with 760mm of annual precipitation, and July average daily minimum and maximum temperatures of 21 and 35°C, respectively and January average daily minimum and maximum temperatures of -4 and 10°C, respectively. The watershed is well instrumented [Fig. 1.1] for hydrological studies and has been the site for several major soil moisture field experiments (e.g., SGP97, and SGP99).

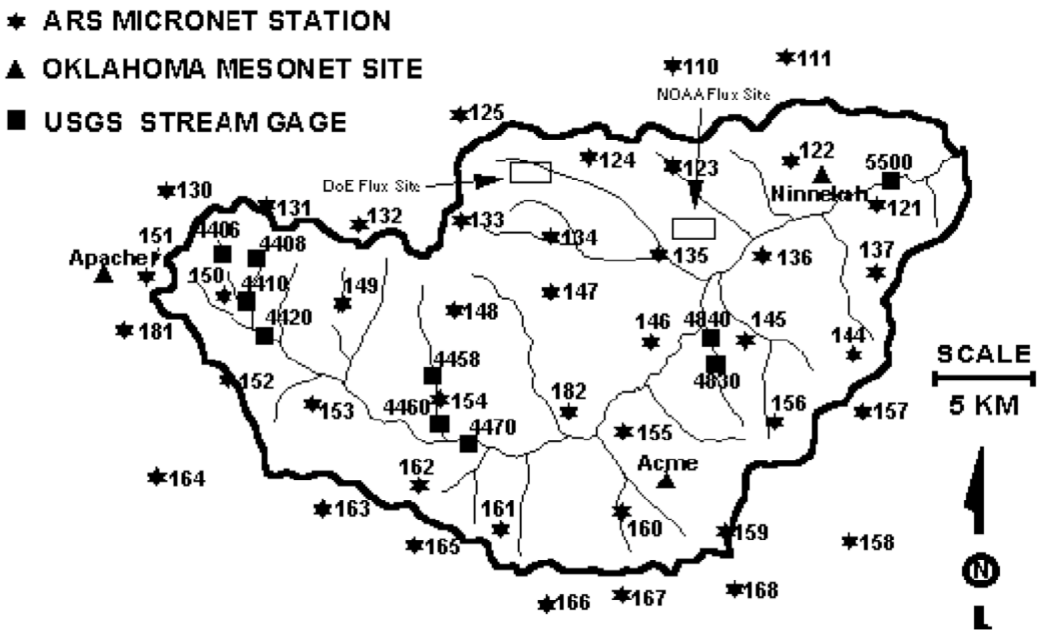

Figure 1.1: Little Washita river watershed instrumentation site.

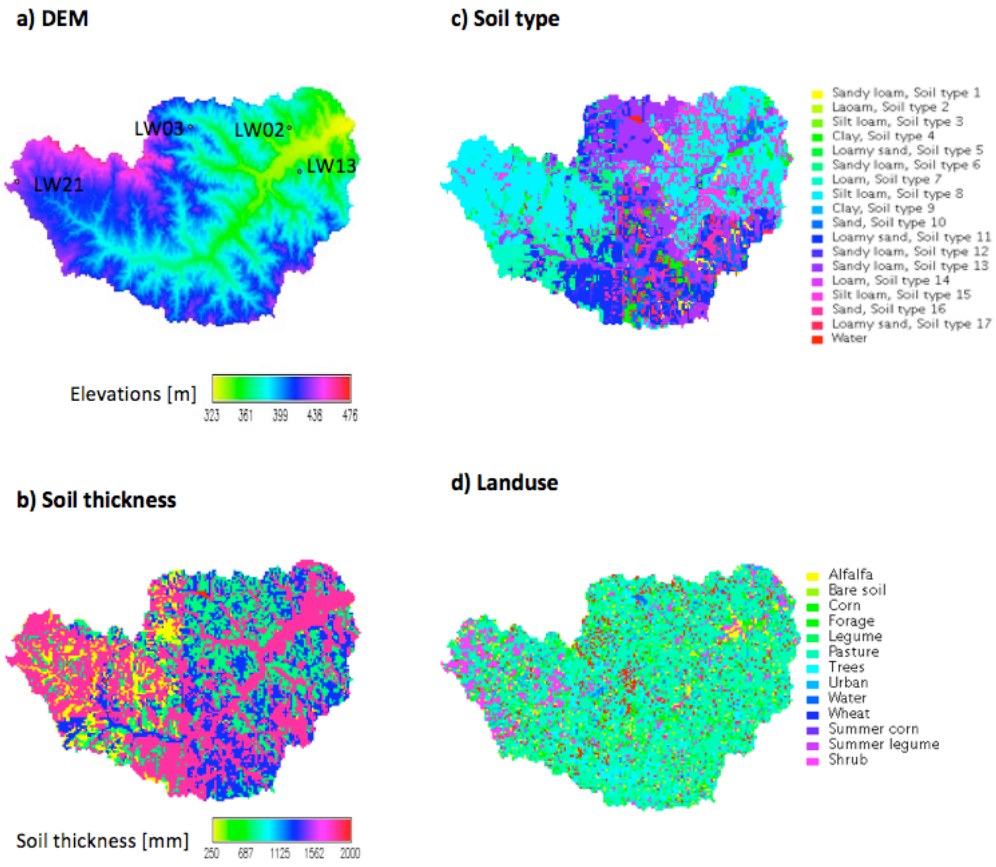

Figure1.2: Little Washita watershed properties: a) Digital elevation model [m], b) Soil thickness [mm], c) Soil texture, and d) Landuse classes. All maps have 200m-grid resolutio

1.7 The GEOtop model

GEOtop model (Rigon et al. 2006) is a distributed hydrological model with coupled water and energy budgets. GEOtop includes solution of the Richards' (Richards 1931) equation in three dimensions for evolution of soil water content and pressure, coupled with one-dimensional simulation of soil heat transport. All hydraulic soil properties are assigned through Van Genuchten (1980) schematization. The energy balance equation includes the effects of slope, aspect, shadow and sky view factor. Sensible and latent heat fluxes are estimated using similarity theory (Monin and Obukhov 1954). The ground heat flux is computed as a function of soil temperature gradient according to the Fourier heat diffusion equation. The surface runoff is routed according to a kinematic

scheme that accounts for local slopes and surface resistance. The surface water flow in channels is described by the convolution of the incoming discharge with the solution of the Barré de Saint-Venant equations (Barré de Saint-Venant 1871).

The basic inputs of the model are Digital Elevation Model (DEM), land cover map, and soil texure map. For each grid, land cover and soil properties are specified. Forcing data of the model are precipitation, wind speed and direction, air pressure, air temperature, relative humidity, cloudiness, solar global short-wave radiation, and if available diffuse and long-wave radiation. The precipitation is partitioned into rain and snow. If more raingauges are available, the value of precipitation in every grid is obtained using kriging method. For more details about the GEOtop model and its capabilities see Rigon et al. (2006), Bertoldi (2007), Bertoldi and Rigon (2004), Dall'Amico (2010), Endrizzi (2007), Bushara and Rigon (2010), Bushara et al. (2010), Bushara et al. (2011a), Bushara et al. (2011b), Simoni et al. (2008).

2 Model calibration using Southern Great Plains 1997 (SGP97) hydrology experiment dataset

We used the comprehensive field data collected during the SGP97 in the Little Washita watershed (583 km^2), Oklahoma, USA to fully calibrate the physically-based distributed hydrological model, GEOtop (Rigon et al. 2006). Then the model can be used to validate ESTAR soil moistures. GEOtop model is driven by meteorological forcings taken at an hourly time step from 45 meteorological stations. The model runs once at the watershed scale, and is reasonably calibrated for the energy fluxes (latent heat, sensible heat, ground heat, and net radiation), soil temperature profiles up to 60cm depth from the ground surface at different locations, volumetric soil moisture profiles up to 60cmm depth from the ground surface at different locations, and streamflows at the watershed outlet.

2.1 Dataset

The Southern Great Plains 1997 (SGP97) Hydrology Experiment took place from June 18 to July 17, 1997, and was a cooperative effort between NASA, USDA, and several other government agencies and universities conducted with the primary goal of collecting a time series of spatial soil moisture data. The core of the experiment involved the deployment of the L-band ESTAR for daily mapping of surface soil moisture. ESTAR is a synthetic aperture, passive microwave radiometer operating at a frequency of 1.413 GHz (21 cm). ESTAR was flown on a P-3B aircraft (at an altitude of 7.5 km) operated by the NASA Wallops Flight Facility. The P-3B flew over Little Washita (Fig. 1.1) at approximately 16:00 UTC (10:00 CST). The footprint of the raw brightness temperature data is 400m, but the raw data were resampled to 800m to derive soil moisture maps. Further details on the ESTAR instrument and the inversion of ESTAR brightness temperatures to volumetric soil moisture can be found in LeVine et al. (1994), Jackson et al. (1995), Jackson and LeVine (1996), and Jackson et al. (1999). ESTAR soil moisture estimates, available at http://daac.gsfc.nasa.gov/fieldexp/SGP97/estar.html (verified June 2009), have been used in this study. The estimates cover a large strip of approximately 50km (West-East) by 250km (North-South), with a pixel grid size of 800m × 800m. The subset of the data

that covers the Little Washita was selected. The estimates represent approximately volumetric soil moisture of the top 5cm soil layer, i.e., 800m × 800m × 5cm volume of soil that is occupied by water.

For this study, the comprehensive dataset available through the SGP97 makes a great opportunity to use such rare and intensive dataset to calibrate hydrological models and to further use hydrological models to validate remotely-sensed soil moistures. During the SGP97 experiment, heat fluxes, soil temperature profiles, soil moisture profiles, meteorological forcing data, and streamflows time series are measured at different locations in the watershed. Landuse cover and soil texture maps are available for the whole watershed.

2.2 Atmospheric forcing to the GEOtop model

GEOtop model is driven by meteorological forcing data taken at an hourly time step from 45 stations [ARS and MESONET networks, see Fig. 1.1] and each station measures precipitation, relative humidity, air temperature, downward solar radiation, wind speed, wind direction and air pressure. Furthermore, the cloudiness for each meteorological station is computed as reported in Liston and Elder (2006). The GEOtop model runs once for the period from July 1 to August 30, 1997 at the watershed scale, for 200m grid resolutions, considering all energy and water balance components.

2.3 Model initialization and setup

2.3.1 Initial and boundary conditions and parameters derived from literature

Each of the landuse and soil texture classes have a total of 13 and 18 parameters, respectively, required initialization during model setup. Each landuse type is initialized for the following parameters: surface roughness, momentum roughness length/heat roughness length ratio, zero-plane displacement height, canopy height, canopy fraction, leaf area index (LAI) for both summer and winter seasons, minimum stomatal resistance, root depth, water content of wilting point, water content of field capacity, albedo, soil emissivity and the coefficient of the law of uniform motion of surface flow. The properties of landuse classes are shown in table 2.1. The data shown in this table are calibrated parameters, but the ranges of these parameters are taken from Mohanty (1999), Dingman (1994), and Garratt (1992). The water flow parameters are also

initialized: the mean velocity in channels, hydrodynamical dispersion in channels, and the exponent of the law of uniform motion of the surface. Since the simulation is during summer time (July 1 - August 30, 1997), both the snow and the glacier modules are switched off.

Table 2.1: Calibrated parameters of landuse properties used in GEOtop model

Landuse type	h_c [mm]	d_0 [mm]	Z_0 [mm]	Z_0/Z_{0T} [-]	f_c [mm]	LAI [L^2/L^2]	r_s [s/m]	r_d [mm]	θ_{wp} [-]	θ_{fc} [-]	C_m	*Albedo*	ε [-]
Alfalfa	750	480	500	100	0.9	6	70	800	0.09	0.21	3.8	0.2	0.97
Bare soil	100	66	10	10	0.1	0.001	10	200	0.14	0.29	3.8	0.2	0.97
Corn	1750	1166	175	10	0.9	4	70	1300	0.12	0.32	3.8	0.2	0.95
Forage	600	350	60	10	0.6	3	70	700	0.21	0.36	3.8	0.2	0.95
Legume	750	500	75	10	0.9	4	70	800	0.088	0.15	3.8	0.2	0.95
Pasture	500	400	5	10	0.55	2.5	70	700	0.09	0.21	3.8	0.04	0.95
Trees	7000	1000	700	10	0.8	5	70	1500	0.14	0.29	3.8	0.2	0.96
Urban	1600	1066	16	10	0.01	2.5	10	600	0.12	0.32	0.05	0.01	0.95
Water	100	66	10	10	0.01	1	3	200	0.21	0.36	5	0.3	0.96
Wheat	1750	30	75	10	0.95	6	70	1300	0.088	0.13	3.8	0.3	0.98
Summer corn	750	500	75	10	0.9	4	70	800	0.088	0.15	3.8	0.2	0.95
Summer legume	1750	1166	175	10	0.9	4	70	1300	0.09	0.21	3.8	0.2	0.95
Shrub	4000	1000	400	10	0.4	3	70	800	0.09	0.21	3.8	0.2	0.95

h_c canopy height [mm], d_0 displacement height [mm], Z_0 surface roughness [mm], Z_0/Z_{0T} momentum roughness to heat roughness ratio, f_c canopy fraction [-], LAI leaf area index[L^2/L^2], r_s minimum stomatal resistance [s/m], r_d root depth [mm], θ_{wp} water content of wilting point[-], θ_{fc} water content of field capacity[-], C_m coefficient of the law of uniform motion on the surface [$L^{-[1-\gamma]}T^{-1}$], and ε emissivity[-].

Each soil type is divided into 7 layers, the centres of these layers from the ground surface are: 25, 100, 150, 200, 350, 600 and 925mm. These soil layers are considered because most of the measurements, including soil moistures and soil temperatures, are taken at these depths and this allows for a direct comparison of the measurements with the model results. The model initial soil moisture of the first soil layer (5cm thickness) is taken to be the mean soil moisture estimated by ESTAR for the whole watershed on July 1, 1997, which is the starting date of the simulation. The initial pressure head for the top 5cm soil layer is obtained using the pedotransfer functions (Vereecken et al. 1989) given the measured soil moisture content from ESTAR. While for the deep soil layers the model is initialized considering hydrostatic pressure profile. Other soil properties: residual water content, saturated water content, *alpha* of Van Genuchten (Van Genuchten 1980), *n* of Van Genuchten, and hydraulic conductivities are taken from the estimation of soil water properties study by Rawls et al. (1982). While soil parameter *m* has been set to 1 according to Vereecken et al. (1989) and soil parameter *v* set to 0.5, which is a usual value as indicated by Mualem (1976). The thermal conductivity and volumetric heat capacity of each soil layer are also initialized as described in Brutsaert (1983) and Garratt (1992). The initial soil temperature for each soil layer is taken to have the same value of the measured temperature at the considered depth. The soil hydraulic and thermal properties used in the GEOtop model simulations are shown in table 2.2.

2.3.2 Procedure of model spin-up

Following the initialization of model parameters, GEOtop is first calibrated for net radiation, sensible heat, and latent heat fluxes by changing landuse, soil, and surface parameters, such as albedo, soil emissivity, LAI, canopy fraction, surface roughness, and momentum roughness length/heat roughness length ratio. Then the ground heat flux is calibrated by changing soil thermal conductivities and soil volumetric heat capacity. For each soil type and at each depth, the soil thermal properties (i.e. thermal conductivity and volumetric heat capacity) are calibrated. Right calibration of soil thermal properties results on right soil temperatures at deep soil layers. Then the model runs for two months (July 1 to August 30, 1997). As shown in figure 2.8, for each soil layer, the soil moisture on July 1, approximately equals to the soil moisture on July 18. Figure 2.8 shows that soil moisture seems to have persistent temporal periodicity.

Table 2.2: Calibrated parameters of soil hydraulic and thermal properties used in the GEOtop model

Soil texture	K_h [mm/s]	K_v [mm/s]	θ_r [-]	θ_{sat} [-]	α [mm^{-1}]	n [-]	λ [$W\ m^{-1}\ k^{-1}$]	ρC [$J\ m^{-3}\ k^{-1}$]
Sandy loam	0.001-0.9	0.001-1.6	0.03-0.13	0.29-0.4	0.0006-0.01	1.1-1.322	0.3	1E6- 2E6
Loam	0.003-0.5	0.001-0.015	0.09-0.13	0.39-0.42	0.009-0.012	1.1- 1.3	0.3	2E6
Silt loam	0.009-0.5	0.001-0.16	0.09-0.17	0.39-0.47	0.0048-0.01	1.1-1.41	0.2- 5.3	0.7E6-2E6
Clay	0.008-0.01	0.0001-0.01	0.09-0.11	0.36-0.37	0.0027-0.006	1.131	0.3	2E6
Loamy sand	0.022-0.025	0.01-0.5	0.05-0.07	0.37-0.41	0.0115-0.014	1.474	0.3	2E6
Sand	0.08-0.09	0.05-1.4	0.02-0.04	0.39-0.41	0.0138-0.017	1.592	0.3	2E6

K_h horizontal hydraulic conductivity [mm/s], K_v vertical hydraulic conductivity [mm/s], θ_r residual water content, θ_{sat} saturated water content, α of Van Genuchten [mm^{-1}], n of Van Genuchten, λ thermal conductivity [$Wm^{-1}\ k^{-1}$], ρC volumetric heat capacity [$J\ m^{-3}\ k^{-1}$]. Within the soil type, the soil hydraulic and thermal properties vary with the depth.

It found that the soil moisture on August 30 approximately equals the soil moisture on July 1. The concept of spinning the model is well expressed here: http://abouthydrology.blogspot.com/2011/01/geotop-guidlines-for-distributed.html
Then the model is reinitialized by taking the new values of the pressure head obtained on August 30, as the input to the GEOtop model. This process is repeated six times (about one year) in order to have spatially correct pressure head in each model grid and in each soil depth. After calibrating the surface heat fluxes and the soil temperatures, the subsurface flow is calibrated. The subsurface flow is calibrated first because the subsurface flow component is small, compared to the total flow, and there is sufficiently relatively long dry-down period (July 1 to 4) without rainfall. Then the surface flow is calibrated, and mainly by changing the coefficient of the law of the uniform motion of the surface, C_m, the mean velocity in the channels and the hydrodynamical dispersion in the channels, while keeping the exponent of the law of the uniform motion of the surface (γ) fixed after it has been calibrated. The surface flow is described by the following equation:

$$q_{\sup} = C_m h^{\gamma} i^{0.5} \qquad (2.1)$$

Where q_{sup} is the surface flow per unit surface area [L/T], C_m is coefficient of the law of the uniform motion of the surface [$L^{-[1-\gamma]}$ T^{-1}], h is surface water thickness [L], i is the local slope [dimensionless] and γ is exponent of the law of the uniform motion of the surface [dimensionless].
Successive model simulations are conducted by calibrating the initial pressure head and *alpha* and *n* of Van Genuchten parameters in order to reproduce the soil moisture measurements for the 1st day of the simulation, and that is applied for each soil type (in total 18 soil types) and for each soil layer (in total 7 layers). Once the correct soil moistures at the start of the simulation have been granted, the full soil moisture time series are simulated by tuning again the initial pressure head, *alpha* and *n* of Van Genuchten parameters, residual water content, horizontal hydraulic conductivity and vertical hydraulic conductivity. Then the whole process is repeated from the beginning for tuning all the above-mentioned parameters. To reproduce the correct flow at the watershed outlet, only the exponent of the law of the uniform motion of the surface (γ) is tuned.

2.4 Performance statistics

We used the Nash-Sutcliffe efficiency (Nash and Sutcliffe 1970) and normalized bias to evaluate the model performance. The Nash-Sutcliffe efficiency (NSE) is computed as follows:

$$E = 1 - \left[\frac{\sum_{i=1}^{n} (SIM_i - OBS_i)^2}{\sum_{i=1}^{n} (OBS_i - OBS_{mean})^2} \right] \tag{2.2}$$

While the normalized bias is computed as follows:

$$Bias = \frac{1}{n(OBS_{\max} - OBS_{\min})} \sum_{i=1}^{n} (OBS_i - SIM_i) \tag{2.3}$$

Where *SIM*, *OBS*, OBS_{mean}, OBS_{max}, OBS_{min}, is the simulated, observed, mean of observed, max of observed, and min of observed, respectively, and *n* is the total number of pairs of simulated and observed data. NSE ranges from -∞ to 1, with higher values indicating better agreement between the data and the simulations. An efficiency of 1 indicates a perfect match of the simulations to the observed data. An efficiency of 0 indicates that the model predictions are as accurate as the mean of the observed data, while efficiency less than zero indicates that the observed mean is a better predictor than the model.

2.5 Results and discussions

2.5.1 Simulated heat fluxes

GEOtop model is calibrated at LW02-NOAA site (Figs. 1.1 and 1.2) for all fluxes: latent heat, sensible heat, ground heat, and net radiation, as shown in figure 2.1. GEOtop model is fairly reproducing the diurnal cycles of all energy fluxes. GEOtop is fairly reproducing the fluxes for both daytimes and nights, and that all the simulated fluxes follow similar trends of the measurements. Among the fluxes, net radiation performed well compared to the other fluxes. Figure 2.1d shows that the ground heat flux increases

as soil moisture increases, resulting on high negative ground heat fluxes on July, 4, 10, and 15, 1997, at which there were storm events. These high negative ground heat fluxes (Fig. 2.1d) together with sensible heat (Fig. 2.1b) are counterbalanced by the latent heat flux (Fig. 2.1c).

Generally, all the simulations show good agreement with the observations. The NSE for the fitted net radiation, sensible heat, latent heat, and ground heat is 0.408, -0.05, 0.46, and -1.23, respectively, while their normalized biases values are 0.11, 0.08, 0.02, and 0.06, respectively. The correlation coefficient between the simulated and the measured net radiation, sensible heat, latent heat, and ground heat is 0.73, 0.61, 0.72, and 0.19, respectively.

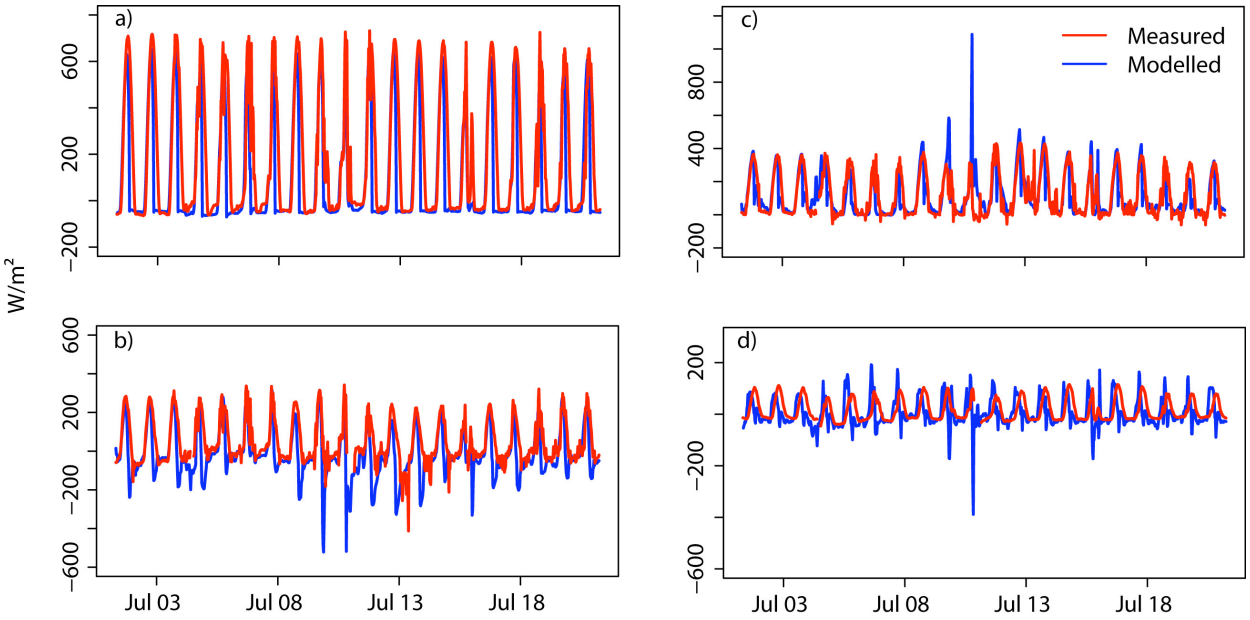

Figure 2.1: Simulated and measured heat fluxes at LW02-NOAA site, for: a) net radiation, b) sensible heat, c) latent heat, and d) ground heat. There were two light rainfall events on July 4 and 15, and heavy rainfall event on July 10, 1997.

2.5.2 Simulated soil temperatures

The surface temperature is computed by solving the surface energy balance equation (Rigon et al. 2006). The simulated soil temperatures are compared to the observations at stations: NOAA, 136, 146, 144,149, 154, and 159 (Fig. 1.1) for depths at 2.5, 10, 15, 20

and 60cm from the ground surface. The stations are distributed across the watershed and lay on different elevations, slopes, aspects, landuses and soil types. In general, the simulations show good agreement with the observations at all locations. Figure 2.2 shows soil temperature profile at LW02-NOAA site, while figures 2.3 to 2.6 show the soil temperature profile at station 136, 146, 149 and 159, respectively. The measured and the simulated soil temperatures for stations 144 and 159 are shown in appendix A. Figures 2.3 to 2.6 also show that the model is fairly simulating the soil temperature profiles at stations 136, 146, 149 and 154. Following the rainfall event on July 4, 1997 all temperature time series become more damped as soil moisture increases with the depth from the ground surface. The diurnal temperature effects diminish at about 60cm depth. At NOAA site, the model is perfectly simulating the temperature measurements for each soil layer, but with less fitting to the 1st top layer. The differences between the measurements and the GEOtop simulations for the first layer is due to the fact that the soil temperature is simulated at 2.5cm depth, while the measured temperature is taken at 3cm depth. Moreover, the differences may be enhanced due to possible soil tension cracks and surface soil disturbance due to human activities, e.g., during the installation of temperature measuring devices. The model is reasonably reproducing the mean soil temperature. We observe that for all stations, the topsoil layer is not well simulated compared to the deep soil layers. This is due to the fact that the model does not consider the heat conduction between the stagnant air layer above the terrain and the soil. For more details about the heat conduction between the stagnant air layer and the soil see Bohren and Albrecht (1998). The slight mismatch often seen between the simulated and the measured temperatures for stations 144, 146, and 159 (see Fig. 2.4 and appendix A) is due to the difference in the chosen initial soil temperatures. If offset values of temperature were added to the simulated or to the measured temperatures, there would be perfect match between the simulated and the measured temperatures. This is due to the fact that we chose only spatially uniform soil thermal properties for each soil type.

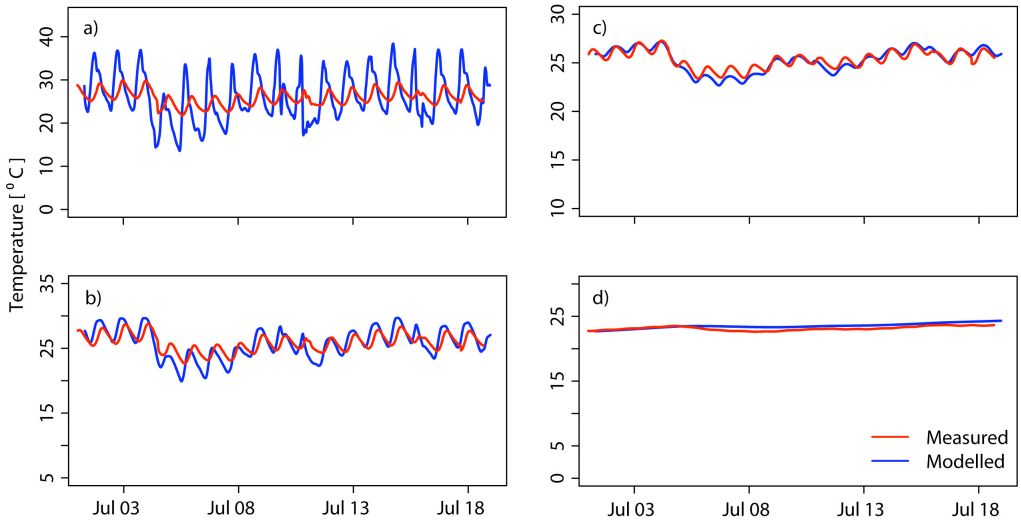

Figure 2.2: Simulated and measured soil temperature profile at LW02-NOAA site for depths: a) top 5cm layer (measurement at 3cm and GEOtop simulations at 2.5cm), b) 10cm, c) 20cm, and d) 60cm from the ground surface.

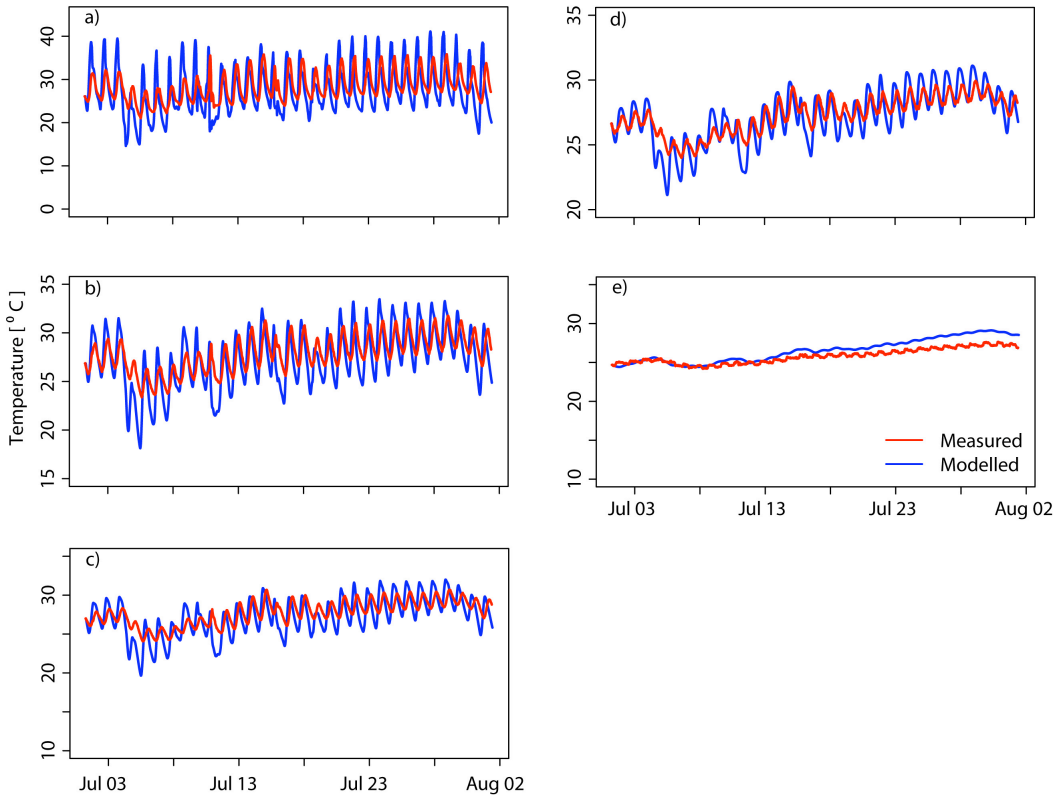

Figure 2.3: Simulated and measured soil temperature profile at station 136, at depths: a) 2.5cm, b) 10 cm, c) 15cm, d) 20 cm, and e) 60cm from the ground surface.

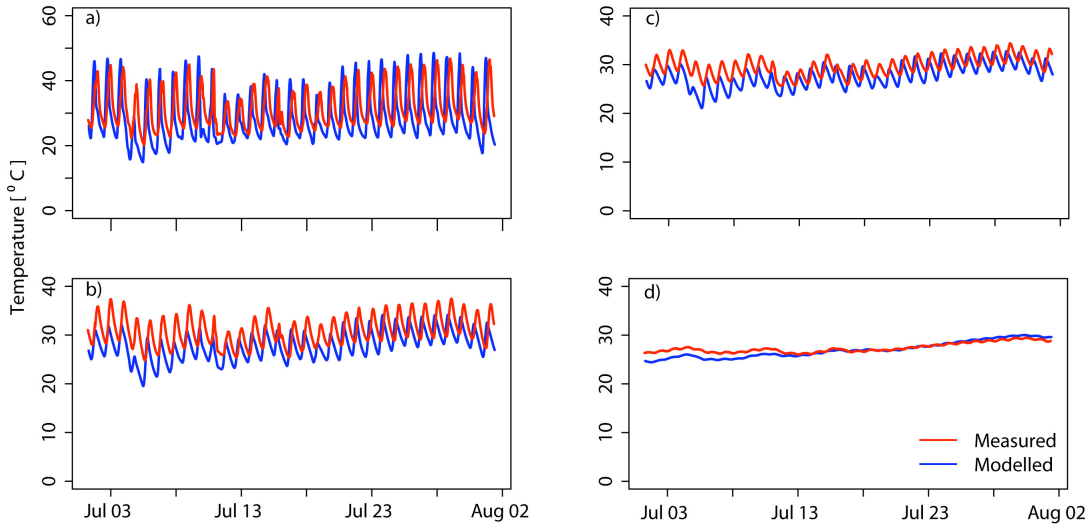

Figure 2.4: Simulated and measured soil temperature profile at station 146, at depths: a) 2.5 cm, b), 15 cm, c) 20 cm, and d) 60cm from the ground surface.

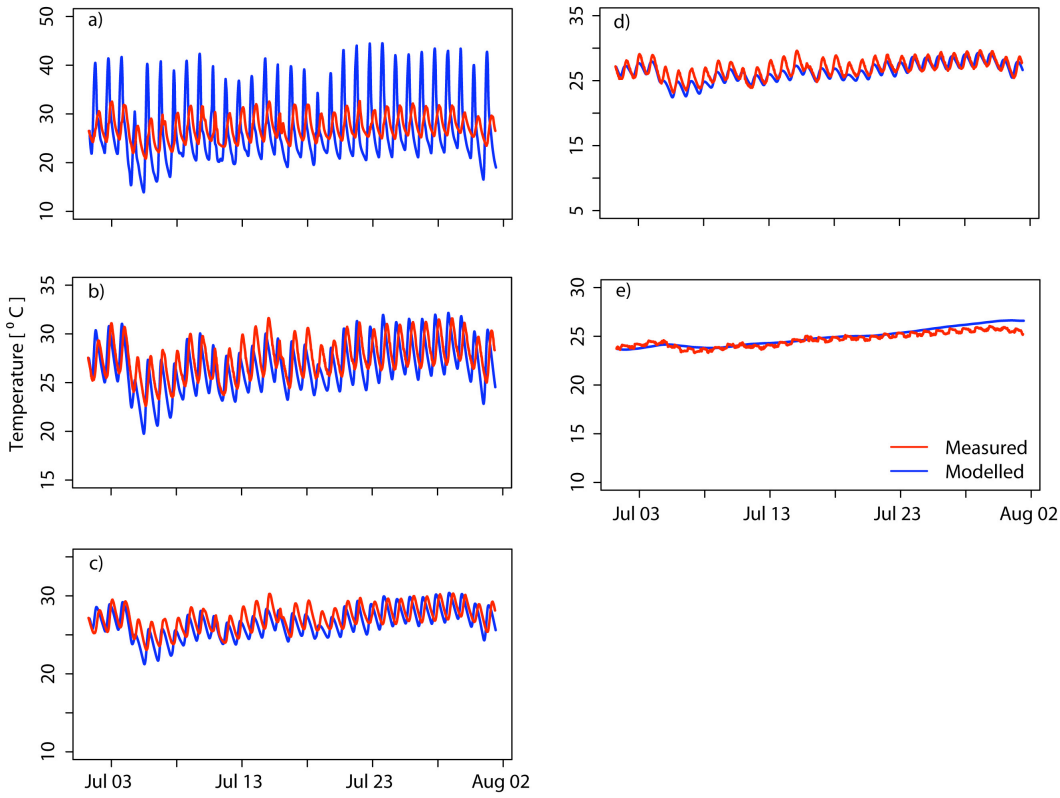

Figure 2.5: Simulated and measured soil temperature profile at station 149, at depths: a) 2.5 cm, b) 10 cm, c) 15cm, d) 20 cm, and e) 60cm from the ground surface.

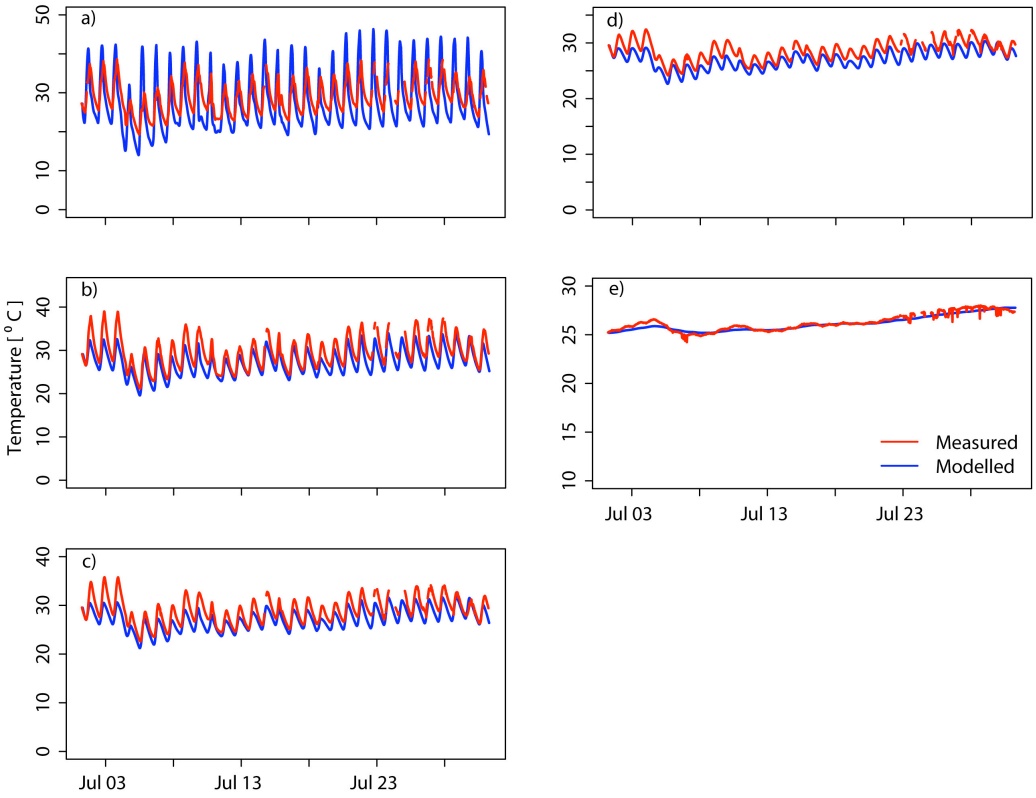

Figure 2.6: Simulated and measured soil temperature profile at station 154, at depths: a) 2.5cm, b) 10 cm, c) 15cm, d) 20 cm, and e) 60cm from the ground surface.

2.5.3 Simulated streamflows

Figure 2.7 shows the measured and the simulated total streamflows (m^3/s) at the watershed outlet as well as the total precipitation (mm) that falls in the watershed during the study period. The model is reasonably simulating the base flows as well as the peak flows. In spite of that, the model is slightly underestimating some parts of the discharge recession curve after the heavy rainfall event on July 10. Although the simulated and the measured streamflow time series are taken every 15 minutes, acceptable values for NSE and bias are obtained. The values of Nash-Sutcliffe and bias are equal to 0.6000 and 0.00086, respectively. The mean channel velocity is calibrated to be 1.8 m/s and the channel hydodynamical dispersion is calibrated to be 15 m^2/s, while the exponent of the law of uniform motion of the surface is calibrated to 0.32. The q_1 and q_2, which are the

slope of the land converging to the channel, and fraction of the pixel occupied by the channel, respectively, are calibrated to be 0.17 and 0.10, respectively.

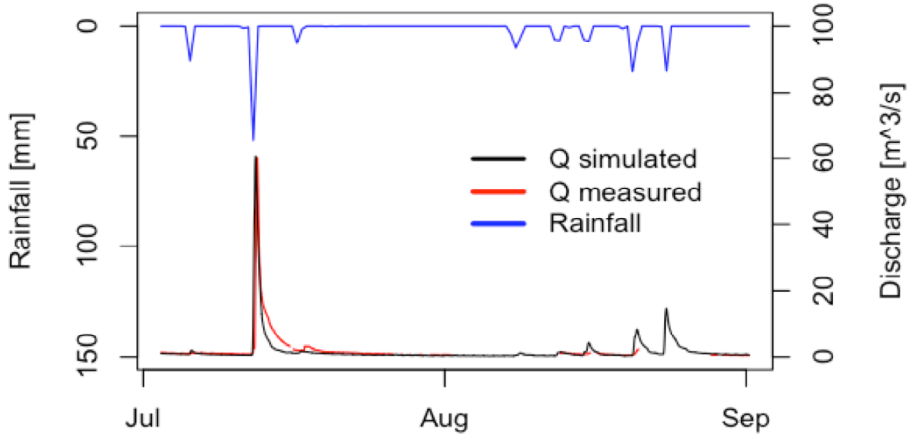

Figure 2.7: Simulated and measured streamflows at the watershed outlet and the watershed total rainfall.

2.5.4 Simulated soil moistures

Figure 2.8 shows the measured and the simulated soil moisture profiles at LW02-NOAA site whose landuse type was Alfalfa on sandy loam soil (soil type 13 - hydraulic conductivity = 2.00 - 6.30 mm/s). The soil moistures were measured at all depths using Water Content Reflectometer. Figure 2.8a shows the simulated and the measured soil moisture for the top 6cm soil layer. The model is reasonably simulating the whole measured time series of soil moisture.

Figure 2.8b shows the simulated and the measured soil moisture at a depth of 10cm. The model is also fairly simulating the measurements although the model is slightly overestimating the second dry-down period (July 4-10) of the soil moisture time series. The model is also fairly simulating the full soil moisture time series at depths of 10, 15,20 and 60cm from the ground surface as shown in figures 2.8b, 2.8c, 2.8d, and 2.8e, respectively. The NSE for the soil moisture at NOAA site at 2.5cm, 10cm, 15cm, 20cm, and 60cm depths is 0.83, 0.4, 0.66, 0.76, and -1.97, respectively. While the correlation coefficient for the soil moisture at NOAA site at 2.5cm, 10cm, 15cm, 20cm, and 60cm depths is 0.87, 0.79, 0.88, 0.89, and 0.15, respectively.

As seen from all above figures the max difference between the measured and the simulated soil moisture contents is less than 0.05, and the simulated soil moistures are timely responding to the rainfall events.

This section shows the ability of GEOtop model to simulate the diurnal cycles of soil moistures at different depths from the ground surface after it reasonably reproduced the total flow at the watershed outlet, as well as the heat fluxes and soil temperature profiles. In addition to that, this section shows the potentials of distributed hydrological models to simulate soil moistures at different depths, in oppose to the remotely-sensed soil moisture instruments that measure soil moisture for only shallow depths.

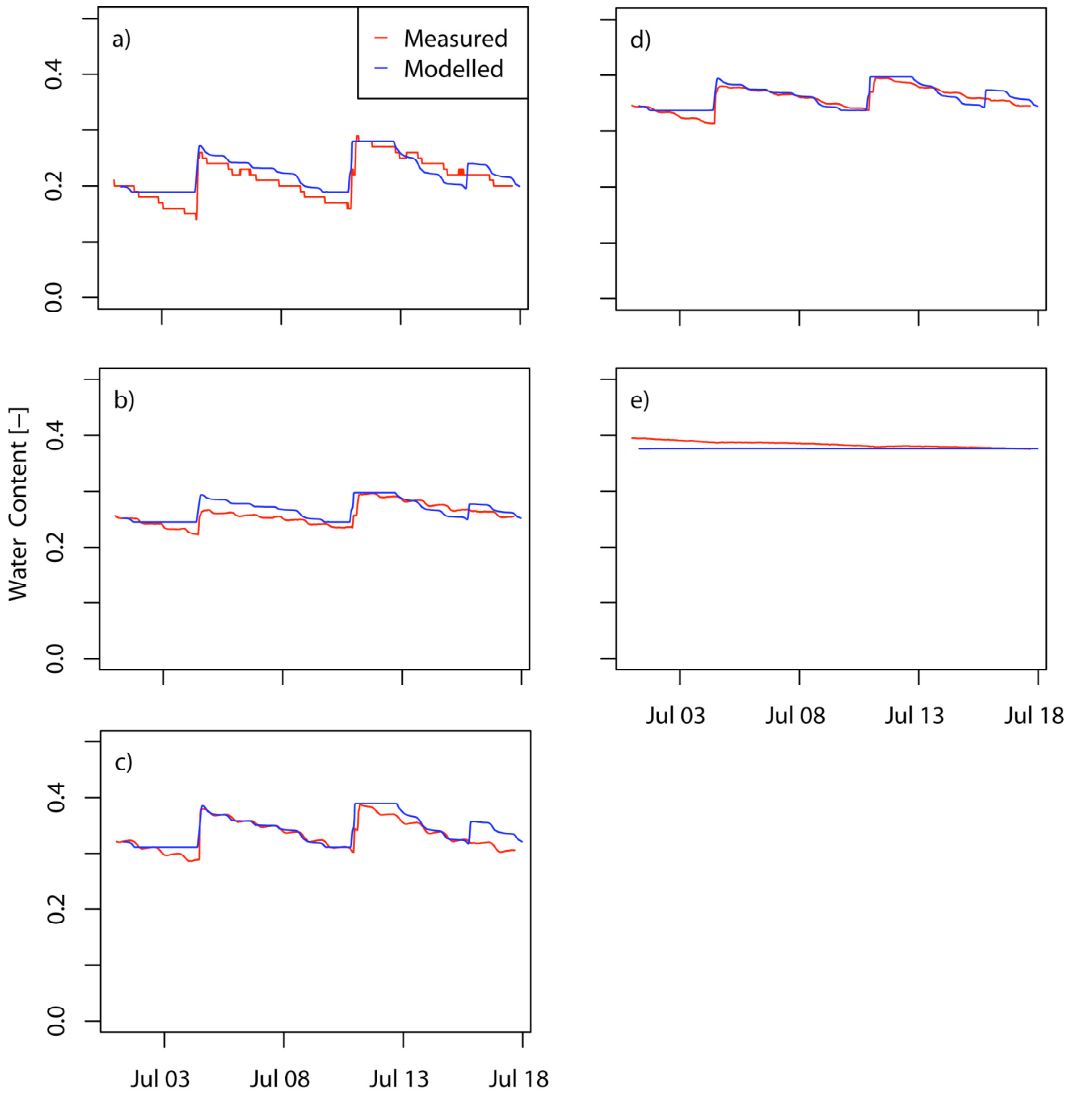

Figure 2.8: Simulated and measured volumetric soil moisture profile at LW02-NOAA [see Figs. 1.1 and 1.2] at depths: a) 2.5cm, b) 10 cm, c) 15cm, d) 20cm, and e) 60cm from the ground surface.

Figures 2.9a, 2.9b, and 2.9c show the measured and the simulated soil moisture at LW03, LW13 and LW21 experimental sites, respectively for the top 5cm soil layer. For each site, which is 800m × 800m, volumetric soil moistures were measured at 49 locations, and named Site_1 to Site_49. However, in each figure only few measured time series are shown in order to make the figures more readable. The exact coordinates of these 49 sites were not reported in the SGP97 experiment. However, coordinates of some locations inside each site are known and the surface soil moistures are simulated at these locations. For each site, the soil moistures are simulated at these known locations, and named Model_1 to Model_4 and shown with thick lines in the figures.

At LW03 the soil type at the four known locations is sandy loam (soil type 13 - hydraulic conductivity = 2.00 - 6.30 mm/s), which is the same soil type at LW02. At LW13, Model_1, Model_2 and Model_3 points lay on silt loam (soil type 8 - hydraulic conductivity = 0.63 - 2.00 mm/s), while Model_4 point lies on another kind of silt loam (soil type 15 - hydraulic conductivity = 2.00 – 6.30 mm/s). Finally, at LW21 Model_1 and Model_2 points lay on silt loam soil (soil type 8 - hydraulic conductivity = 0.63 - 2.00 mm/s). It is evident that the simulated soil moistures follow the same trends of the measurements and within the measurements range at all the experimental sites. The model is fairly simulating the soil moistures for the sandy loam (soil type 13 - hydraulic conductivity = 2.00 - 6.30 mm/s) at LW02 and LW03 experimental sites. Also the model is fairly simulating the soil moistures for different kinds of silt loam soils (soil type 8 - hydraulic conductivity = 0.63 - 2.00 mm/s, and soil type 15 - hydraulic conductivity = 2.00 – 6.30 mm/s) at LW13 experimental site. Furthermore, the model is reasonably simulating the soil moisture for the silt loam soil (soil type 8 - hydraulic conductivity = 0.63 - 2.00 mm/s) at the LW21 experimental site.

The model is able to simulate soil moistures for different soil types in the experimental sites. Furthermore, the model is able to simulate soil moistures for a given soil type at different experimental sites.

From all the above simulations, it is evident that the model is reasonably reproducing soil moistures at LW02, LW03, LW13 and LW21 experimental sites. These sites lay on different elevations, soil types and land use types. The types of soil textures and landuse at each experimental site are shown in table 2.3. Soil textures shown in table 2.3 are dominant in the study watershed (Fig. 1.2). Sandy loam (soil type 13 - hydraulic conductivity = 2.00 - 6.30 mm/s), silt loam (soil type 8 - hydraulic conductivity = 0.63 -

2.00 mm/s), and silt loam (soil type 15 - hydraulic conductivity = 2.00 – 6.30 mm/s) represent 19.8%, 25%, and 8% of watershed coverage, respectively. Soil type is found to be the main controlling factor of soil moisture distribution in the watershed (see section 4.1). As the soil type is the main controlling factor of the soil moisture distribution in the watershed and as GEOtop model is reasonably reproducing soil moistures at all the experimental sites for surface and deep soil layers, the GEOtop ability to reproduce the spatial patterns of soil moistures for the whole watershed is trusted, and the model results can be taken with high confidence to validate ESTAR soil moisture products.

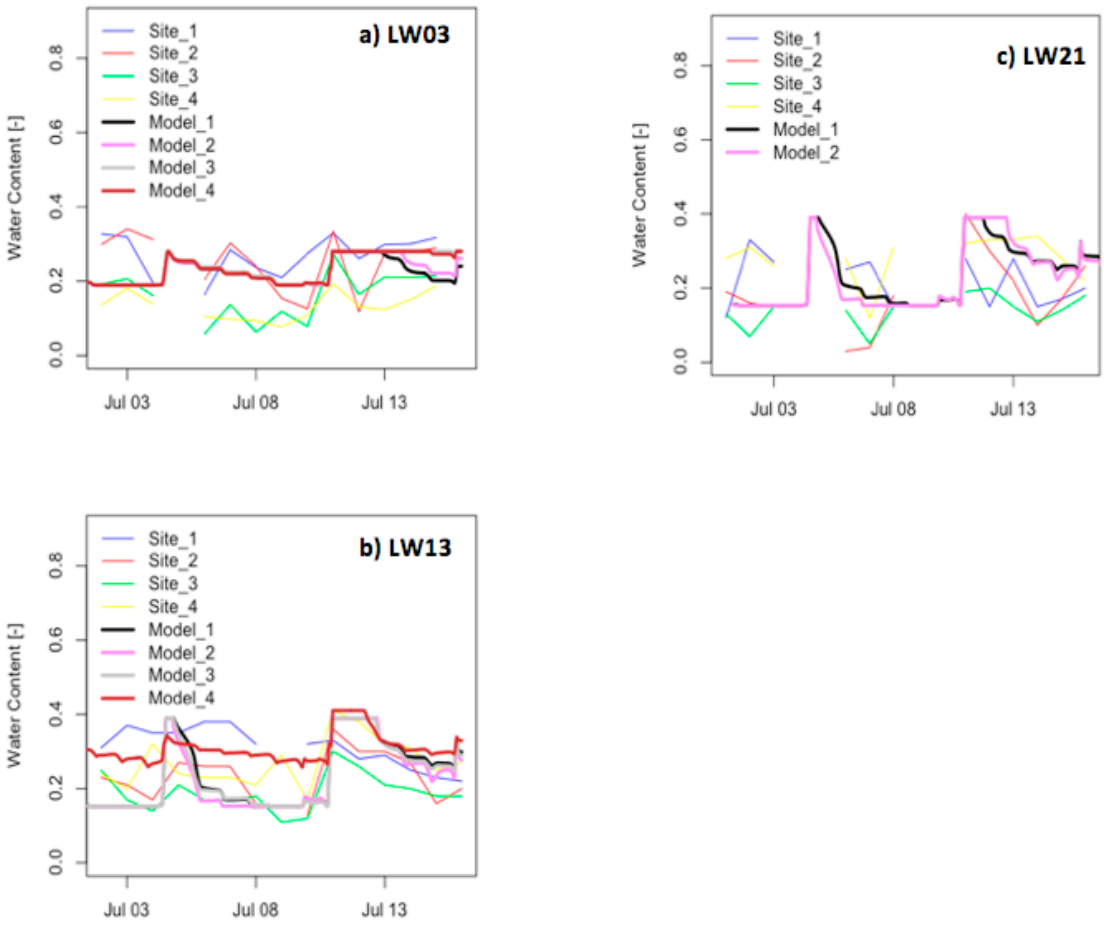

Figure 2.9: Simulated and measured soil moisture of the top 5cm soil layer at: a) LW03, b) LW13, and c) LW21 ground-based measurement sites. The continuous thick lines are the simulated soil moistures. The thin lines are the soil moisture measurements. Thin lines are often broken because of missing measurements. The plot shows that the simulated soil moistures have the same trends of the measurements and within the measurement range.

Table 2.3: Landuse and soil textures at the ground-based measurement sites

Site	Landuse type	Soil texture
LW02	Alfalfa	*Sandy loam
LW03	Bare soil, forage, and pasture	**Sandy loam
LW13	Forage, pasture and urban	***Silt loam
LW21	Pasture, urban, and wheat	****Silt loam

*Sandy loam (soil type 13 - hydraulic conductivity = 2.00 - 6.30 mm/s)

**Sandy loam (soil type 13 - hydraulic conductivity = 2.00 - 6.30 mm/s)

***Silt loam (soil type 8 - hydraulic conductivity = 0.63 - 2.00 mm/s, and soil type 15 - hydraulic conductivity = 2.00 – 6.30 mm/s)

****Silt loam (soil type 8 - hydraulic conductivity = 0.63 - 2.00 mm/s)

2.6 Conclusion

In this chapter, we use the comprehensive field data collected during the SGP97 in the Little Washita watershed (583 km^2) to fully calibrate the physically-based distributed hydrological model, GEOtop (Rigon et al. 2006). The model is constrained by meteorological data from 45 stations and the model runs once at watershed scale for the period from July 1 to August 30, 1997. Results show that the model and is reasonably reproducing energy fluxes (latent heat, sensible heat, ground heat, and net radiation), soil temperature profiles up to 60cm depth from the ground surface at different locations, volumetric soil moisture profiles up to 60cm depth from the ground surface at different locations, and streamflow at the watershed outlet with acceptable accuracies. Therefore, the model ability to produce spatial soil moisture is trusted and the model can be used to validate ESTAR soil moistures.

3 Model validation using Southern Great Plains 1999 (SGP99) hydrology experiment dataset

The purpose of this chapter is to validate GEOtop model using the comprehensive ground-based measurements that was collected during the SGP99. GEOtop model was calibrated using the comprehensive dataset that was collect during the SGP97 (see chapter 2). The model is initialized and driven by meteorological forcings taken at an hourly time step from 44 meteorological stations. Results show that the model is reasonably validated for energy fluxes (latent heat, sensible heat, ground heat, and net radiation), soil temperatures, soil moistures, and streamflows at the watershed outlet. Once the model is validated, the model can be use to validate ESTAR soil moisture.

3.1 Model initialization and setup

All the calibrated parameters that were obtained during the SGP97 for the GEOtop model are kept fixed, except the initial soil water pressure, and the initial soil temperatures. Furthermore, the coefficient of the law of the uniform of the motion of the surface, C_m, is slightly modified for some landuses to account for possible landuse changes. The initial soil water pressures are obtained by running the GEOtop model several times until the hydrological equilibrium of the watershed is reached. The model runs for the period from July 5 to 31, 1999, and the GEOtop model is driven by atmospheric forcings taken at an hourly time step from 44 meteorological stations (Fig. 1.1), excluding Ninnekah station, after performing quality control. The DEM and all other geomorphological maps that are used in the model have 200m grid resolutions; same grid resolutions used for the SGP97. At LW02, LW04, LW05, LW06, LW08, LW09, LW11, LW12, LW13, LW14, LW21, LW22, and LW23 experimental sites (Fig. 3.1), the model is validated for sensible heat, latent heat, ground heat, net radiation, soil temperatures at 10cm depth, streamflows at the watershed outlet (USGS stream gage # 07327550), and soil moistures for the top 5cm soil layer. During the SGP99, and at each

experimental site, the soil moistures were measured for the layers 2.5 - 5cm and 0 - 5cm, and the mean soil moisture was estimated for each depth of the experimental sites. In this study, for each experimental site, the measured soil moisture for the top 5cm soil layer is obtained by taking the average soil moistures measured at the layers 2.5 - 5cm and 0 - 5cm. The measured soil moistures at these layers are gravimetric. The gravimetric soil moisture, G, is defined as follows:

$$G = \frac{M_w}{M_t} \tag{3.1}$$

Where M_w is the weight of water, and M_t is the overall weight of the soil.
The gravimetric soil moistures have to be converted to volumetric soil moistures to be compared to the model results. Volumetric soil moistures, θ, is defined as follows:

$$\theta = \frac{V_w}{V_t} \tag{3.2}$$

Where V_w is the volume of water, and V_t is total volume of the soil.

The gravimetric soil moistures are converted to volumetric soil moistures by multiplying the gravimetric soil moistures by the specific gravity of the soils. The specific gravity, SG, is defined as follows:

$$SG = \frac{\rho_s}{\rho_w} \tag{3.3}$$

Where ρ_s is the density of soil sample, and ρ_w is the density of water.

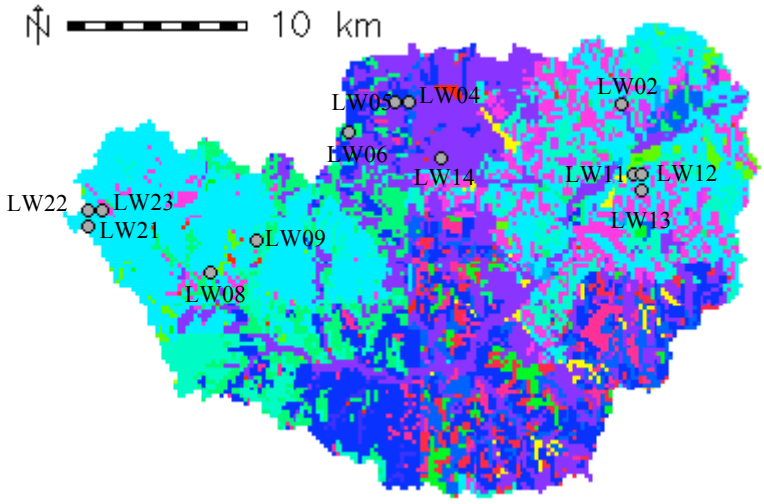

Figure 3.1: Little Washita experimental sites on soil type map of the watershed, the map has 200m-grid resolution.

3.2 Results and discussions

3.2.1 Simulated surface fluxes

The surface fluxes: sensible heat, latent heat, ground heat and net radiation are reasonably simulated at LW08 and LW21 experimental sites, as shown in figures 3.2 and 3.3, respectively. The precise locations at LW08 and LW21, for which the heat fluxes were measured, were not reported in the experiment, but we knew coordinates of some locations inside LW08 and LW21 experimental sites, and we simulated the heat fluxes at these known locations and we compare the simulated heat fluxes to the measurements.

Figures 3.2 and 3.3 show that the simulated latent heat fluxes increase as soil moisture increases, resulting on large amount of latent heat flux on July 10, for which there was rainfall event. To complete the energy balance, this large amount of latent heat flux has to be counterbalanced by sensible heat and ground heat. As shown in Figures 3.2 and 3.3, the sensible heat and ground heat have counterbalanced the latent heat on July 10.

From the figures it appears that the model is fairly reproducing the diurnal cycles of heat fluxes, with often little differences, and that the simulated and the measured heat fluxes have similar trends. The differences between the simulated and the measured heat

fluxes is most likely due to the mismatch in locations between the measured and the simulated heat fluxes; measured and the simulated heat fluxes most likely are in different locations inside the experimental sites. Even though, the differences might be smaller if errors in the measurements have to be considered.

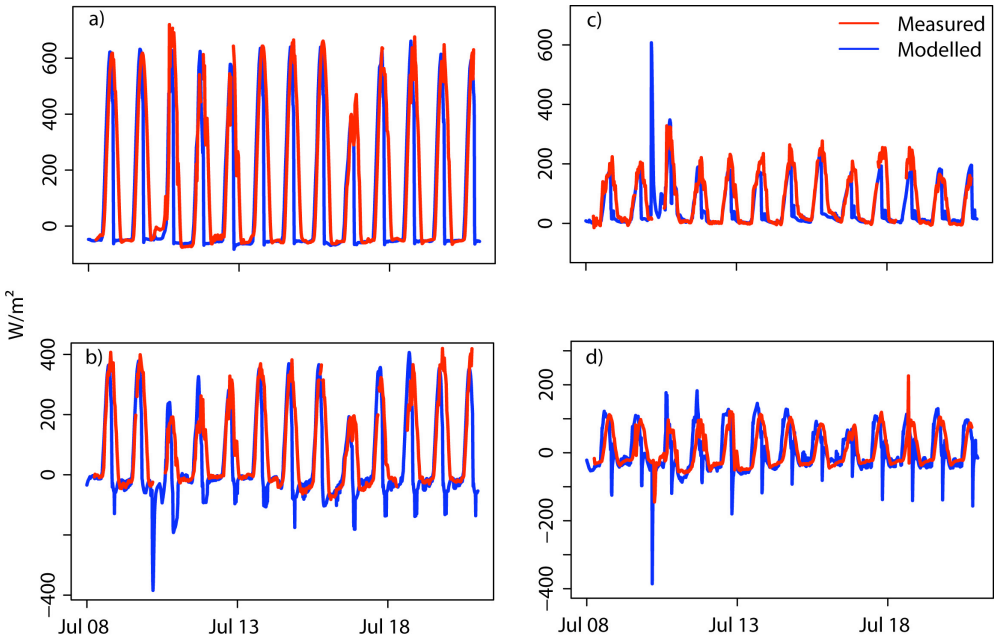

Figure 3.2: Simulated and measured heat fluxes at LW08 experimental site, for: a) Net radiation, b) Sensible heat, c) Latent heat, and d) Ground heat.

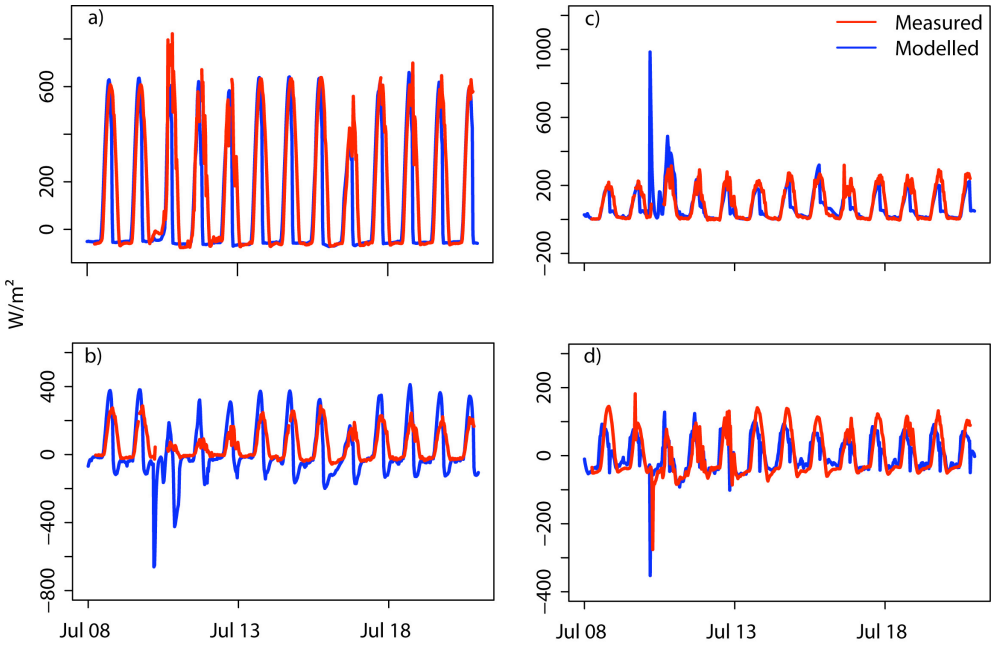

Figure 3.3: Simulated and measured heat fluxes at LW21 experimental site, for: a) Net radiation, b) Sensible heat, c) Latent heat, and d) Ground heat.

3.2.2 Simulated soil temperatures

Figure 3.4 shows the measured and the simulated soil temperatures at 10cm depth at LW02, LW06, LW09, LW12, and LW14 experimental sites. Again, the precise locations of the measured temperatures at each experimental site were not reported in the experiment, but locations of some points inside each experimental site are known, and the soil temperatures are simulated at these known locations, and the simulated soil temperatures are compared to the measurements.

Although the measured soil temperature time series are short, the model is reasonably reproducing the soil temperatures measurements; at least the mean soil temperatures, at all the experimental sites. This indicates that the GEOtop model is capable of simulating soil temperatures for deep soil layers, and indicates that the GEOtop model is implicitly capable of simulating shallow soil temperatures, as shown during the SGP97 (see chapter 2). Therefore, the model capability for reproducing heat fluxes and soil temperatures is trusted.

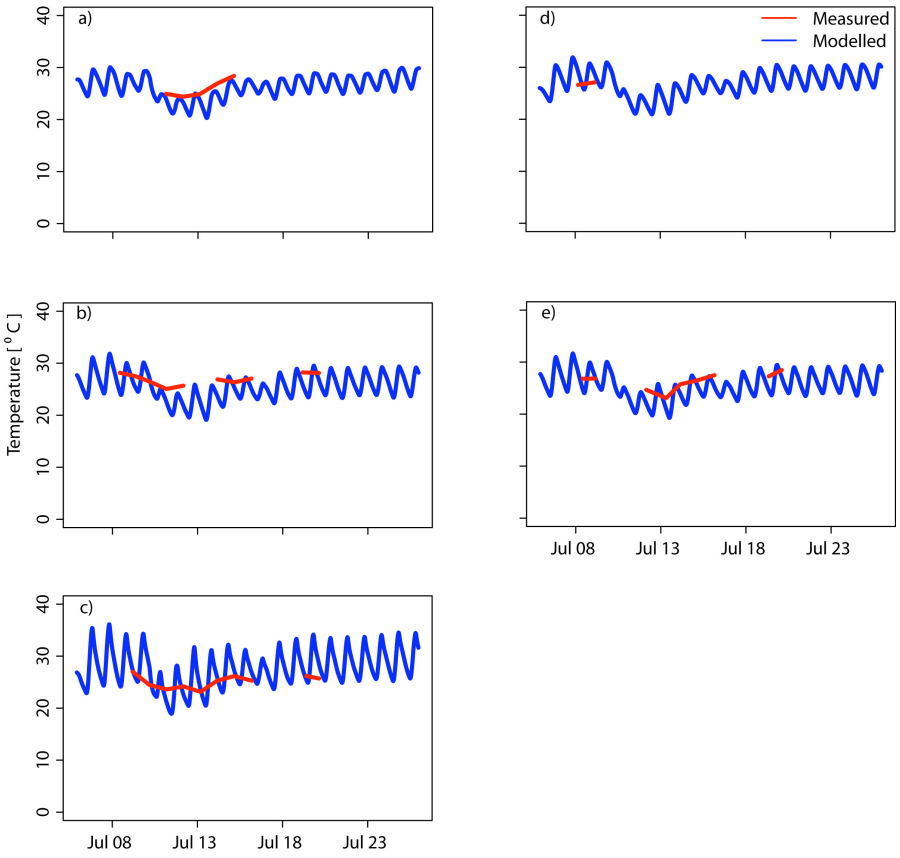

Figure 3.4: Simulated and measured soil temperature at 10cm depth at: a) LW02, b) LW06, c) LW09, d) LW12, and e) LW14.

3.2.3 Simulated soil moistures

At each experimental site in the Little Washita watershed, gravimetric soil moistures (see equation 3.1) were measured for two layers: 2.5 - 5cm and 0 - 5cm from the ground surface, and the soil moisture was estimated for each layer of the experimental sites. In this study, the soil moisture of the top 5cm soil layer is obtained by taking the average soil moistures measured for the layers 2.5 - 5cm and 0 - 5cm, and then, the gravimetric soil moistures are converted to volumetric soil moistures.

Although many soil types could be available at each experimental site, only one value of soil specific gravity has been assigned for each experimental site. The mean measured bulk density of the soil for each experimental site was measured during the experiment. As the density of water is assumed to be $1 gm/cm^3$, the soil specific gravity (see equation 3.3) equals to the soil mean bulk density. The volumetric soil moistures (see equation 3.2) are obtained by multiplying the gravimetric soil moistures by the soil specific gravity.

At each experimental site, coordinates of some points are known, and the soil moistures are simulated at these known points and named Model_1, Model_2, and Model_3. The simulated soil moistures are taken at 2.5cm depth. Then the simulated soil moistures are compared to the aggregated measured gravimetric soil moistures at the corresponding experimental site after converting the gravimetric soil moistures to volumetric soil moistures.

Figure 3.5 illustrates the simulated and the measured volumetric soil moistures for the top 5cm soil layer at LW04, LW05, LW08, LW09, LW11, LW12, LW13, LW21, LW22, and LW23 experimental sites. At each experimental site in the Little Washita watershed, the measured soil specific gravity that is used in this study is shown in table 3.1. As shown in figure 3.5, it is evident that the GEOtop model is fairly simulating the soil moisture measurements at each experimental site. Although the measured soil moistures are the averaged values of soil moistures for the top 5cm soil layer for each individual experimental site, the differences between the simulated and the measured soil moistures are quite small. Moreover, the soil moisture of the top 5cm soil layer is obtained by averaging the soil moisture measurements for the layers 2.5 - 5cm and 0 - 5cm.

The model is fairly reproducing the soil moisture measurements at different locations across the watershed (Fig. 3.1) and these locations lay on different soil types, landuses,

and elevations, implying that the model is capable of simulating soil moistures for the whole Little Washita watershed.

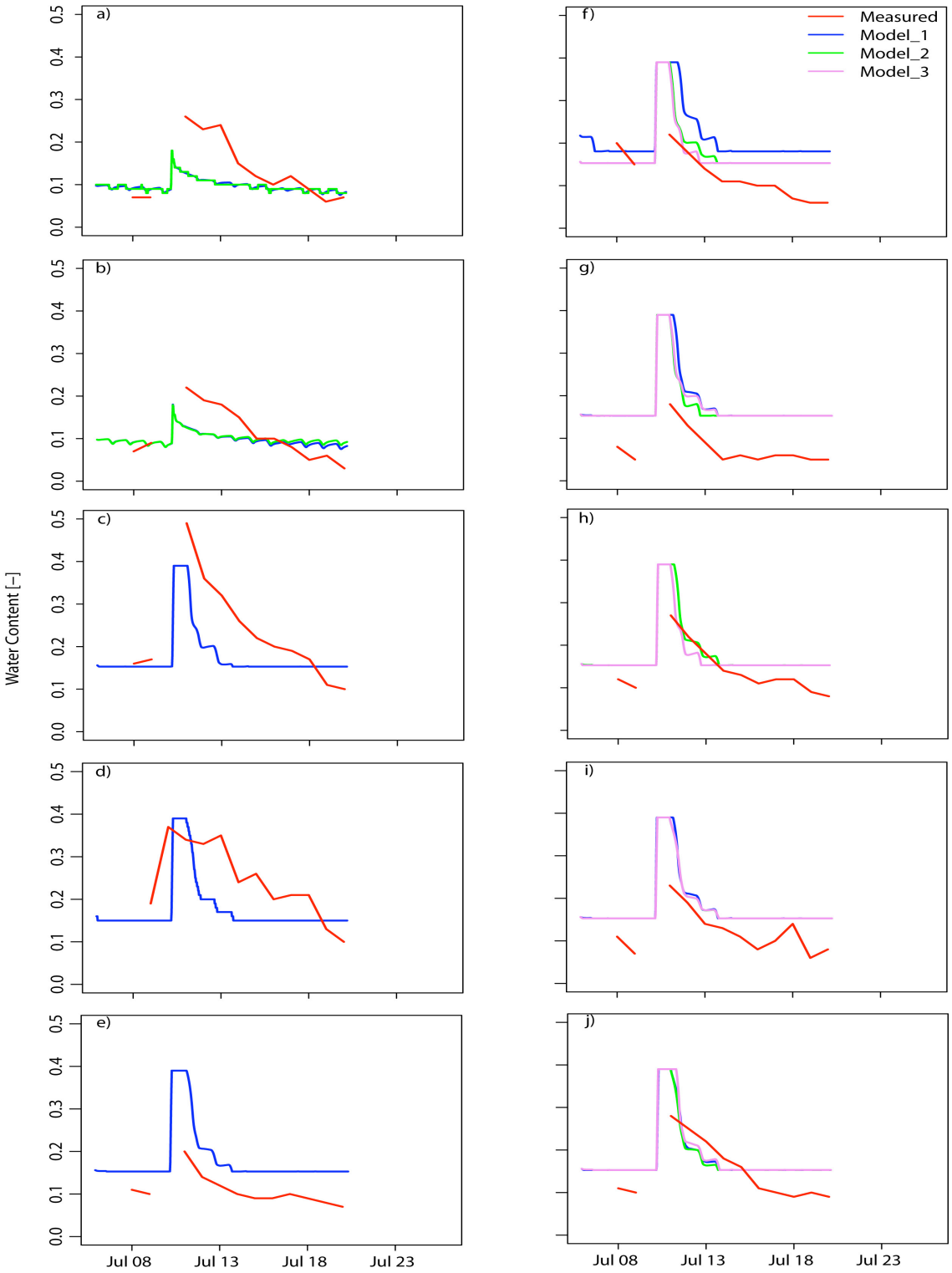

Figure 3.5: Simulated and measured volumetric soil moistures for the top 5cm soil layer at: a) LW04, b) LW05, c) LW08, d) LW09, e) LW11, f) LW12, g) LW13, h) LW21, i) LW22, and j) LW23

Table 3.1: Measured soil specific gravity for the Little Washita experimental sites

Little Washita site ID	Soil specific gravity [-]
LW04	1.41
LW05	1.42
LW08	1.17
LW09	1.19
LW11	1.15
LW12	1.19
LW13	1.2
LW21	1.19
LW22	0.95
LW23	1.16

3.2.4 Simulated streamflows

Figure 3.6 shows the simulated and measured streamflows during the validation period; SGP99, at which there was rainfall event on July 10. Both simulated and measured streamflows are printed every 15minutes. The figure also shows the total precipitation that falls in the watershed during the validation period. The model is perfectly capturing the peakflow. In addition, the model is reasonably simulating the base flows. However, the discharge recession curve of the measurements is not well simulated by the model, and this can have significant effect on the model performance. For the simulated and measured streamflows, the NSE (equation 2.2) is calculated to be 0.231, while the calculated normalized bias (equation 2.3) is 0.049. This low value of NSE is mainly due to the fact that the model is not well simulating the discharge recession curve of the measurements. From the figure it is clear that the simulated water volume is less than the measured volume. This means either the measured precipitation that subsequently used for the simulations is underestimated or there is pre-storm water has been released from reservoirs. The former is not likely to make the difference in water volume since the precipitation is measured from dense network. The latter is likely to make the

difference in water volume since there was storm on July 1. In the watershed there are about 42 flow retarding structures (FRSs) used for flood control during precipitation storms, and the released water from FRSs lasts some days after the storms (Allen and Naney 1991; Tortorelli and Bergman 1985).

From all the above simulations, it is evident that the GEOtop model is able to reproduce the soil moistures that were measured at different locations across the watershed: LW04, LW05, LW08, LW09, LW11, LW12, LW13, LW21, LW22, and LW23 experimental sites (Fig. 3.5). In addition, the model is reasonably simulating the sensible heat, latent heat, net radiation and ground heat fluxes at LW08 and LW21 experimental sites, and is reasonably simulating the temperature measurements for deep soil layers at LW02, LW06, LW09, LW12, and LW14 experimental sites.

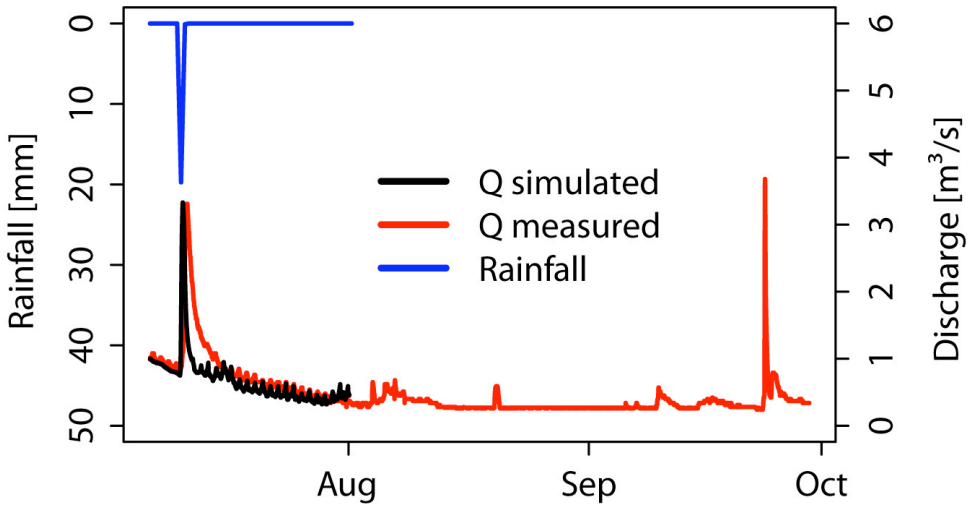

Figure 3.6: Simulated and measured streamflows at the watershed outlet, and the watershed total rainfall.

3.3 Conclusion

The comprehensive field data collected during the SGP99 in the Little Washita watershed (583 km^2) is used to validate the GEOtop model that was already calibrated using the SGP97 dataset (see chapter 2). The model is forced by meteorological forcing data from dense network (see Fig. 1.1) and the model runs once at watershed scale considering all water and energy balance components. Results show that the model is

reasonably validated for energy fluxes (latent heat, sensible heat, ground heat, and net radiation), soil temperatures at different locations, volumetric soil moistures at different locations, and streamflows at the watershed outlet. Therefore, the model can be used to validate ESTAR soil moistures.

4 Simulated and ESTAR soil moisture patterns during SGPs

Simulated and ESTAR soil moisture patterns obtained during the SGP97 and SGP99 in the Little Washita watershed (583 km^2), Oklahoma, USA, are studied. Do both GEOtop and ESTAR give the same patterns? Can the information coming from the two sources be combined to obtain better results? Can the biases observed in ESTAR be corrected? First we compared the spatial patterns then we calculated their statistics, followed by investigating the relationships vegetation, surface roughness, topography, and ESTAR soil moisture, and finally investigating the relationships brightness temperatures, soil temperatures and soil moistures.

GEOtop and ESTAR give different spatial patterns. GEOtop spatial patterns showed to be more realistic then ESTAR patterns. No well-defined relationships between GEOtop simulations and ESTAR hinder the use of combining ESTAR estimates and GEOtop simulations to obtain better estimates of soil moistures.

4.1 Simulated and ESTAR soil moisture patterns during SGP97

4.1.1 Comparison between simulated and ESTAR soil moisture patterns

We compare the spatial soil moisture patterns obtained from GEOtop simulations and ESTAR estimates for the days at which we have ESTAR estimates. Figure 4.1 shows the comparison between simulated and ESTAR soil moistures for July 1, 2, 3, 11, 12, 13, 14, and 16, 1997 and for the top 5cm soil layer. For all the days of the comparison, there are some differences between GEOtop simulations and ESTAR estimates. For relatively dry soil (July 1 - 4), ESTAR estimates and GEOtop simulated soil moistures are comparable, but for wet conditions (July 11 - 16), ESTAR soil moistures are higher than the simulated soil moistures. The simulated soil moisture maps always look very similar to the watershed soil type map (compares Fig. 1.2c and 4.1), while ESTAR estimates did not show any similarity to the watershed soil type map. From the comparison between GEOtop simulations and ESTAR estimates, ESTAR smoothes soil moistures patterns, and this partly due to the low resolution of ESTAR maps; 800m

resolution, while GEOtop simulations have been carried out for 200m resolutions. Furthermore, ESTAR estimates are also subjected to some errors from inverting brightness temperatures to volumetric soil moistures. For all the days of the comparison, ESTAR estimates show zero soil moistures, while GEOtop simulations do not show zero soil moistures. There should be some residual water content given that the smallest soil thickness in the watershed is about 250 mm (see Fig. 1.2b), indicating that GEOtop results appear more realistic than ESTAR.

From the simulated soil moistures and for the entire simulation period (July 1 - August 30, 1997) and from the soil moisture measurements, the maximum value of the volumetric soil moisture content at LW02, LW03, LW13 and LW21 sites does not go beyond 0.41. While ESTAR estimates of soil moistures are greater than 0.41 and goes up to 0.73 sometimes for some of the locations. Except for peat soil, no soil has saturated water content of 0.73. In the watershed there is no peat soil (see Fig. 1.2c). Even on July 11, after the heavy rainfall event on July 10, the simulated soil moisture maps look very similar to the watershed soil type map. Therefore, it can be concluded that the soil type controls the soil moisture variability in the watershed, and there are little effects of precipitation distribution as well as the topography. The low effect of topography is partly explained by the gentle slope of the Little Washita watershed, which is in agreement with Bertoldi (2007). We observe that the control of landuse on soil moisture variability is minimal. Our result agrees with Cosh and Brutsaert (1999) finding who concluded that the soil type is the main controlling factor of soil moisture variability in the Little Washita watershed. On the other hand, Bertoldi (2007) and Mohr et al. (2000) concluded that the main controling factor of soil moisture spatial distribution in the watershed is the soil type during dry periods and precipitation during wet periods.

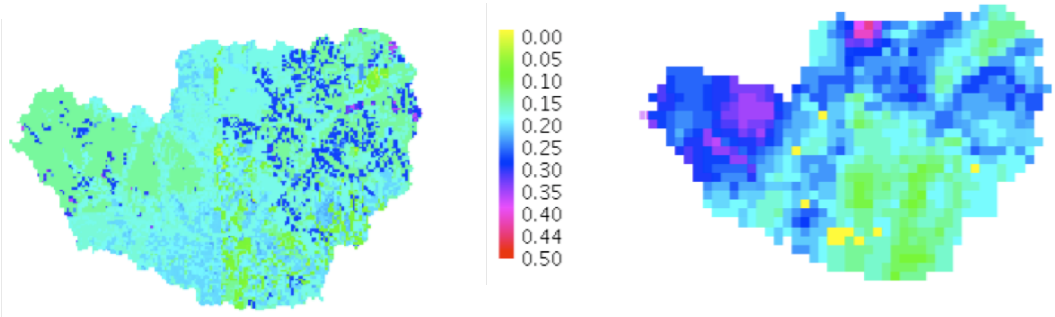

Figure continues in the next page

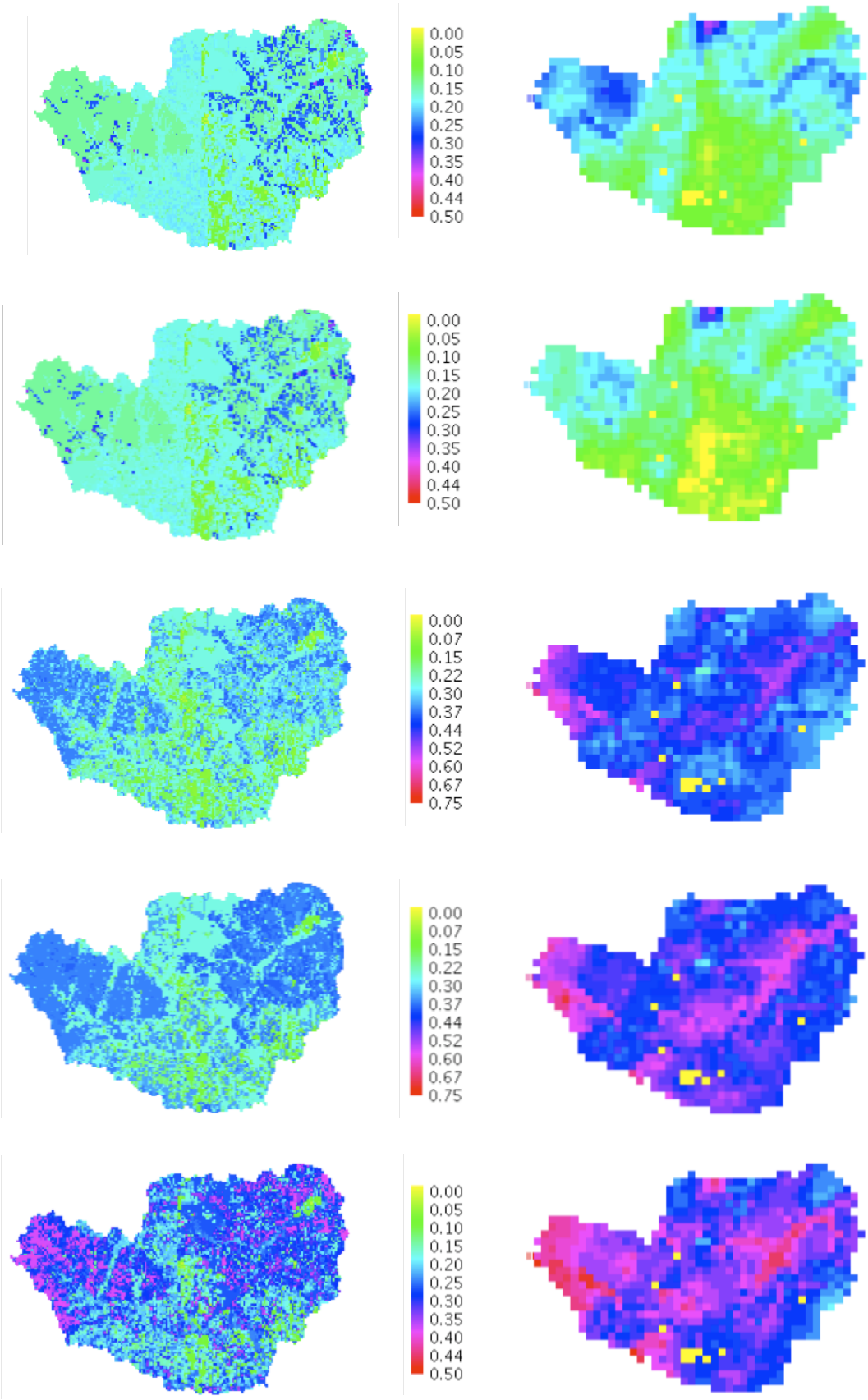

Figure continues in the next page

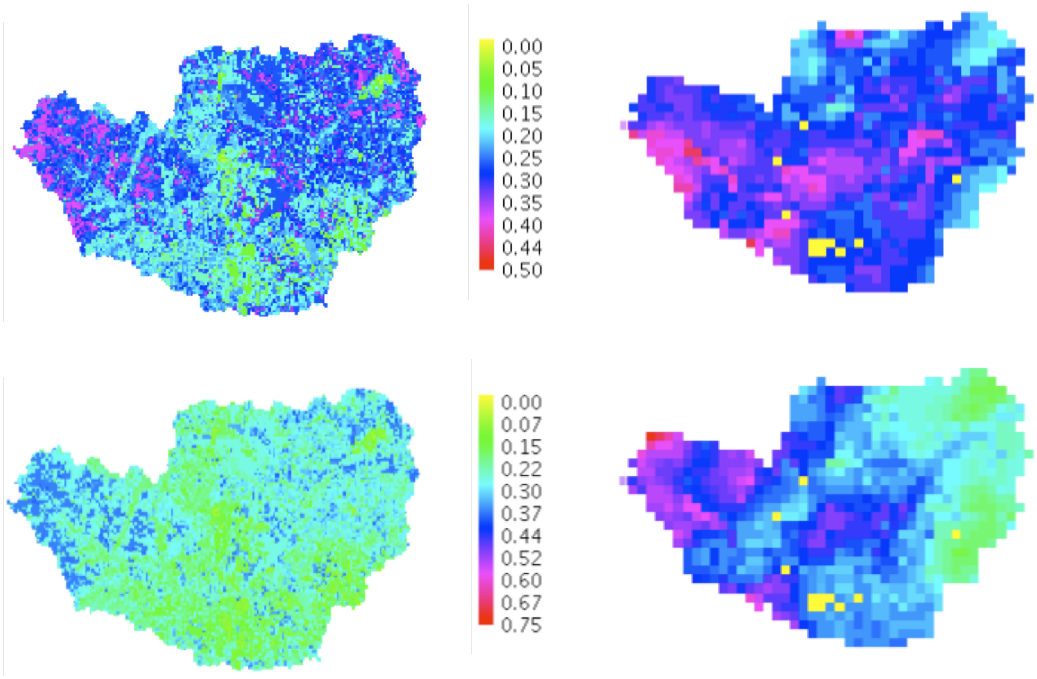

Figure 4.1: Volumetric water content of the top 5cm soil layer for July 1, 2, 3, 11, 12, 13, 14, and 16, 1997, from left to right and from top to bottom, respectively. Each row (couple) refers to a different day. (right) estimated using ESTAR remote sensor. (left) simulated using GEOtop model.

Figure 4.2 shows the spatial mean, spatial standard deviation (STDEV), and spatial coefficient of variation (CV) of soil moisture derived from ESTAR estimates and GEOtop simulations for the entire watershed. ESTAR soil moisture values are higher in the mean than the GEOtop simulations following a rain event, but this discrepancy shrinks as the soil dries. According to ESTAR estimates, the spatial STDEV decreases as the soil dries following a rain event, and increases as the soil wets up. On the contrary, according to GEOtop simulations, the STDEV remains fairly insensitive to changes in soil moisture. For the CV statistic, let us consider only the soil moisture fields whose mean values exceed 0.20 to avoid the unrealistically large values caused by the very small magnitudes of mean soil moisture. Both ESTAR and GEOtop show that the CV increases as the soil dries – this agreement is due to the fact that both have captured the decrease in the spatial mean during the dry-down period following a rain event. The ESTAR estimates show smaller CV values than the GEOtop results, and this can be explained by the higher spatial mean of ESTAR estimates.

Figure 4.2 also shows the spatial correlation, root mean square error (RMSE), and bias for the relationships between ESTAR and simulated soil moistures for the entire watershed. The spatial correlation, RMSE, and bias are obtained after resampling the 200m-model resolution to 800m resolution, to match ESTAR resolution, using JGRASS-GIS (www.jgrass.org) interface. Results show that there is no correlation between ESTAR and simulated soil moistures. Both RMSE and bias are relatively small during relatively dry period (July 1 - 4), and relatively large during the wet period (July 11 - 16). During the wet period, and as soil dries, both RMSE and bias decrease and both increase again as soil wets up.

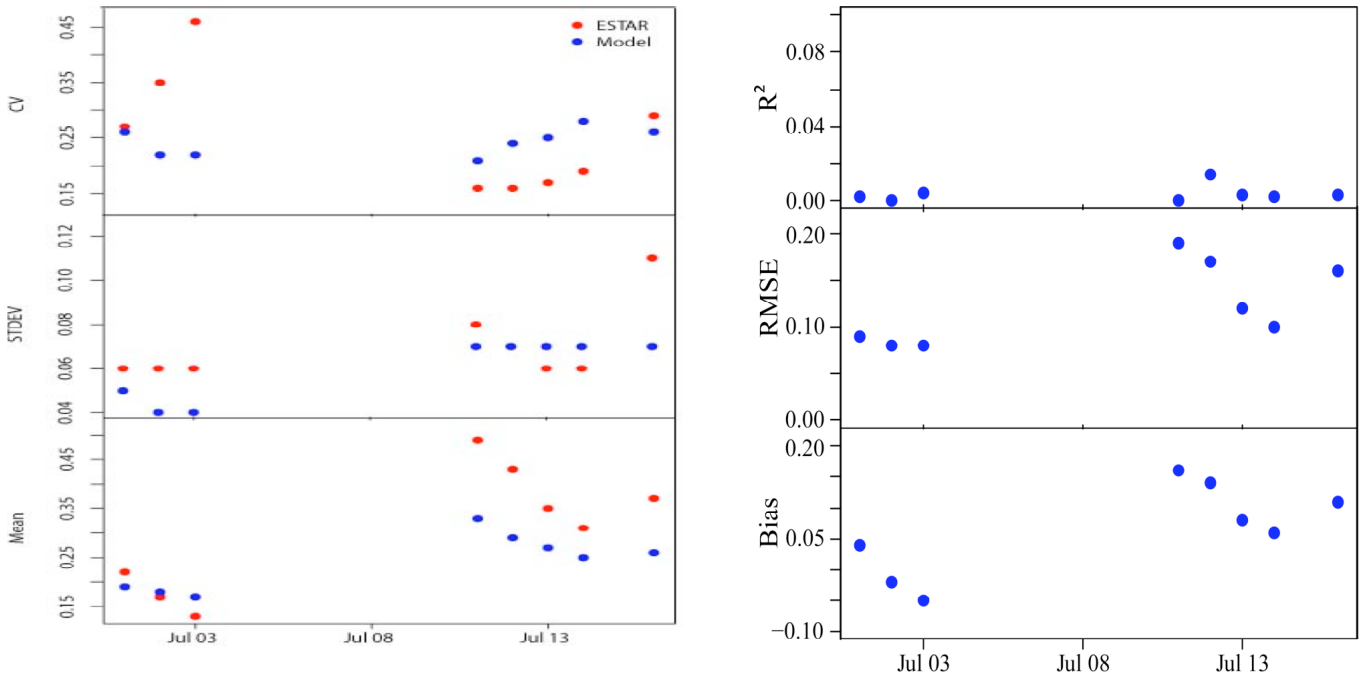

Figure 4.2: Left graph shows the mean, standard deviation and CV for the ESTAR and simulated soil moistures, and right graph shows the root mean square error, bias and coefficient of determination of water content [-] for the relationships between ESTAR estimates and GEOtop simulations for the entire watershed and for the top 5cm soil layer.

In order to investigate the differences between the simulated and ESTAR soil moistures, the statistical properties (e.g., mean, STDEV, and CV) of sandy loam (soil type 13 - hydraulic conductivity = 2.00 - 6.30 mm/s), silt loam (soil type 8 - hydraulic conductivity = 0.63 - 2.00 mm/s), sandy loam (soil type 6 - hydraulic conductivity = 0.63 – 2.00 mm/s) and loam soil (soil type 7 - hydraulic conductivity = 0.63 – 2.00 mm/s) are characterized. As the soil type is the main controlling factor of the soil moisture distribution in the watershed, and to avoid the smoothness of soil moisture statistical properties resulting from averaging the watershed statistical properties, the statistical properties for the all above-mentioned soil types are characterized. These soil types are dominant in the watershed and represent 19.8%, 25%, 7%, and 10% of the watershed coverage, respectively. Here only the statistical properties of silt loam (soil type 8 - hydraulic conductivity = 0.63 - 2.00 mm/s) and sandy loam (soil type 13 - hydraulic conductivity = 2.00 - 6.30 mm/s) are shown (Fig. 4.3). As shown in figure 4.4, sandy loam lies along the main river and in the central north part of the watershed, while silt loam lies in the northeast and northwest parts.

Figure 4.3 presents the spatial mean, spatial STDEV, and spatial CV of soil moisture derived from ESTAR estimates and GEOtop simulations, over the sandy loam and silt loam parts of the watershed. With regard to the spatial mean, ESTAR estimates are higher than the corresponding GEOtop simulations, and the discrepancy gets smaller at lower moisture contents, for both soil types. With regard to the spatial STDEV, ESTAR estimates give higher values than GEOtop simulations, for both soil types. For the sandy loam soil, ESTAR estimates indicate that the STDEV decreases as the soil dries down, while the contrary is shown by the GEOtop simulations. For the silt loam soil, ESTAR estimates indicate that the STDEV decreases as the soil dries down, while GEOtop simulations do not indicate a monotonic pattern of STDEV during dry-down. With regard to CV, ESTAR estimates are often higher than the GEOtop simulations.

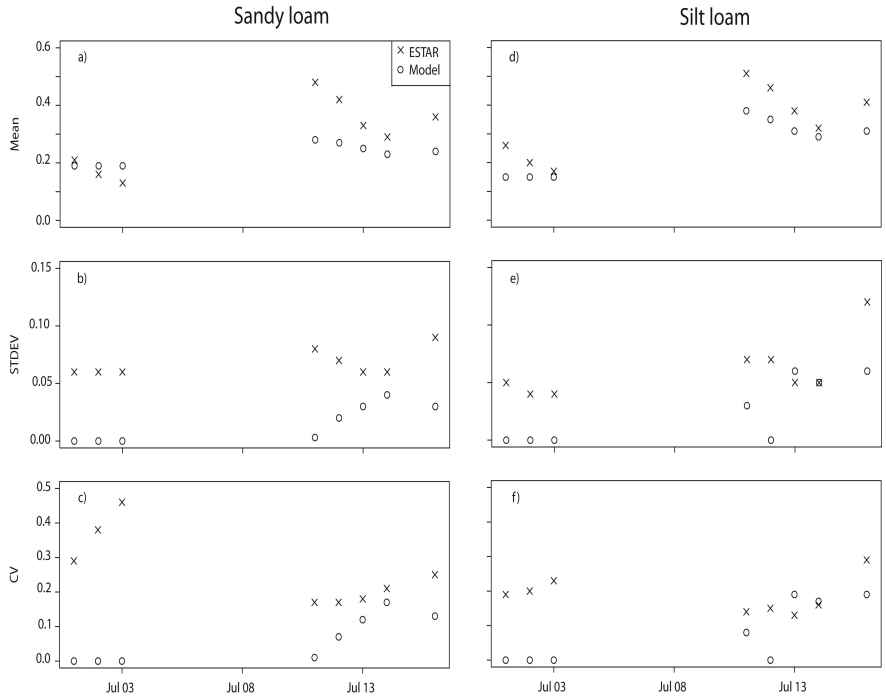

Figure 4.3: Statistical moments of simulated and ESTAR soil moisture time series, for the sandy loam (left) and silt loam (right) soils, and for the top 5cm soil layer. Figures a), b) and c) show the mean soil moisture, soil moisture STDEV, and soil moisture CV for sandy loam soil, respectively, while figures d), e), and f) show the mean soil moisture, soil moisture STDEV and soil moisture CV for silt loam soil, respectively.

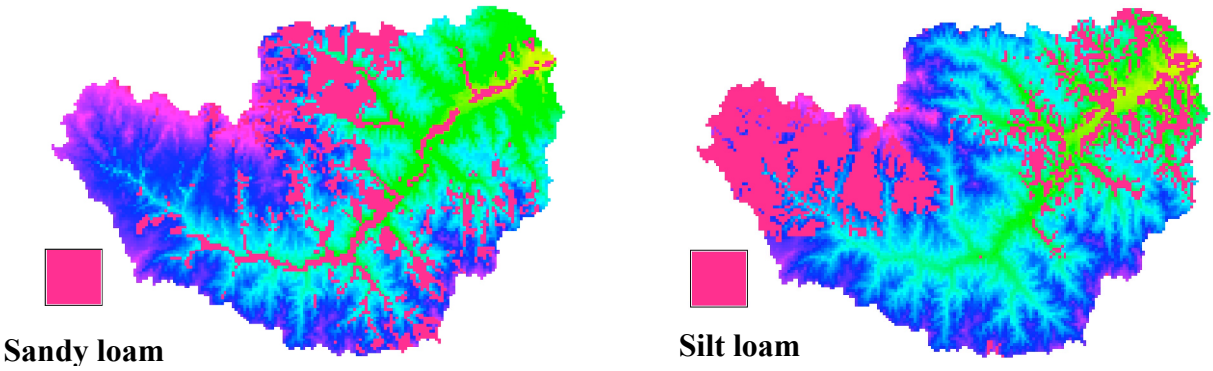

Figure 4.4: Sandy loam (left) and silt loam (right) soils superimposed on the watershed DEM.

4.1.2 The relationships vegetation, surface roughness, topography, and ESTAR soil moisture

To further investigate the differences between the GEOtop simulations and ESTAR soil moistures, we compare the mean soil moisture content obtained from GEOtop simulations and ESTAR estimates for bare soil in a fixed soil type. This is performed to investigate whether the ESTAR measures the soil moisture of vegetation or soil moisture of the soil. In a bare soil, both GEOtop simulations and ESTAR estimates are expected to have the same mean water content if the differences between ESTAR estimates and GEOtop simulations are mainly due to the presence of vegetation. For both GEOtop simulations and ESTAR estimates, we find that the mean soil moisture content for bare soil is similar to the mean soil moisture content of the same soil type under different landuse types, as shown in figures 4.5, and 4.6. This excludes that the differences between ESTAR estimates and GEOtop simulations are not mainly due to the presence of vegetation.

To investigate where and when the ESTAR and the GEOtop give similar spatial soil moisture patterns, the effect of surface roughness on ESTAR soil moisture is investigated for channel network pixels as well as for non-channel pixels in a fixed soil type. For each soil type, the mean soil moisture contents for pixels only inside channel networks and for pixels only outside channel network are computed. Results show that for both GEOtop simulations and ESTAR estimates, the mean soil moisture content, for a particular soil type, for only channel network pixels is similar to the mean soil moisture content for the same soil type considering only non-channel network pixels (Fig. 4.5). This excludes that the differences between ESTAR estimates and GEOtop simulations are not mainly due to differences in surface roughness.

To further investigate where and when the ESTAR and the GEOtop give similar spatial soil moisture patterns, the effect of topography on ESTAR soil moisture is investigated for only concave pixels and for only convex pixels in a fixed soil type. For each soil type, the mean soil moisture contents for only concave pixels and for only convex pixels are computed. For both GEOtop simulations and ESTAR estimates, the mean soil moisture contents, for a certain soil type, for only concave pixels is similar to the mean soil moisture content for the same soil type considering only convex pixels (Figs. 4.5 and 4.6). This excludes that the differences between ESTAR estimates and GEOtop simulations are not mainly due to topography effects.

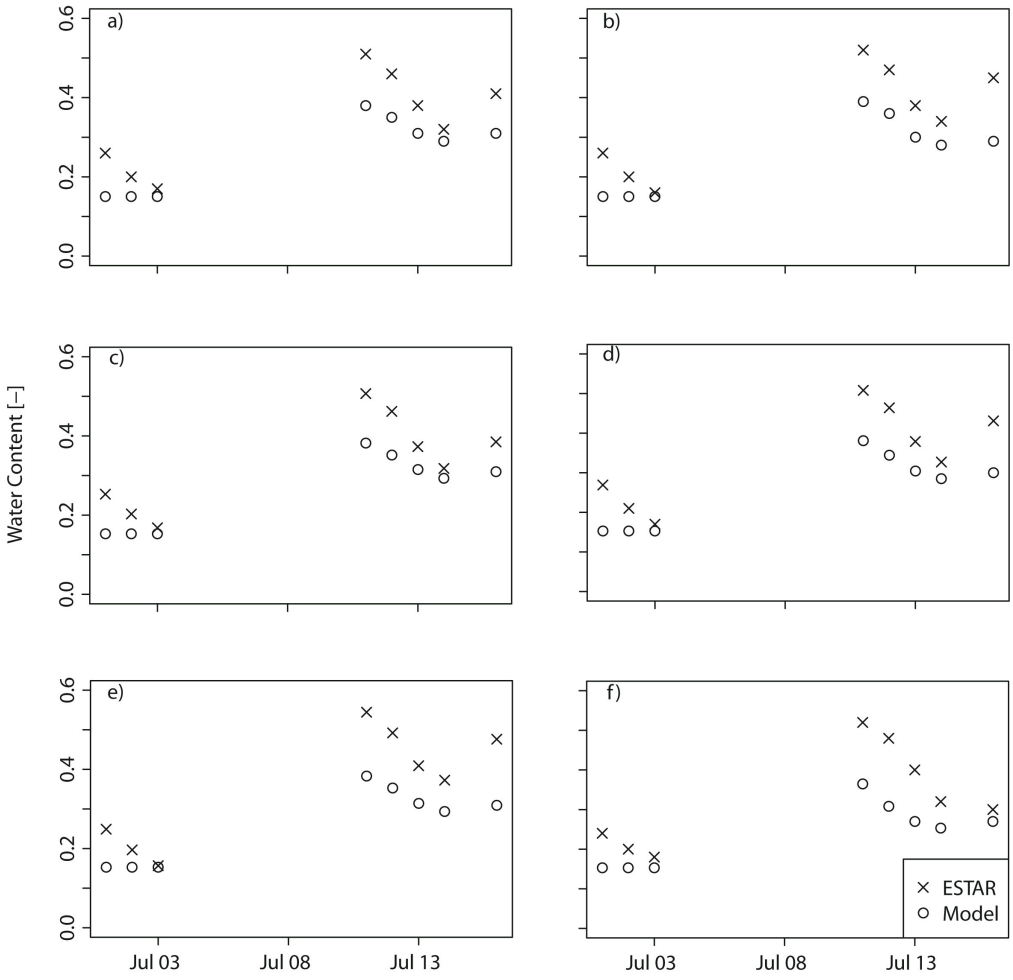

Figure 4.5: Simulated and ESTAR soil moisture content time series for the top 5cm soil layer for: a) Soil moisture content for all pixels of silt loam soil, b) Soil moisture content for silt loam in only bare soil, c) Soil moisture content for silt loam in only concave pixels, d) Soil moisture content for silt loam in only convex pixels, e) Soil moisture content of silt loam only in non-channel network pixels, and f) Soil moisture content for silt loam in only channel network pixels.

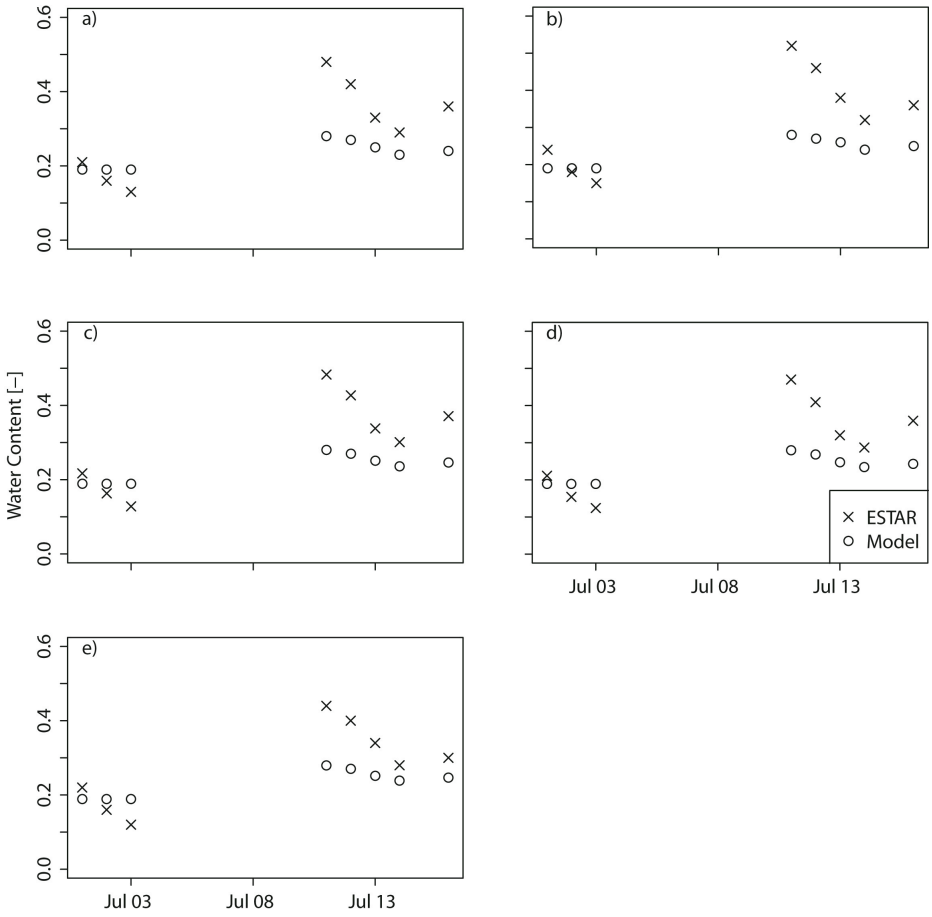

Figure 4.6: Simulated and ESTAR soil moisture content time series for the top 5cm soil layer for: a) Soil moisture content for all pixels of sandy loam soil, b) Soil moisture content for sandy loam in only bare soil, c) Soil moisture content for sandy loam in only concave pixels, d) Soil moisture content for sandy loam in only convex pixels, and e) Soil moisture content of sandy loam in only non-channel network pixels. There are no pixels of ESTAR estimates for only channel network. ESTAR resolution is 800m, while GEOtop simulations have 200m-grid resolution.

As there are little effects of vegetation, surface roughness, and topography on ESTAR soil moistures, we hypothesized that ESTAR soil moistures are influenced by surface runoff and vegetation-intercepted water. Furthermore, we hypothesize that ESTAR is influenced by surface water from irrigation. This hypothesis is supported by the observation that ESTAR estimated exceedingly high values of soil moistures along the channel network. Figure 4.2 shows that for the wet period (July 11 - 16) the minimum difference (RMSE and bias) between ESTAR and simulated soil moistures is on July 14. On this day, which has the minimum surface runoff depth (Fig. 4.7), ESTAR estimates and GEOtop simulations are more comparable than any other day in the wet period. In the dry period (July 1 - 4), ESTAR estimates and GEOtop simulations somehow show comparable soil moisture patterns and show low values of RMSE and bias, as shown in figure 4.2. Figure 4.7 shows the simulated surface runoff depth maps for July 11, 12, 13, 14, and 16, while figure 4.8 shows the simulated intercepted water on vegetation leaves on July 11 and 16. The intercepted water map on July 11 is very similar to the watershed landuse map (Fig. 1.2d). There is no intercepted water on July 12, 13 and 14, since there were no rainfall events on these days.

In the dry period there is no runoff, only streams flows, and the maximum difference (bias) in water content between ESTAR estimates and GEOtop simulations is about 0.05, as shown in figure 4.2. Figure 4.2 shows that on July 11, the difference is large, and the difference decreases as soil dries. The difference increases again on July 16 following the rainfall event on July 15. Along the channels, ESTAR shows soil moisture values higher than porosity, and the more higher when more wetter is the period.

Comparing ESTAR soil moisture maps in the wet period with the corresponding surface runoff depth maps, it is evident that the estimated ESTAR soil moistures are higher than the GEOtop simulations when the surface runoff depths and surface runoff coverage are high, and the difference between ESTAR estimates and GEOtop simulations decreases as the surface runoff depths and surface runoff coverage decrease.

Similarly, comparing ESTAR soil moisture maps in the wet period with the corresponding intercepted water maps, it is evident that the estimated ESTAR soil moistures are higher than the GEOtop simulations when the intercepted water depths and coverage are high, and the difference between ESTAR estimates and GEOtop simulations decreases as the vegetation-intercepted water and converge decrease. One possible explanation of this is that ESTAR is influenced by vegetation-intercepted water

(Bushara et al. 2010). Furthermore, it is likely that ESTAR is influenced by dew on vegetation leaves.

The surface runoff in the watershed decreases from July 11 to 14, consequently, the areas with high soil moistures detected by ESTAR are decreased. The runoff depths and runoff converge increase again on July 16, resulting on high ESTAR soil moistures in large areas in the watershed. The intercepted water on July 16 (Fig. 4.8) has little effect on ESTAR estimated soil moistures. The little effect of intercepted water on ESTAR soil moisture on July 16 is due to the small depths and coverage of the vegetation-intercepted water.

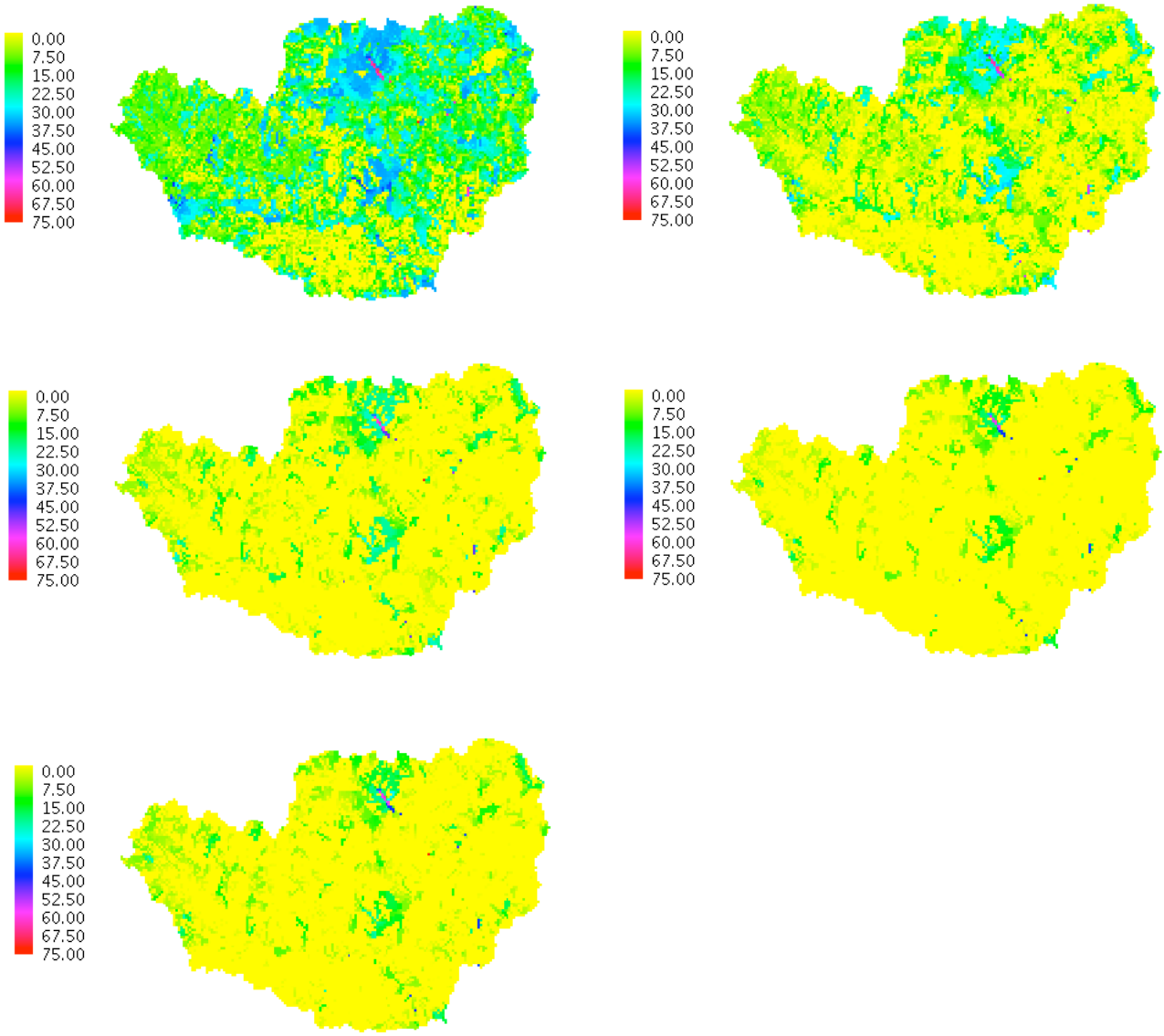

Figure 4.7: Simulated surface runoff depth (mm) on July 11, 12, 13, 14, and 16, 1997, from left to right and from top to bottom, respectively.

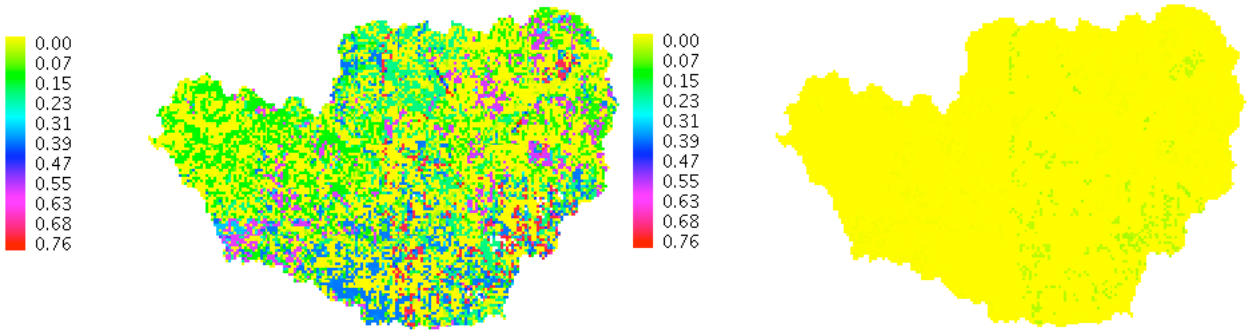

Figure 4.8: Simulated intercepted water on vegetation leaves (mm), on July 11, 1997 (left), and July 16, 1997 (right).

4.1.3 The relationships brightness temperatures, soil temperatures and soil moistures

In this section we investigated the possibility of using soil moistures and soil temperatures for the top 5cm soil layer derived from GEOtop simulations to produce bias-adjusted ESTAR soil moistures.

Figure 4.9 shows the scatter plot of simulated and ESTAR soil moistures for the days at which we have ESTAR measurements fitted with linear models. It is evident that the correlations between simulated and ESTAR soil moistures are very low. Nevertheless, from visual inspection, it appears that there is a better correlation between simulated and ESTAR soil moisture in the wet period (July 11-16) than in the dry period.

Figure 4.10 shows the relationship between the soil moisture derived from GEOtop simulations versus the measured brightness temperature for the whole watershed for different days during the experiment. Jackson et al. (1999) derived an algorithm to estimate soil moistures based on the relationship between the measured volumetric soil moistures and the measured brightness temperatures. In this study, the dry period (July 1 - 4) it evident that there is no defined relationship between the soil moistures derived from GEOtop simulations and the brightness temperatures. The wet period (July 11 - 14) it appears there is a relationship between the soil moistures derived from GEOtop simulations and the measured brightness temperatures. However, this relationship is weak (correlation coefficient in the wet period varies from 0.22 to 0.4). However, If few datapoints were used, as used by Jackson et al. (1999), the correlation between the soil moistures derived from GEOtop simulations and the brightness temperatures is expected

to be very strong. Even in bare soil, in order to eliminate the possible effects of vegetation on the brightness temperatures, there is weak correlation between the soil moistures derived from GEOtop simulations and the measured brightness temperatures (Fig. 4.11), the highest correlation coefficient is 0.5 on July 11. This indicates that the differences between the soil moistures derived from GEOtop simulations and ESTAR estimates are not mainly due to the presence of vegetation. This confirms our previous findings (see section 4.1.2) stating that effects of vegetation on ESTAR soil moistures.

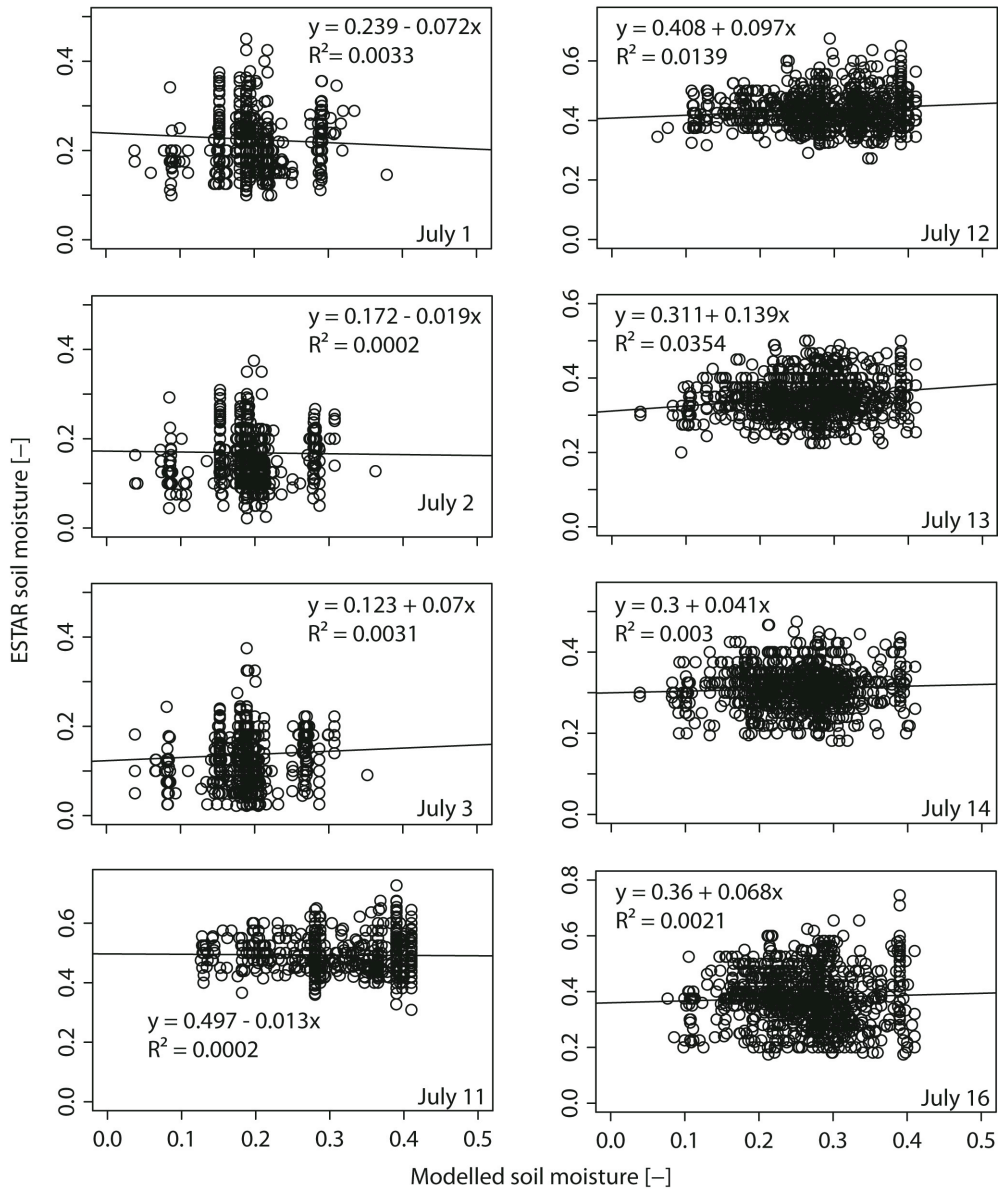

Figure 4.9: Simulated soil moisture versus ESTAR soil moisture for the whole watershed and for the days at which we have ESTAR estimates.

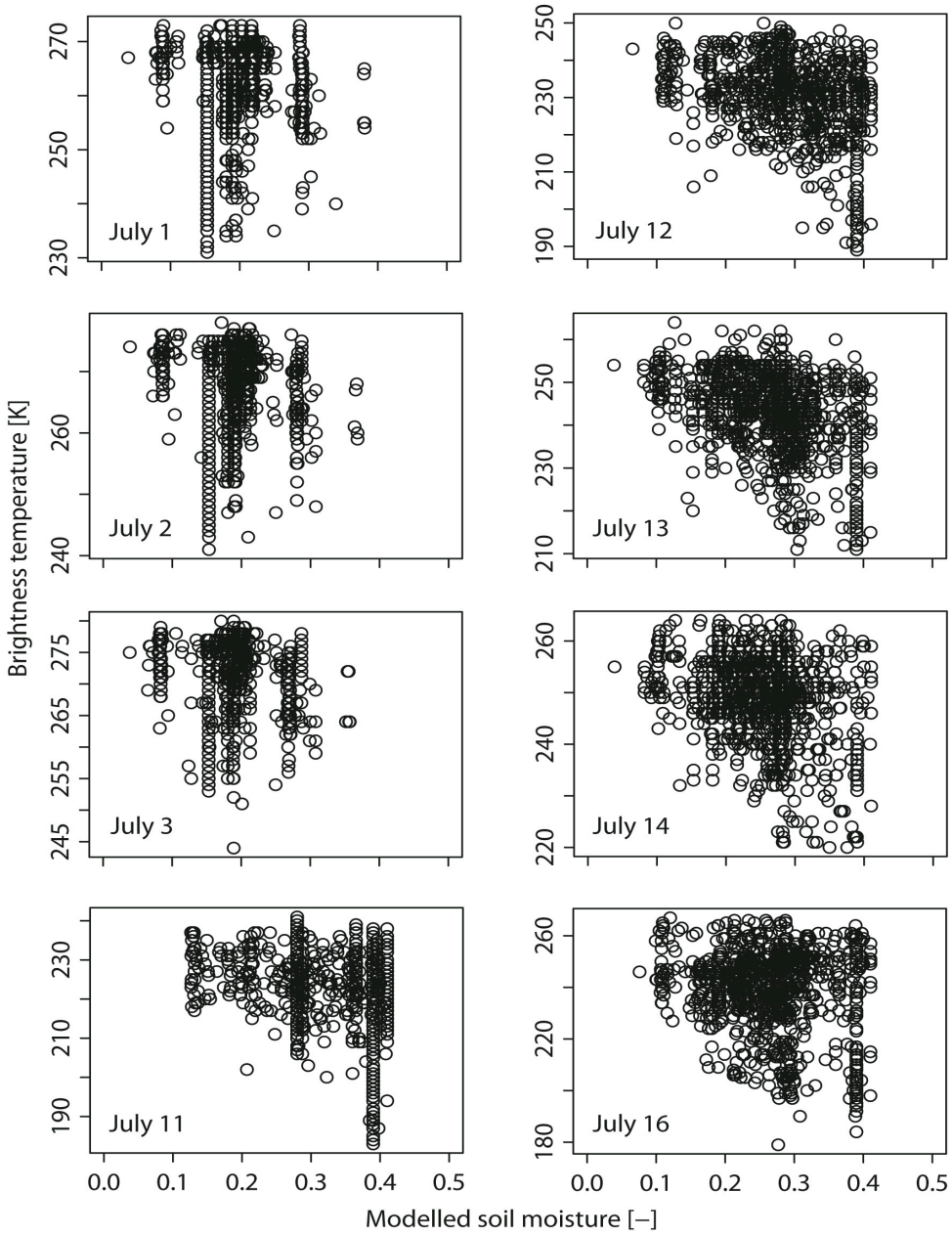

Figure 4.10: Simulated soil moisture [-] versus the measured brightness temperature [K] for the whole watershed.

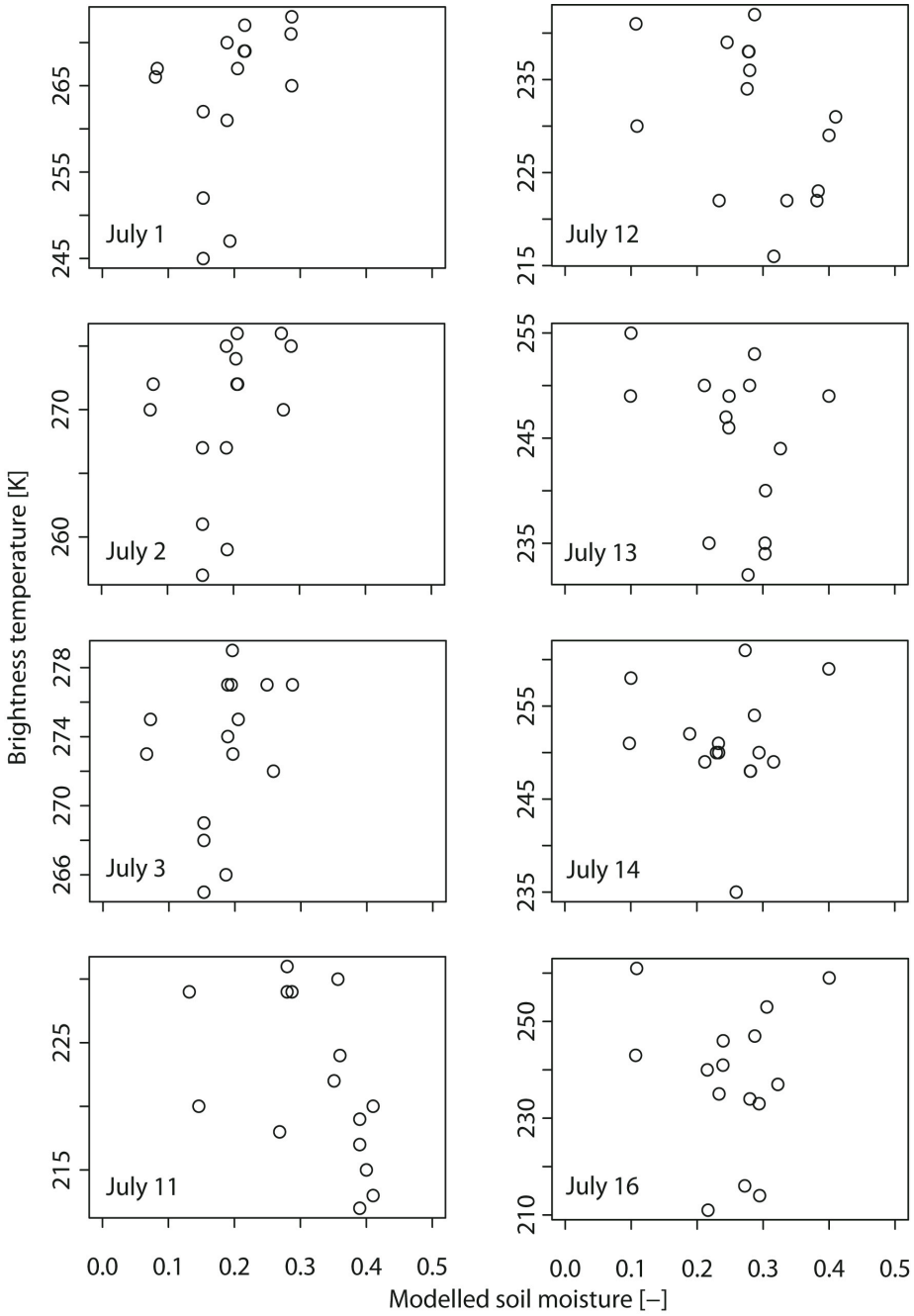

Figure 4.11: Simulated soil moisture [-] versus the measured brightness temperature [K] in bare soil.

Jackson et al. (1999) derived an algorithm for the relationship between the measured brightness temperature and the observed volumetric soil moistures. However, they validated the algorithm for the observed soil moistures only in the range of (0 – 0.4). The algorithm was used to estimate ESTAR soil moistures, based on a relationship between the volumetric soil moisture and the brightness temperature, and ESTAR soil moistures higher than 0.4 were obtained by extrapolation. In order to avoid any uncertainties in ESTAR soil moistures caused by the extrapolation, we compare the ESTAR soil moistures that in the range of (0 – 0.4) with the corresponding soil moistures derived from GEOtop simulations (Fig. 4.12). Even in the wet period, where it appears there is defined relationship between the simulated soil moisture and the measured brightness temperature, there is weak relationship between ESTAR soil moisture and soil moisture derived from GEOtop simulations. The highest correlation coefficient is 0.39 on July 11. This excludes that the differences between the ESTAR soil moistures and the soil moistures derived from GEOtop simulations are not mainly due to the algorithm extrapolation problem.

Figure 4.13 shows the relationship between the simulated soil temperature for the top 5cm soil layer and the corresponding measured brightness temperature. It is evident that there is weak correlation between the simulated soil temperature and the brightness temperature. Furthermore, the simulated soil temperature is higher than the estimated brightness temperature, and that most of brightness temperature values are less than absolute zero ^{0}C (273.15 ^{0}K). The simulated soil temperature varies in a short range compared to the measured brightness temperature. High values of simulated soil temperatures compared to the measured brightness temperatures resulted in low values of emissivities, since the emissivity, ε, is calculated using the following equation:

$$\varepsilon = \frac{T_B}{T} \tag{4.1}$$

Where T_B is the measured brightness temperature, and T is the simulated soil temperature.

During the SGP97, the brightness temperatures were measured for the whole watershed and the brightness temperatures are inverted to volumetric water content. For more details about the brightness temperatures please see LeVine et al. (1994), Jackson et al. (1995), Jackson and LeVine (1996), and Jackson et al. (1999).

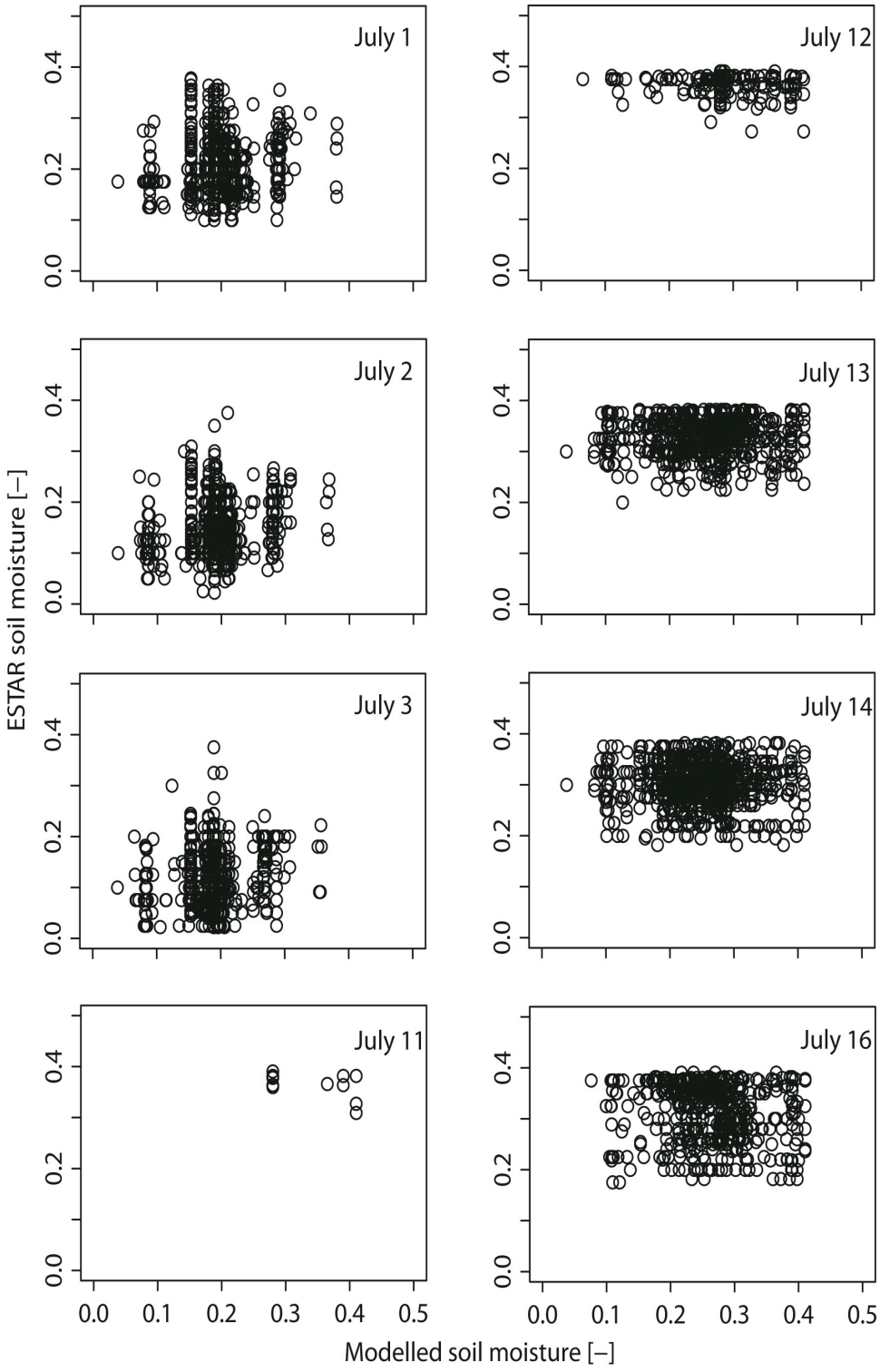

Figure 4.12: Simulated soil moisture [-] versus ESTAR soil moistures [-] that are lower than 0.4.

In order to investigate the effect of vegetation on brightness temperature, we compare the simulated soil temperature for the top 5cm soil layer with the brightness temperature in only bare soil (Fig. 4.14). Results show that the brightness temperature is lower than the simulated soil temperature, and that the simulated soil temperature varies in a short range compared to the brightness temperature. It appears there is upward quadratic relationship between the simulated soil temperature and the measured brightness temperature. The brightness temperature decreases as the simulated soil temperature increases, up to the minima, and increases again as the simulated soil temperature increases. Weak correlation between the simulated soil temperature and the brightness temperature in only bare soil; the highest correlation is 0.39 on July 14, indicates that the weak correlation is not mainly due to the presence of vegetation.

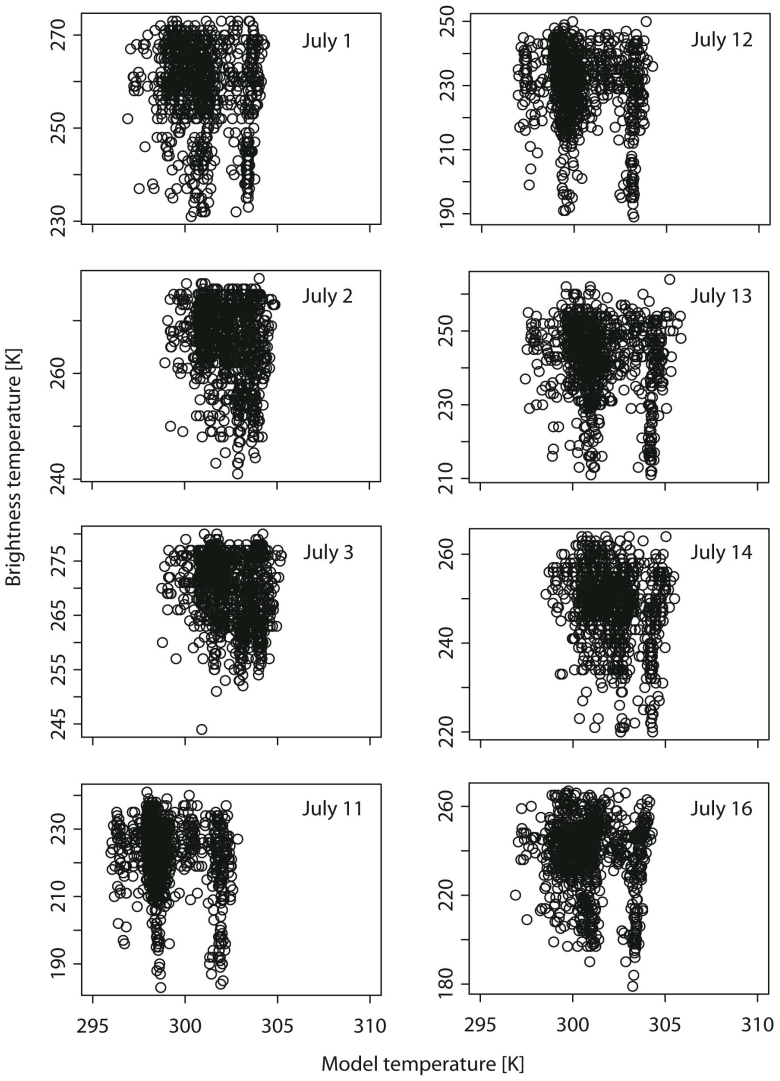

Figure 4.13: Simulated soil temperature [K] versus brightness temperature [K] for the whole watershed.

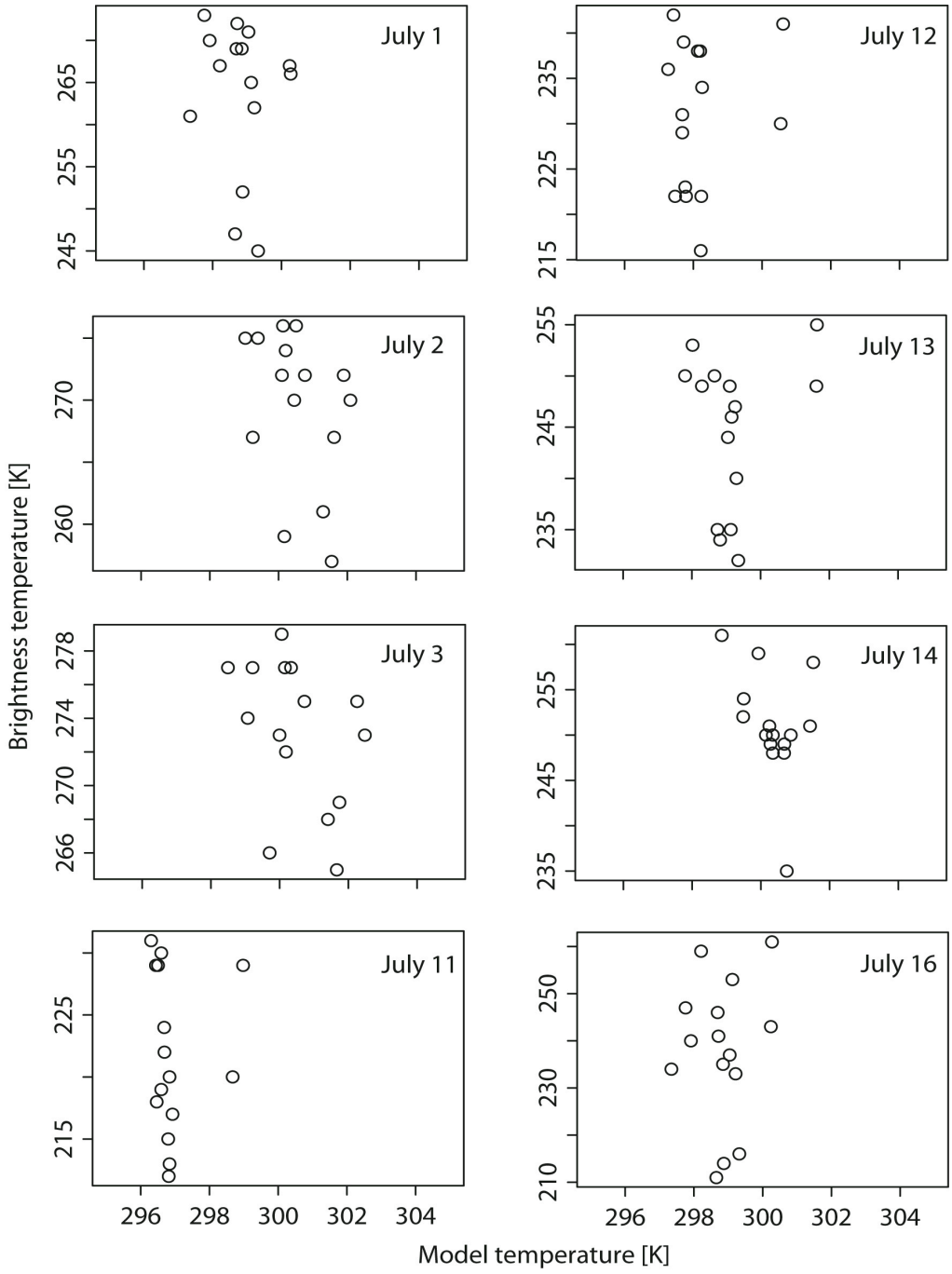

Figure 4.14: Simulated soil temperature [K] versus brightness temperature [K] in bare soil.

The low values of measured brightness temperatures compared to the simulated soil temperatures resulted in low values of emissivities (Figs. 4.15 and 4.16). Figure 4.15 shows the 5th, 50th, and 95th quantiles of the calculated emissivities, while the spatial emissivities for each day during the SGP97 experiment is shown in figure 4.16. The emissivities are calculated using equation 4.1. The calculated emissivities are lower than the values reported in the literature, for example see Dingman (1994). Even though, the emissivities in the dry period (July 1 - 4) are higher than in the wet period (July 11 - 16). This also supports our hypothesis stating that ESTAR soil moistures are influenced by surface runoff and interception.

From all above, we suspect that the brightness temperature and subsequently the algorithm used for deriving ESTAR soil moistures are not accurate, since the brightness temperature is highly dependent on the type of the model used for computing the brightness temperatures. For instance, Schmugge and Choudhury (1981) show that the brightness temperature varies significantly depending on the type of the model used for computing the brightness temperature, and on the wave frequency of the aircraft or satellite sensor used to measure the brightness temperature.

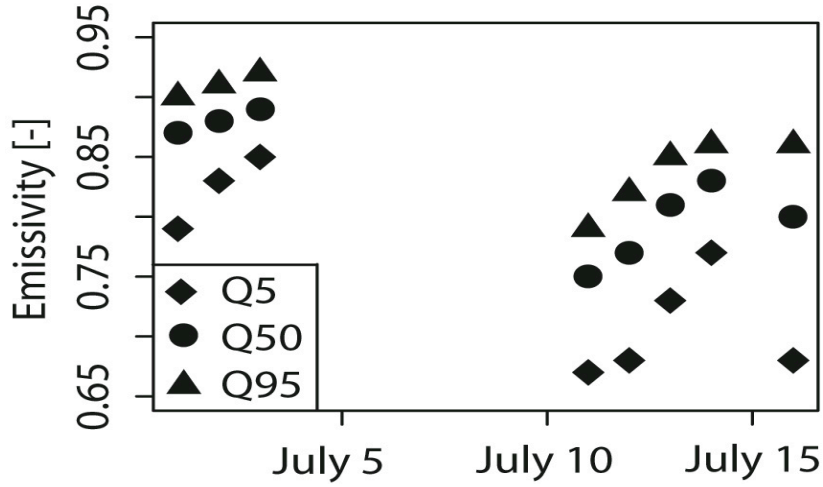

Figure 4.15: Soil emissivity for the 5th, 50th and 95th quantiles for the whole watershed, as derived from equation 4.1.

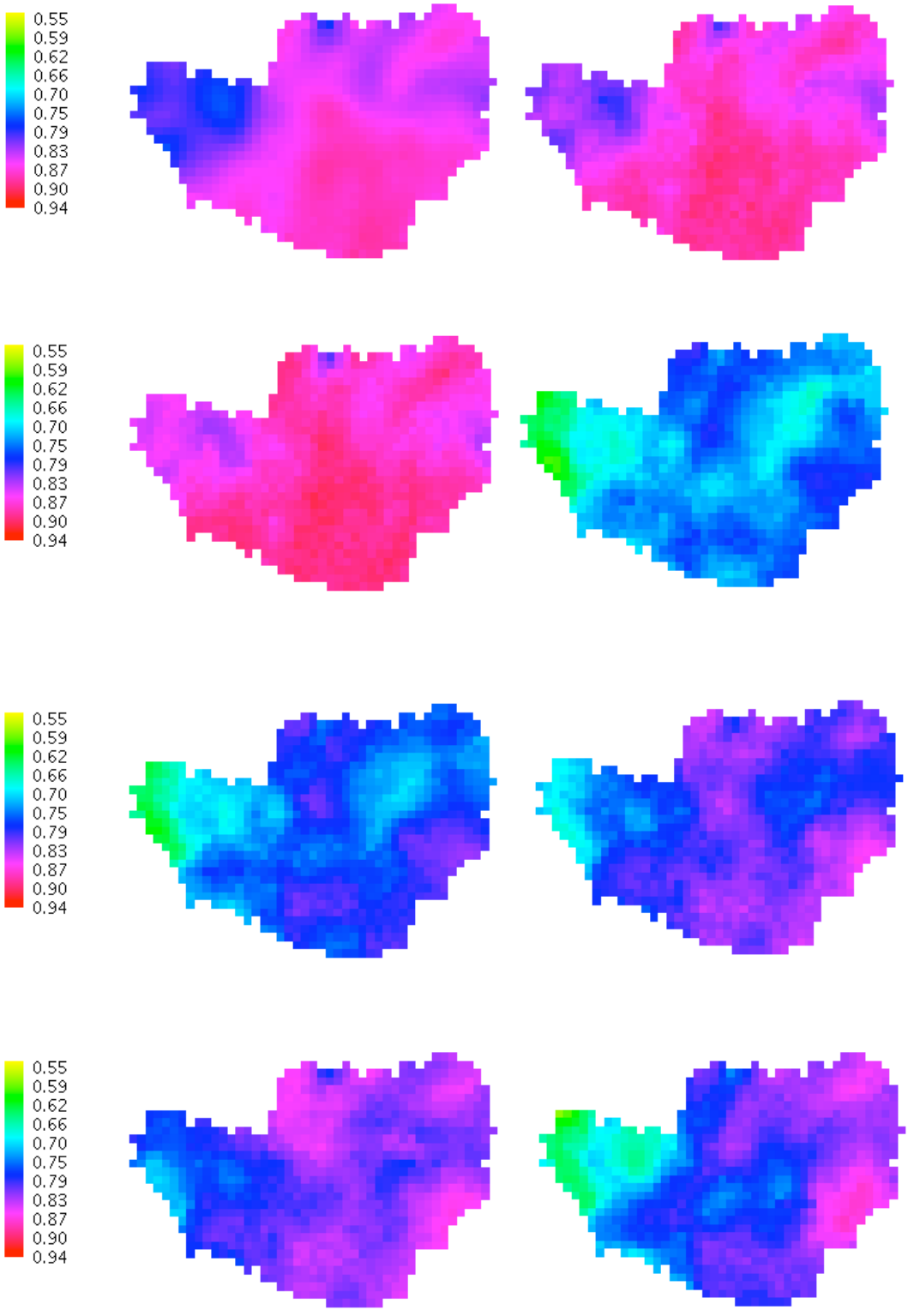

Figure 4.16: Spatial surface emissivity for July 1, 2, 3, 11, 12, 13, 14, and 16, from left to right, and from top to bottom, respectively.

4.2 Simulated and ESTAR soil moisture patterns during SGP99

4.2.1 Comparison between simulated and ESTAR soil moisture patterns

Figure 4.17 shows the spatial soil moisture patterns for ESTAR estimates and GEOtop simulations for July 8, 14, and 20, 1999, and for the top 5cm soil layer. The ESTAR soil moisture maps are downloaded from NASA website (Verified August 2009): (http://daac.gsfc.nasa.gov/fieldexp/SGP99/estar_sm.shtml). We observe that the simulated soil moisture patterns are different from the ESTAR soil moisture patterns. Again, the simulated soil moisture maps always look very similar to the watershed soil type map, confirming the previous result of the SGP97, which concludes that the soil type is the main controlling factor of the soil moisture distribution in the Little Washita watershed. While ESTAR spatial soil moisture patterns are very smoothed and are different from the watershed soil type map. For all the days of the comparison, ESTAR soil moisture maps are drier than the corresponding simulated soil moisture maps. GEOtop simulations show small number of small scattered portions with high soil moistures; effect of river network and concave pixels, while ESTAR estimates do not show any pixels with high soil moistures.

Comparing soil moistures for ESTAR estimates and GEOtop simulations during the SGP99, ESTAR estimates show very low soil moistures range compared to the GEOtop simulations, and this most likely ESTAR underestimates the soil moistures. It is evident that ESTAR estimates do not consider the effect of the river network and concave zones at which the soil is saturated or have high soil moisture levels.

Comparing the spatial soil moistures during the SGP97 with the spatial soil moistures during the SGP99, both ESTAR estimates and GEOtop simulations show that spatial soil moistures during the SGP99 are much drier than that during the SGP97. A noticeable difference in soil moistures between SGP97 and SGP99 is that, generally, during the SGP97, ESTAR overestimates soil moistures with respect to the GEOtop simulations, while during the SGP99, ESTAR underestimates soil moistures with respect to the GEOtop simulations. Another noticeable difference is that during the SGP97 always there are some locations with zero soil moistures for ESTAR estimates. As there are many locations with zero soil moistures during the SGP97, and as the soil is much drier during the SGP99, more locations with zero soil moistures for ESTAR estimates are expected during the SGP99; however, that is not the case. This shows

inconsistency in ESTAR estimates, and suggests that ESTAR during the SGP97 and the SGP99 are computed slightly in different ways.

The mean differences in spatial soil water content between ESTAR estimates and GEOtop simulation shown in figure 4.17, are computed quantitatively in terms of RMSE and bias, and are shown in figure 4.18. The differences decrease on July 14 and 15, following the rainfall event on July 10, and then increase again as soil dries. The RMSE and bias are relatively low; simulated and ESTAR soil moisture maps are somehow comparable, especially on July 14 and 15. Although both RMSE and bias are small, ESTAR soil moisture patterns are different from the simulated patterns. This means having low values of RMSE and bias do not necessarily having the actual soil moisture patterns.

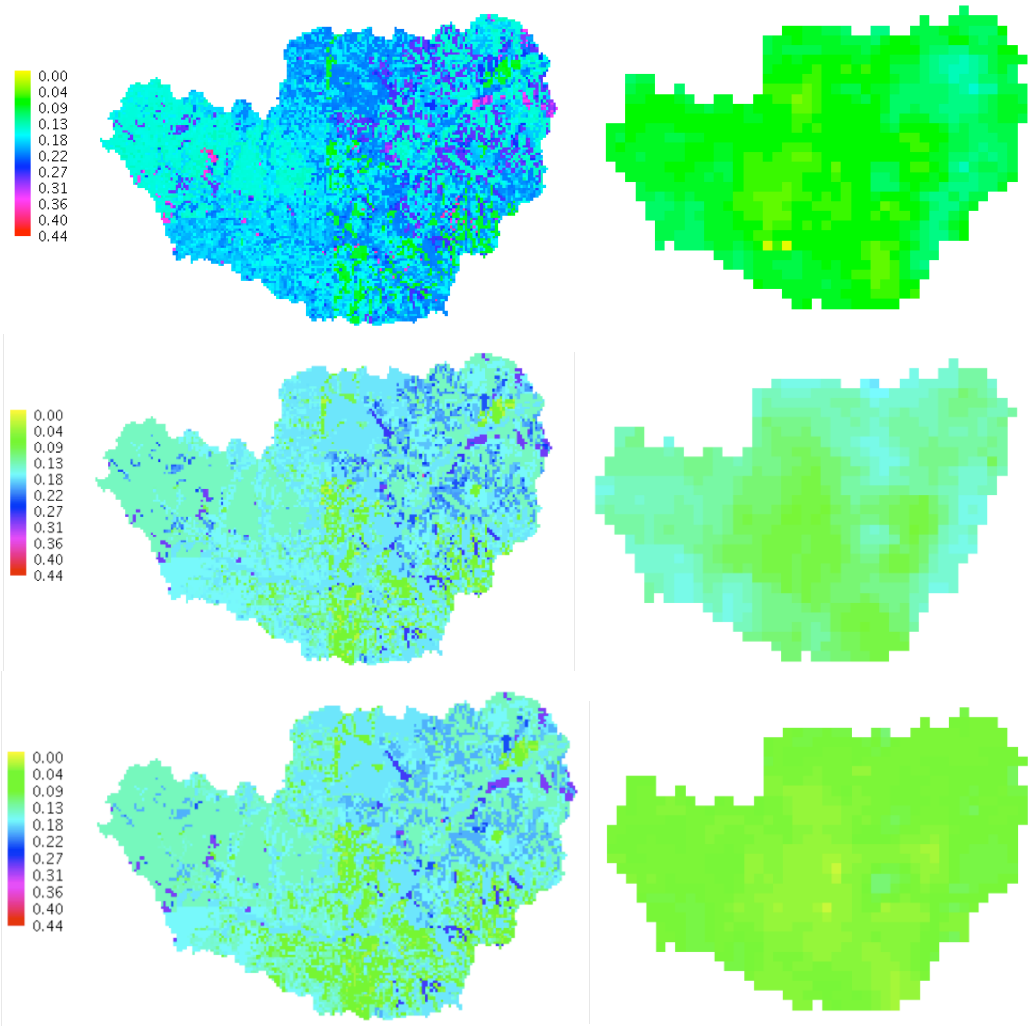

Figure 4.17: Volumetric water content of the top 5cm soil for July 8, 14, and 20, 1999, from left to right and from top to bottom, respectively. Each row (couple) refers to a different day. (right) estimated using ESTAR [800m resolution]. (left) simulated using GEOtop model [200m resolution].

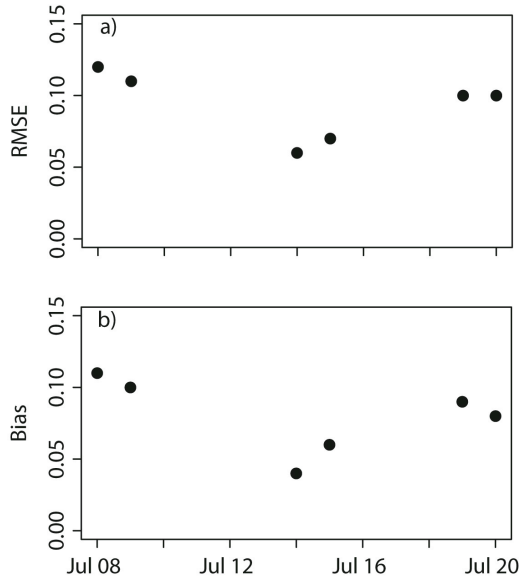

Figure 4.18: a) Root mean square error of water content [-] between ESTAR estimates and simulated soil moisture, and b) Bias between ESTAR estimates and simulated soil moisture for the whole watershed.

4.2.2 The relationships vegetation, surface roughness, topography, and ESTAR soil moisture

The effect of vegetation on ESTAR soil moistures is investigated by comparing the mean soil moisture content for only bare soil in a fixed soil type, with the mean soil moisture content for all the landuse classes in the same soil type. The effect of surface roughness on ESTAR soil moistures is investigated by comparing the mean soil moisture content for only channel network pixels in a fixed soil type, with the mean of soil moisture content for only non-channel network pixels in the same soil type. While the effect of topography on ESTAR soil moistures is investigated by comparing the mean soil moisture content for only concave pixels in a fixed soil type, with the mean soil moisture content for only convex pixels in the same soil type.

In this chapter, we investigated the effect of vegetation, surface roughness, and topography on ESTAR soil moistures for silt loam (soil type 8 - hydraulic conductivity = 0.63 - 2.00 mm/s), and sandy loam (soil type 13 - hydraulic conductivity = 2.00- 6.30 mm/s), as shown in figures 4.19 and 4.20, respectively.

Results show that for both soil types there are insignificant effects of vegetation on ESTAR soil moistures; mean soil moisture content for only bare soil in a fixed soil type is similar to the mean soil moisture content of all landuse classes in the same soil type. Similarly, for both soil types, there are insignificant effects of surface roughness on ESTAR soil moistures; mean soil moisture content for only channel network pixels in a fixed soil type is similar to the mean soil moisture content for the only non-channel network pixels in the same soil type. Finally, for both soil types, there are insignificant effects of topography on ESTAR soil moistures; the mean soil moisture content for only concave pixels in a fixed soil type similar to the mean soil moisture content for the only convex pixels in the same soil type. These results confirm the previous results that were obtained during the SGP97; there are insignificant effects of vegetation except of interception, surface roughness, and topography on ESTAR soil moistures.

From figures 4.19 and 4.20, it is evident that ESTAR underestimates soil moistures with respect to the simulated soil moistures, and the differences between the ESTAR estimates and the GEOtop simulations decrease for July 14 and 15, 1999, following the rainfall event on July 10, and as soil dries, the differences increase again. At a certain wetness conditions in the watershed, the differences between the ESTAR estimates and GEOtop simulations are minimal. In spite of that, ESTAR estimates and GEOtop simulations are comparable to a large extent.

Crosson et al. (2005) studied parameter sensitivity of soil moisture retrievals from airborne L-Band radiometer measurements (ESTAR) during the SMEX02 experiment, and they reported that the uncertainties in ESTAR soil moisture estimates are related to surface roughness and absorption, scattering, and emission by vegetation. In addition to that, Crosson et al. (2005) and Ulaby et al. (1983) reported that microwave brightness temperature is strongly depends on temperature depth profile of the soil.

Crosson et al. (2005) showed that volumetric soil moisture content increases monotonically with the increase of surface roughness, and that the volumetric soil moisture versus surface roughness relationship is very sensitive for wet soils than for dry soils. They showed that this relationship depends on polarization approach to a large extent. Moreover, they observed that the effects of surface roughness and vegetation on brightness temperature are higher for wet soils than for dry soils.

On the other hand, Drusch et al. (2001) studied the dependency of surface emissivity on atmospheric and vegetation effects, and they reported that the variability in integrated atmospheric water vapour introduces variations of about 0.023 in surface emissivity.

This value is ~36% of the variability caused by changes in soil moisture. They concluded that atmospheric corrections should generally improve the soil moisture retrieval from passive microwave remote sensing.

So, at least in this case (SGP99), where there are insignificant effects of vegetation, surface roughness, and topography on ESTAR soil moistures, the differences between GEOtop simulations and ESTAR estimates is more likely due to the effects of temperature depth profile of the soil, atmospheric effects, and other errors (such as errors in the algorithm used for inverting brightness temperatures to volumetric soil moistures) that are not accounted for.

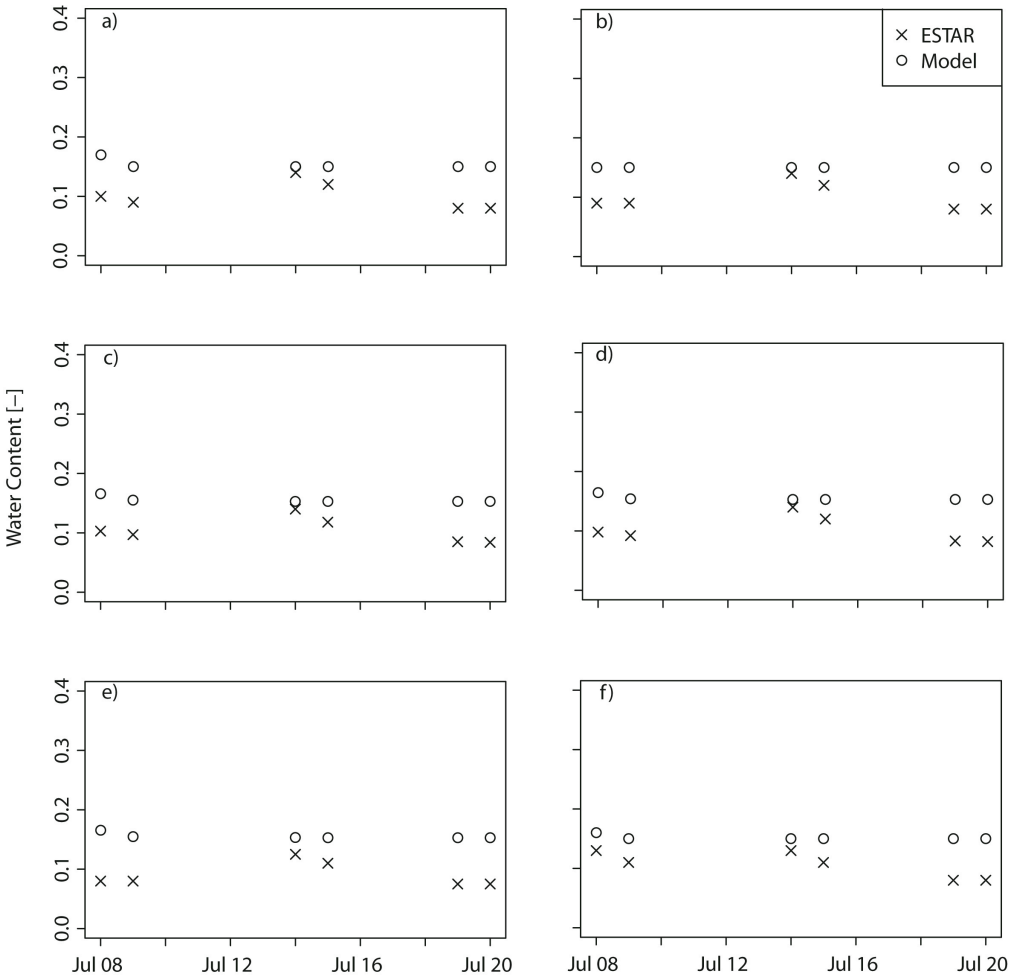

Figure 4.19: Simulated and ESTAR soil moisture time series for the top 5cm soil layer for: a) Soil moisture content for all pixels of silt loam soil, b) Soil moisture content for silt loam soil in only bare soil, c) Soil moisture content for silt loam soil in only concave pixels, d) Soil moisture content for silt loam soil in only convex pixels, e) Soil moisture content of silt loam soil in only non-channel network pixels, and f) Soil moisture content for silt loam soil in only channel network pixels.

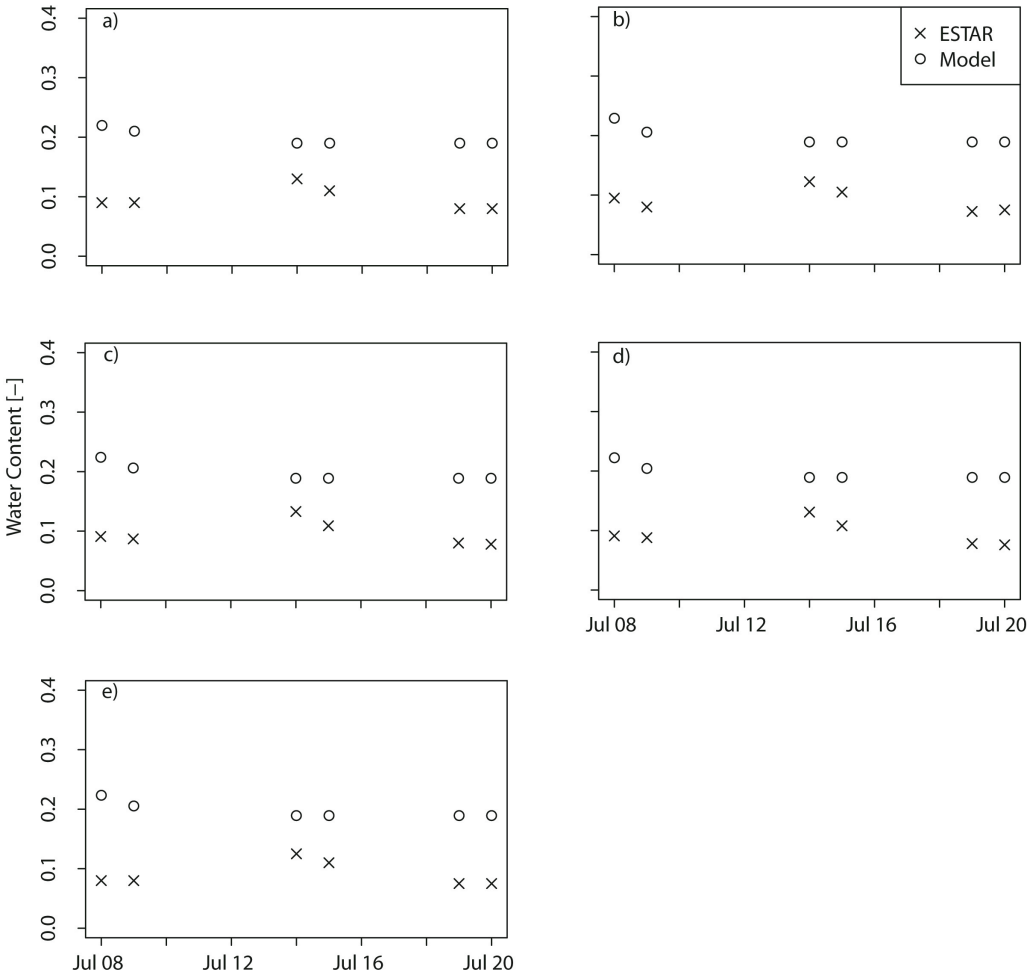

Figure 4.20: Simulated and ESTAR soil moisture series for the top 5 cm soil layer for: a) Soil moisture content for all pixels of sandy loam soil, b) Soil moisture content for sandy loam soil in only bare soil, c) Soil moisture content for sandy loam soil in only concave pixels, d) Soil moisture content for sandy loam soil in only convex pixels, and e) Soil moisture content of sandy loam soil in only non-channel network pixels. There are no pixels of ESTAR estimates for only channel network.

4.3 Conclusion

Simulated and ESTAR soil moisture patterns obtained during the SGP97 and SGP99 in the Little Washita watershed (583 km^2), Oklahoma, USA, are studied. Results show that ESTAR estimates and simulated soil moistures are comparable when the watershed is

relatively dry, but they are very different when the watershed is wet. The RMSEs and biases for the relationships between the simulated and ESTAR soil moistures are very small during dry periods. We find that obtaining small value of RMS it doesn't mean necessarily obtaining the actual soil moisture patterns. Modeling results show that soil texture controls the spatial soil moisture distribution in the watershed. This is consistent with the findings of Cosh and Brutsaert (1999) who concluded that soil texture is the main factor controlling the spatial distribution of soil moisture in the Little Washita watershed. In addition, we investigated the effect of vegetation, surface roughness, and topography on ESTAR soil moistures, and it found that vegetation except intercepted water, surface roughness, and topography have little effects on ESTAR soil moistures (Bushara et al. 2010). Possible explanation for the discrepancy between simulated and ESTAR soil moistures is that ESTAR is highly influenced by surface runoff, and by vegetation-intercepted water to some extent. Furthermore, we used simulated soil moistures and soil temperatures to produce bias-adjusted ESTAR soil moisture maps. However, we are not able to produce such maps because there is no well-defined relationship between the GEOtop simulated soil moisture and the ESTAR measured brightness temperature or between the GEOtop simulated soil temperature and the brightness temperature as given by ESTAR. The calculated emissivities, based on simulated soil temperature and measured brightness temperature, are much lower than the values reported in the literature. Therefore, we conclude that there is a problem with the algorithm that is used for inverting the brightness temperatures to volumetric soil moistures.

5 Characterization of space-time soil moisture variability during SGPs

This chapter focuses on characterization of space-time soil moisture variability from two sources of data: ESTAR passive microwave radiometer and GEOtop simulations, and using SGP97 and SGP99 datasets. This study is important because to our knowledge no study has done comparative study of soil moisture variability from aircraft-based microwave observation and distributed model simulations. Do both methods perform similarly? Or which one performs better?. First, we compared distributions, followed by moments, then scaling, and finally spatial statistics, including covariances. The relationships between the STDEV, CV, skewness and kurtosis versus spatial mean soil moisture are identified. Further, the scaling characteristics of soil moisture are studied. The last section is dedicated to the re-thinking of the soil moisture assessment in SGP experiments.

5.1 Statistical characterization of soil moisture

5.1.1 Soil moisture frequency distributions

Figures 5.1 and 5.2 present the frequency distribution of soil moisture, during the SGP97 and SGP99, respectively, derived from ESTAR estimates and GEOtop simulations, over the sandy loam and silt loam parts of the watershed.

During the SGP97 (Fig. 5.1), ESTAR estimates cover a larger range of soil moisture values than GEOtop simulations. ESTAR estimates have unimodal, bell-shaped distributions that can be approximated by normal distribution. On the contrary, GEOtop simulations show negative skewness at high wetness levels and as soil dries, the distributions change to positive skewness. The evolution of soil moisture from negative skewness to positive skewness suggests that the soil moisture distribution could be well represented by beta distribution. As soil dries, GEOtop simulations show that silt loam

soil has bimodal distribution, while sandy loam dries gradually and have a negative skewness. The gradual drying of soil moistures of the sandy loam soil and the bimodality distribution of the silt loam soil indicate the effect of the river network on the spatial distribution of soil moisture. This is due to the fact that sandy loam soil lies along the river network, while the silt loam soil lies in the northeast (along the river network; relatively high soil moistures) and in the northwest (upper part of the watershed; relatively low soil moistures) (see Fig. 4.4). This effect of the river network on the soil moisture distribution is not reported by ESTAR estimates. On July 11 and for the sandy loam soil, GEOtop simulations show that most of pixels have the same high soil moisture level. This is because the sandy loam soil lies along the river network (see Fig. 4.4) and the watershed was saturated.

During the SGP99 (Fig. 5.2) ESTAR underestimates soil moistures with respect to the GEOtop simulations. For both soil types, ESTAR estimates show that soil moistures can be approximated by normal distribution, while GEOtop simulations show that soil moistures are positively skewed; most of pixels have low and the same soil moisture values with few pixels with varying soil moisture levels (soil moisture varies from minimum soil moisture to the saturation). Except for July 8 and 9, and for both soil types, GEOtop simulations show that most of pixels have the same low soil moisture level. Since the watershed is dry during the SGP99, this behaviour of GEOtop, i.e., most of pixels have the same low soil moisture level, is not attributed to the saturation conditions in the watershed. This is likely that the watershed is at wilting point. For both soil types, the low soil moisture levels shown by GEOtop simulations are not the residual water contents of the soils since in the GEOtop simulations the residual water contents of the top 5cm soil layer are taken to be 0.03 and 0.09 for sandy loam and silt loam, respectively.

As discussed earlier, and for both soil types, there are some pixels lay on the river network with high levels of soil moistures. Further, as there is streamflow at the watershed outlet, there should be some pixels at saturation. GEOtop simulations show that there are some pixels at saturation, while ESTAR estimates do not show any pixels

at saturation. This indicates that GEOtop simulations are more accurate than ESTAR estimates.

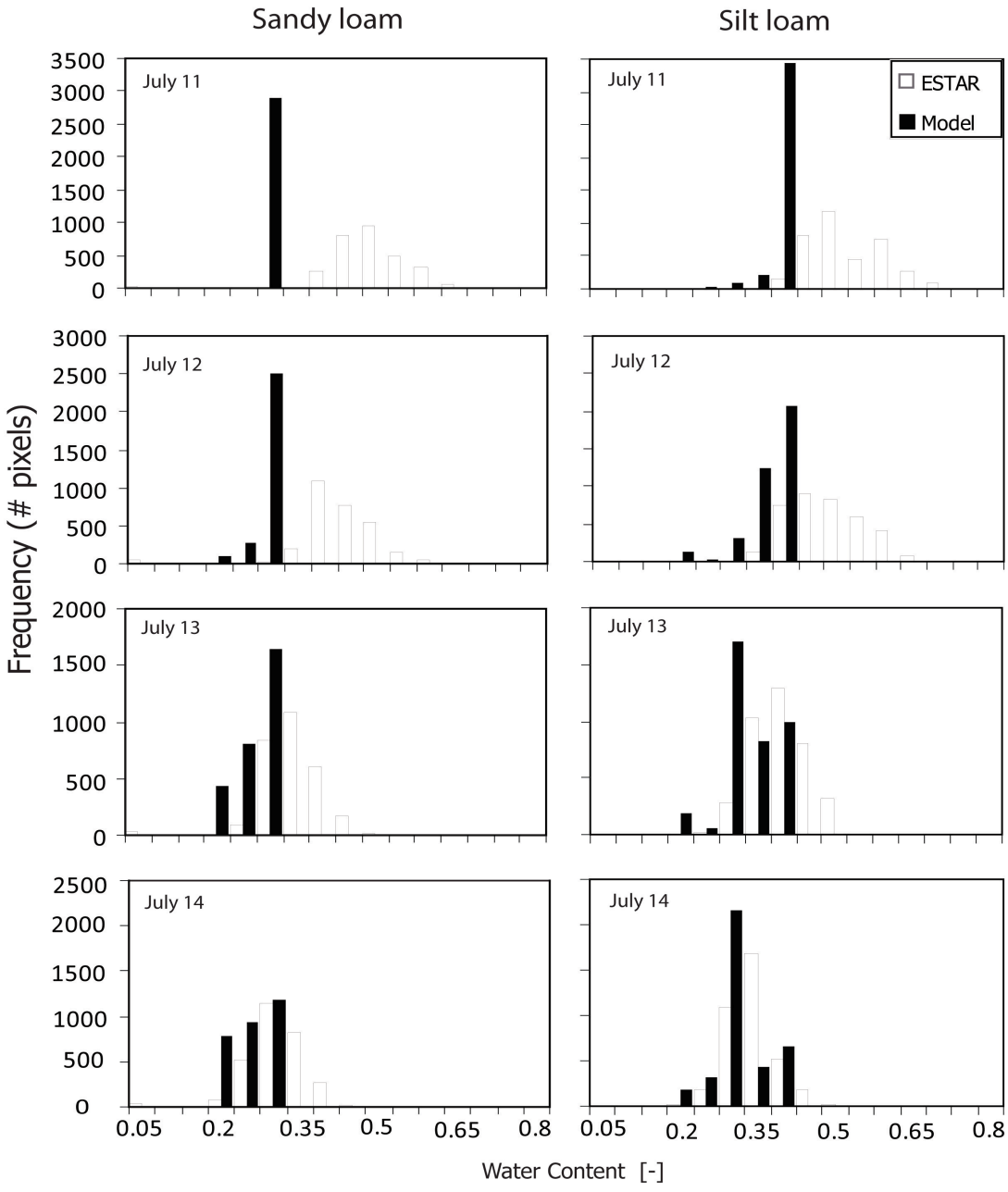

Figure 5.1: Simulated and ESTAR soil moisture frequency distributions for the top 5cm soil layer for both sandy loam and silt loam soils. Sandy loam (left) and silt loam (right) for July 11, 12, 13, and 14, 1997. On July 11 and for the sandy loam soil, model simulations show that most of pixels have the same high soil moisture level. This is because the sandy loam soil lies along the river network (see Fig. 4.4) and the watershed was saturated.

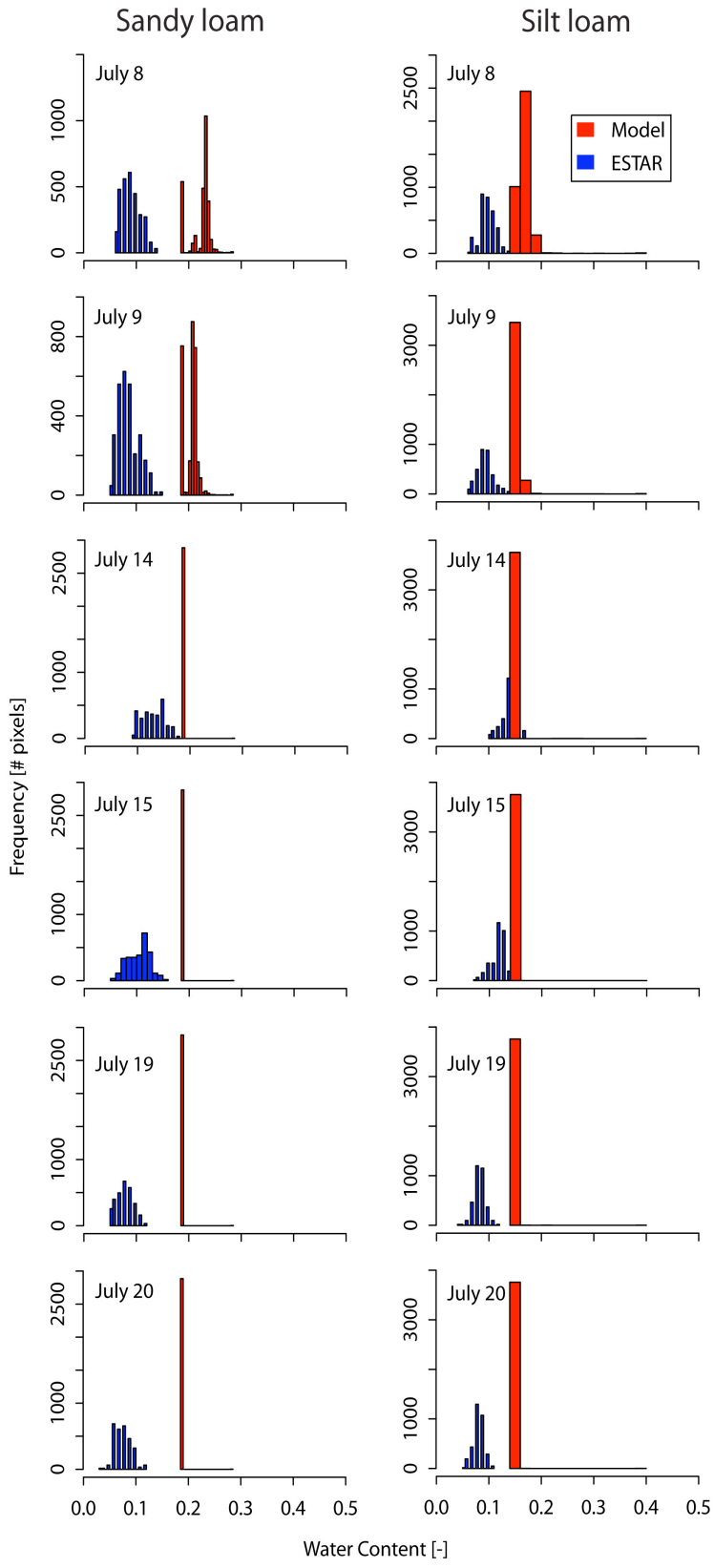

Figure 5.2: Simulated and ESTAR soil moisture frequency distributions for the top 5cm soil layer for both sandy loam and silt loam soils. Sandy loam (left), and silt loam (right) for July 8, 9, 14, 15, 19, and 20, 1999.

5.1.2 Standard deviation, coefficient of variation, and skewness

In this section, we characterize soil moisture variability for the two main soil textures in the watershed: sandy loam (soil type 13 - hydraulic conductivity = 2.00 - 6.30 mm/s) and silt loam (soil type 8 - hydraulic conductivity = 0.63 - 2.00 mm/s), which represent 19.8% and 25% of the watershed coverage, respectively. As shown in figure 4.4, sandy loam lies along the main river and in the central north part of the watershed, while silt loam lies in the northeast and northwest parts.

Figures 5.3 and 5.4 present the spatial STDEV, CV and skewness of near-surface soil moisture as a function of the spatial mean, during the SGP97 and SGP99, respectively, derived from ESTAR estimates and GEOtop simulations for both soil types.

During the SGP97 (Fig. 5.3) ESTAR estimates show linear relationship between STDEV and mean, with STDEV increasing with increasing mean wetness, for both soil types. On the contrary, GEOtop simulations show a downward quadratic relationship between the STDEV and mean, where the STDEV is low at low and high ends of mean wetness and takes maximum values at moderate mean wetness levels, for both soil types. We fit the relationship between the standard deviation and spatial mean of soil moisture with second order polynomial, while Pan and Peters-Lidard (2010) fit this relationship with third order polynomial. In both approaches (our approach and Pan and Peters-Lidard approach) the relationship between the standard deviation and the spatial mean is assumed to have downward relationship. Pan and Peters-Lidard assume that the maximum point of the curve is at the field capacity, and the low ends of the curve are for the saturation and wilting point of the soil. Their main assumption to derive the relationship between the standard deviation and the spatial mean is that most of observed soil moistures are between the states of saturation and wilting point. In our approach we find that at saturation condition the standard deviation is equal zero. Likewise, we find that for dry conditions, when all plants at wilting point, the standard deviation is also equal zero. Similar to the Pan and Peters-Lidard approach we also assume that the maximum point of the curve is at the field capacity. Knowing the boundary conditions at the two low ends and the maxima of the curve allow us to fit the relationship between the standard deviation and the spatial mean with second order polynomial.

ESTAR estimates also show a linear relationship between the spatial CV and spatial mean, with CV decreasing with increasing wetness, for both soil types. On the contrary, GEOtop simulations show downward quadratic relationship between CV and mean, for both soil types. ESTAR estimates show zero skewness for the spatial frequency distribution of near-surface soil moisture regardless of the mean wetness level, while GEOtop simulations show positive skewness for dry soils, zero skewness for moderate wet soils, and negative skewness for very wet soils, for both soil types.

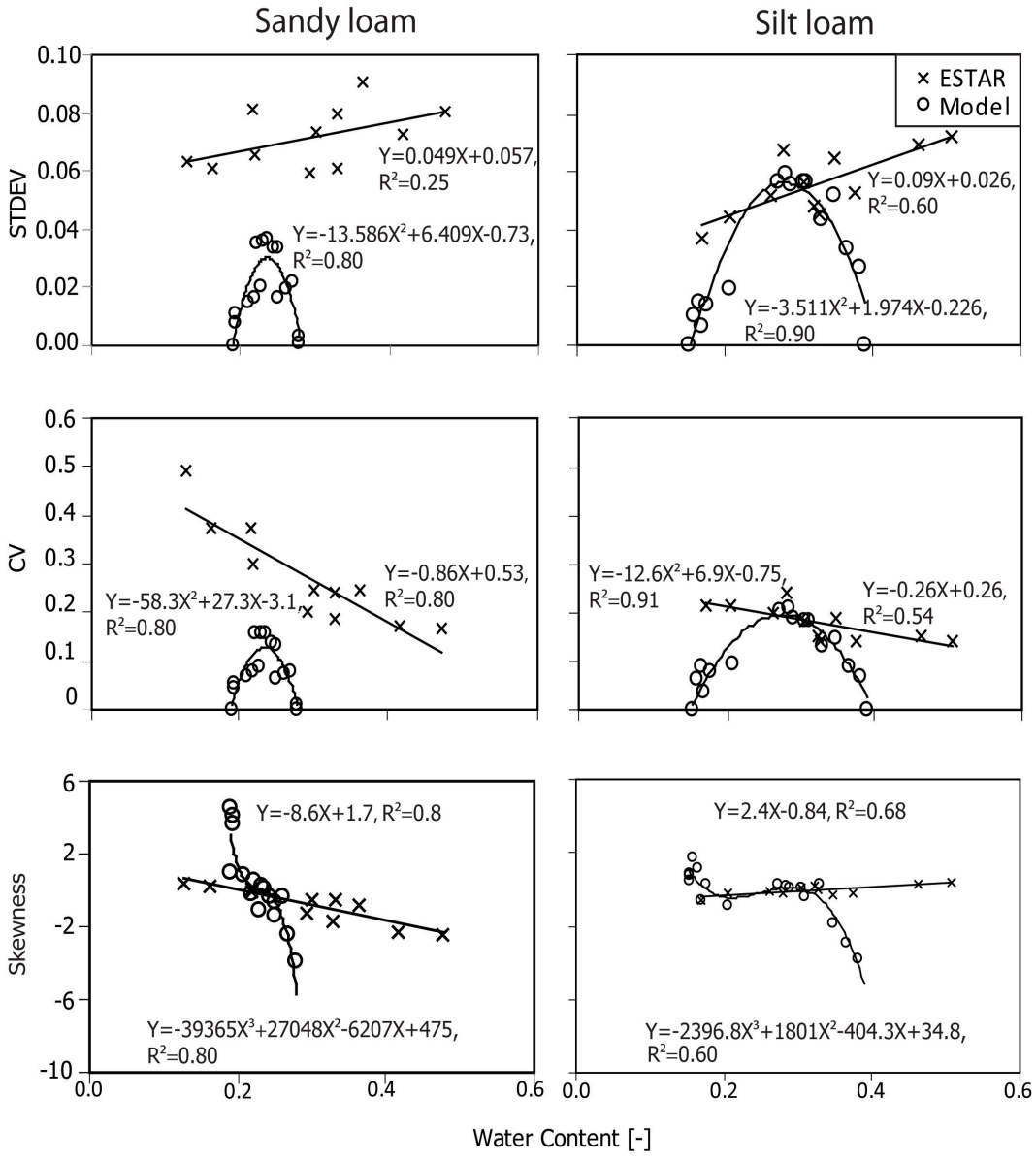

Figure 5.3: STDEV, CV, and skewness versus mean soil moisture for the top 5cm soil layer during the SGP97, for sandy loam soil (left) and silt loam soil (right).

The relationships between the spatial STDEV, CV and skewness of near-surface soil moisture as a function of the spatial mean during the SGP99 (Fig. 5.4) are very similar to the same relationships obtained during the SGP97. Because the watershed is dry, i.e. short range of soil moisture dynamics during the SGP99, the STDEV and CV versus the spatial mean of soil moisture derived from GEOtop simulations did not show downward quadratic relationships, but they tend to show downward quadratic relationships. Furthermore, because the watershed is dry, the soil moistures derived from GEOtop simulations have positive skewness.

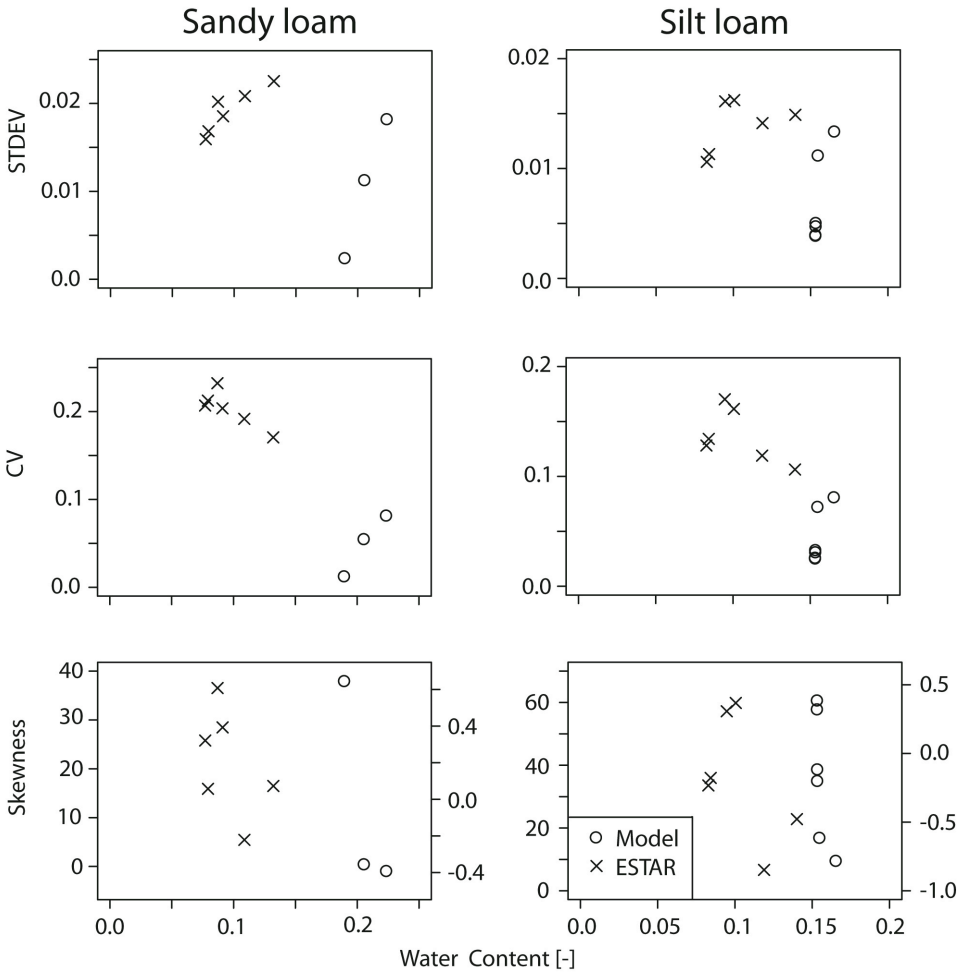

Figure 5.4: STDEV, CV, and skewness versus mean soil moisture for the top 5cm soil layer during the SGP99, for sandy loam soil (left) and silt loam soil (right). The skewness in the main ordinate is for the soil moisture derived from GEOtop simulations, while the skewness in the secondary ordinate is for the soil moisture derived from ESTAR estimates.

5.1.3 Kurtosis of soil moisture

As known, kurtosis describes the flatness or peakedness of a distribution relative to the normal distribution. Kurtosis equals 3 for normal distribution. Kurtosis is greater than 3 for distributions that are steeper than the normal distribution. It is smaller than 3 for flatter distributions.

Figures 5.5 and 5.6 present kurtosis of near-surface soil moisture as a function of the spatial mean, during the SGP97 and SGP99, respectively, derived from ESTAR estimates and GEOtop simulations, for both soil types.

During the SGP97 (Fig. 5.5), and for both soil types, ESTAR estimates show that soil moisture distribution can be well approximated by normal distribution (kurtosis around 3, although for silt loam soil the distribution is slightly flatter than the normal distribution), while GEOtop simulations show that only midrange soil moistures can be approximated by normal distribution. GEOtop simulations show that low soil moistures have distributions flatter than the normal distribution (kurtosis less than 3), and high soil moistures have distributions steeper than the normal distribution (kurtosis greater than 3), for both soil types.

During the SGP99 (Fig. 5.6), and for both soils, ESTAR estimates show that soil moistures have distributions flatter than the normal distribution, while GEOtop simulations show that soil moistures have distributions steeper than the normal distribution. Because the watershed was dry during the SGP99, GEOtop simulations show that soil moistures have distributions steeper than the normal distribution. On the contrary, during the SGP97, GEOtop simulations show that dry soils have distributions flatter than the normal distribution. This contradiction in soil moisture distribution for dry soils is most likely due to the differences in soil moisture dynamics mechanisms. During the SGP99, majority of pixels in the watershed have low soil moistures, while during the SGP97, the soil dries gradually after the saturation following the heavy rainfall event on July 10, 1997. We have to mention that during the SGP97, there was heavy rainfall event on July 10, and light rainfall events on July 4 and 15, while during the SGP99, there was light rainfall event on July 10,1999.

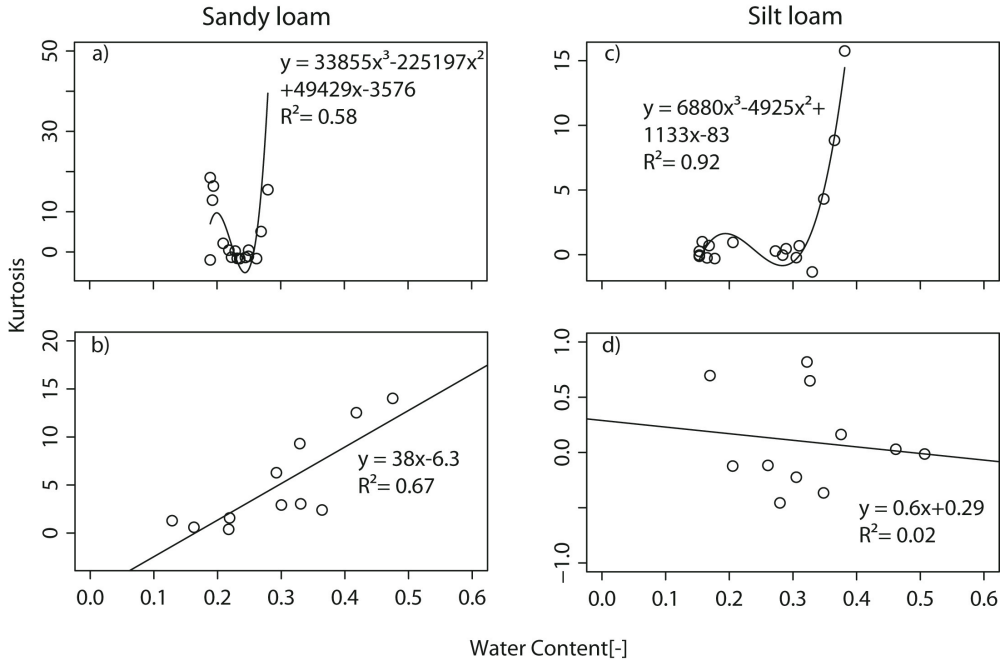

Figure 5.5: Kurtosis versus mean soil moisture for the top 5cm soil layer during the SGP97, for the sandy loam (left) and silt loam (right). a) and c) for simulated soil moistures, while b) and d) are for ESTAR estimates.

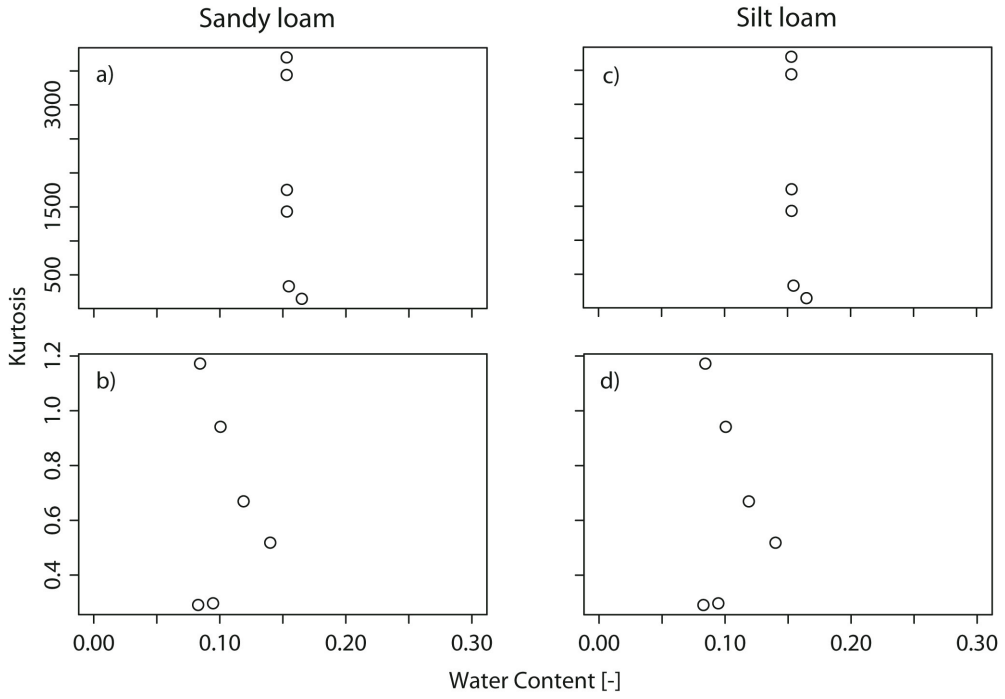

Figure 5.6: Kurtosis versus mean soil moisture for the top 5cm soil layer during the SGP99, for the sandy loam (left) and silt loam (right). a) and c) for simulated soil moistures, while b) and d) are for ESTAR estimates.

5.2 Scaling analysis of simulated and ESTAR soil moistures

We used random filed theory described in Vanmarcke (1983) to model the complex patterns of soil moisture. The soil moisture is assumed to be a random process in space and time. This theory is feasible for the cases where deterministic treatment is insufficient and conventional statistics in sufficient (Vanmarcke 1983). An ideal random field model has to capture the essential feature of the complex random phenomena in terms of a minimum number of physically meaningful and experimentally accessible parameters (Vanmarcke 1983). The scale at which the random process is observed is very important. A phenomenon that appears deterministic on the microscale -have defined structured atoms- may at large-scale exhibit highly variable properties that call for the probabilistic description. In this study, we used the coarse graining method (Vanmarcke 1983) that uses minimum number of physically meaningful parameters to describe the spatial process of soil moisture. For the full explanation of the coarse graining method, please see Vanmarcke (1983).

Figures 5.7 and 5.9 show the log soil moisture variance versus log area during the SGP97 and SGP99, respectively, for both ESTAR estimates and GEOtop simulations and for the top 5cm soil layer along the main transect (Fig. 5.10). While figures 5.11 and 5.12 show the log correlation of soil moisture versus log distance during the SGP97 and SGP99, respectively, and for the top 5cm soil layer along the same transect. The soil moisture sampling transect crosses varying elevations, landuses, and soil textures (Figs. 5.10 and 1.2).

The soil moisture was aggregated at increasing spatial scales, from a pixel of 200m side to a pixel of 2600m side for the simulated soil moistures, and from a pixel of 800m side to a pixel of 9600m side for ESTAR soil moistures. At each aggregation level, the soil moisture was taken to be the average soil moistures of the 200m and 800m pixels for the GEOtop simulations and ESTAR estimates, respectively, and no overlapping was considered in the aggregation. The model spatial scale is limited to 2600m in order to have more sampling points in the analyses. During the SGP97 the watershed was relatively wet, while during the SGP99, the watershed was dry.

For the wet conditions; SGP97, results show that the log soil moisture variance versus the log area has an increasing power law relationship, for both simulated and ESTAR soil moistures with statistically significant correlations. This suggests that the spatial soil moisture variance have the property of scale-invariance. This result is in agreement

with Gebremichael et al. (2009) who found that the soil moistures have the property of scale-invariance in the variograms of spatial soil moistures. For the dry conditions; SGP99, the soil moisture variance is spatially uniform and is independent of scale.
The slope time series of the power law relationship of figure 5.7 for the GEOtop simulations and ESTAR estimates are shown in figure 5.8. During the dry-down period (July 11-14) the slopes of both ESTAR and model, in general, decrease with the time. This indicates that the drying process produces large degree of heterogeneity at large scale. This is in disagreement with Rodriguez-Iturbe et al. (1995) who found that the drying process produces large degree of heterogeneity at small scale. This disagreement is likely due to the effect of initial conditions of soil moisture and to different mechanisms of soil moisture dynamics.

The log correlation of soil moisture versus log separation distance (Figs. 5.11 and 5.12) for both simulated and ESTAR soil moistures show that soil moisture has multiscaling behaviour. The average correlation range of near-surface soil moisture is estimated to be around 7km. In agreement with Rodriguez-Iturbe et al. (1995), GEOtop simulations show that the spatial correlation of the near-surface soil moisture follows power law decay up to about 1km. For scales larger than 1km, both GEOtop simulations and ESTAR estimates show that soil moisture has multiscaling behaviour (Bushara and Rigon, 2010). The multiscaling behaviour of soil moisture is due to the high heterogeneities of soil moistures along the transect, since the transect crosses varying elevations, landuses, and soil textures. The decay of spatial correlation of soil moisture with the increase of distance is also observed by Khandani and Kalantari (2009) who analyzed soil moisture data in the Little Washita watershed during the SMEX03, and they found that the soil moisture correlation is exponentially decaying with the increase of distance, with zero correlation for distances beyond 0.4km.

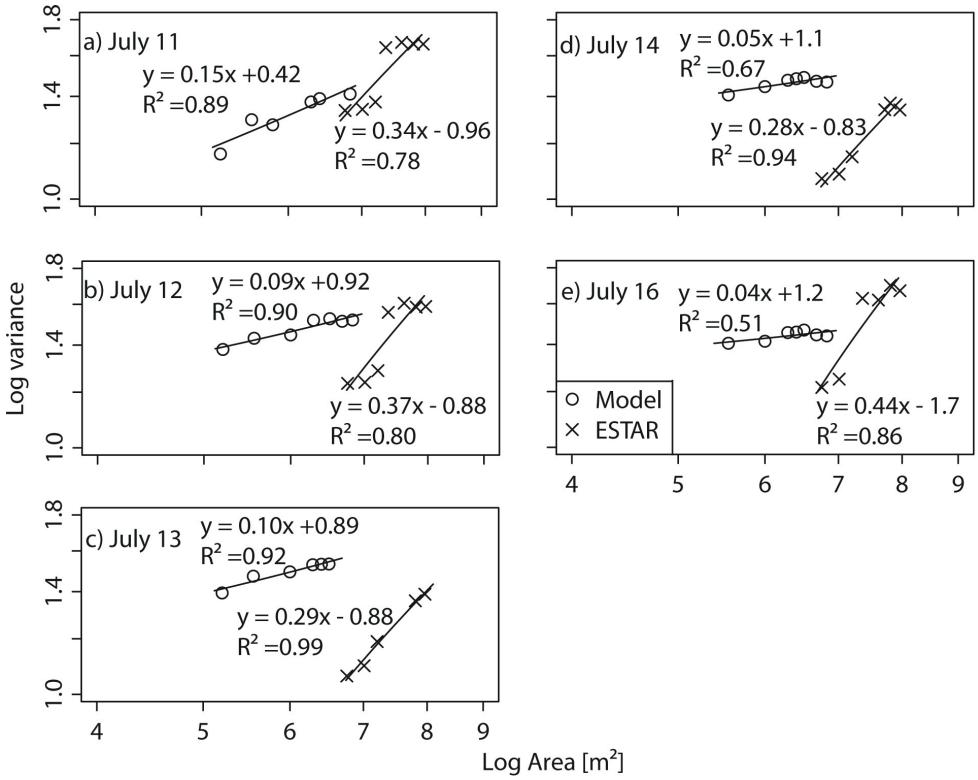

Figure 5.7: Log soil moisture variance versus log area for GEOtop simulations and ESTAR estimates along the transect (Fig. 5.10) for the top 5cm soil layer for: a) July 11, b) July 12, c) July 13, d) July 14, and e) July 16, 1997.

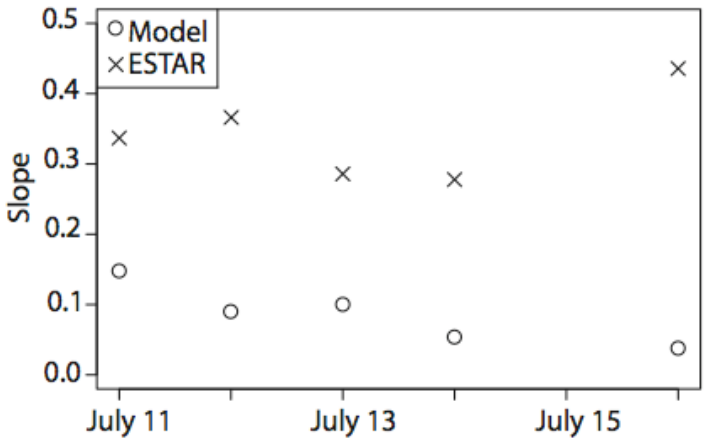

Figure 5.8: Slopes of the fitting lines in figure 5.7.

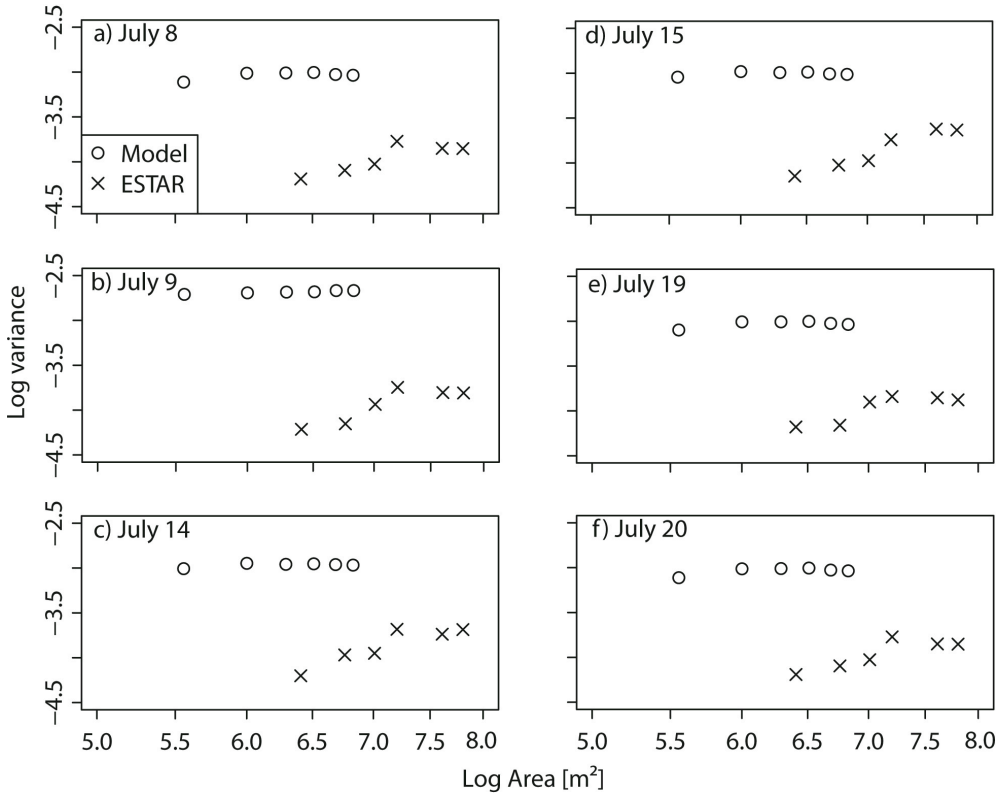

Figure 5.9: Log soil moisture variance versus log area for GEOtop simulations and ESTAR estimates along the transect (Fig. 5.10) for the top 5cm soil layer for: a) July 8, b) July 9, c) July 14, d) July 15, e) July 19, and f) July 20, 1999.

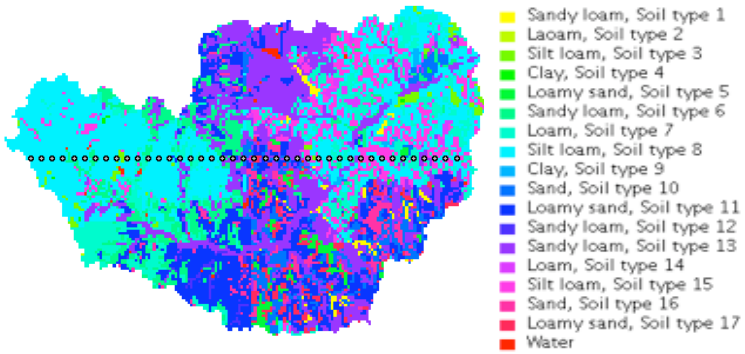

Figure 5.10: Soil texture map of the Little Washita watershed showing the transect of soil moisture scaling.

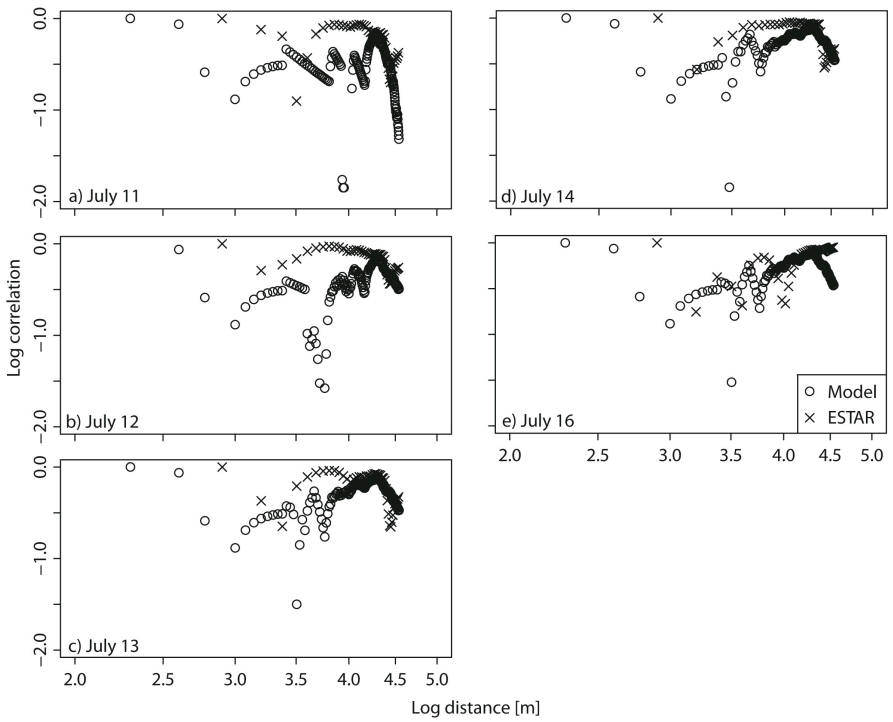

Figure 5.11: Spatial correlation of soil moisture along the transect (Fig. 5.10) for the top 5cm soil layer for: a) July 11, b) July 12, c) July 13, d) July 14, and e) July 16, 1997.

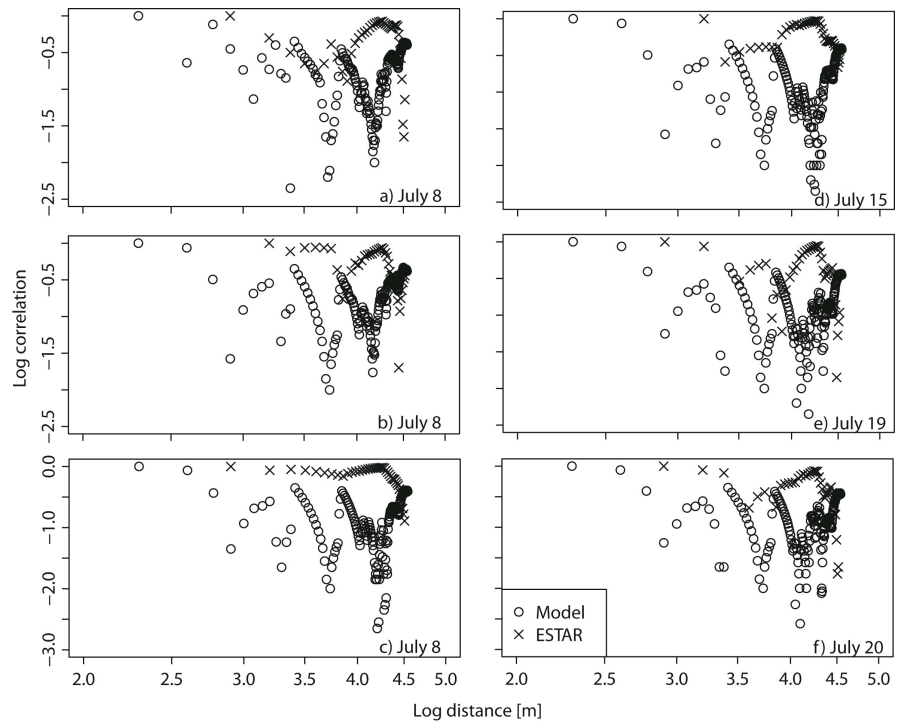

Figure 5.12: Spatial correlation of soil moisture along the transect (Fig. 5.10) for the top 5cm soil layer for: a) July 8, b) July 9, c) July 14, d) July 15, e) July 19, and f) July 20, 1999.

5.3 Soil moisture variograms

Figures 5.13 and 5.14 present the soil moisture variograms for ESTAR estimates and GEOtop simulations during the SGP97 and SGP99, respectively, while the properties of the variograms are presented in tables 5.1 and 5.2, respectively. The experimental variograms of both simulated and ESTAR soil moistures are fitted with spherical theoretical models that well fit the experimental variograms. During the SGP97 the watershed was relatively wet, while during the SGP99 the watershed was dry.

During the SGP97 (Fig. 5.13 and table 5.1) GEOtop simulations show large nugget, implying high subgrid variability (Western and Blöschl 1999), while ESTAR estimates show low nugget, meaning that ESTAR smoothes the subgrid variability. Remember that the model support is 200m, while the ESTAR support is 800m, and that the model and ESTAR are different techniques for estimating soil moistures. Generally, both ESTAR estimates and GEOtop simulations show that the nugget decreases as soil dries, and increases as soil wets up. This means that the subgrid variability decreases as soil dries, and increases as soil wets up. In a case of a measurement, the nugget is the sum of the measurement errors and the subgrid variability (Blöschl and Grayson, 2000). Similarly, both ESTAR estimates and GEOtop simulations show that the variance (sill) decreases as soil dries and increases as soil wets up. During the dry-down period (July 11 - 14), as soil dries, simulated soil moisture range decreases, while ESTAR soil moisture range increases. Generally, GEOtop simulations show that soil moisture correlates well to larger scales compared to the ESTAR estimates.

ESTAR experimental variogram on July 16 is shown to be nonstationary. It suggests that the variogram is stationary at scale larger than the considered scale. The nonstationary variograms is likely to be well fitted with linear models than the spherical models. Therefore, the variogram properties are highly affected by the considered scale.

Furthermore, we investigated the soil moisture anisotropy in different directions. The investigation is carried out only for July 12, 1997, because on this day the watershed is moderately wet, for moderately wet watersheds, the soil moisture shows high degree of spatial organization (Western et al. 1999). The analysis of soil moisture anisotropy is presented in section 6.2.

Table 5.1 : Variograms properties of simulated and ESTAR soil moisture during SGP97

Day	GEOtop simulations			ESTAR estimates		
	Nugget	Sill	Range (m)	Nugget	Sill	Range (m)
July 11	0.0030	0.0056	10448.15	0.0015	0.0066	3928.23
July 12	0.0035	0.0055	7244.243	0.0013	0.0054	4665.08
July 13	0.0031	0.0047	5307.736	0.0009	0.0037	5144.216
July 14	0.0027	0.0041	5152.216	0.0008	0.0033	5261.572
July 16	0.0029	0.0044	7289.494	0.0012	0.0083	9389.073

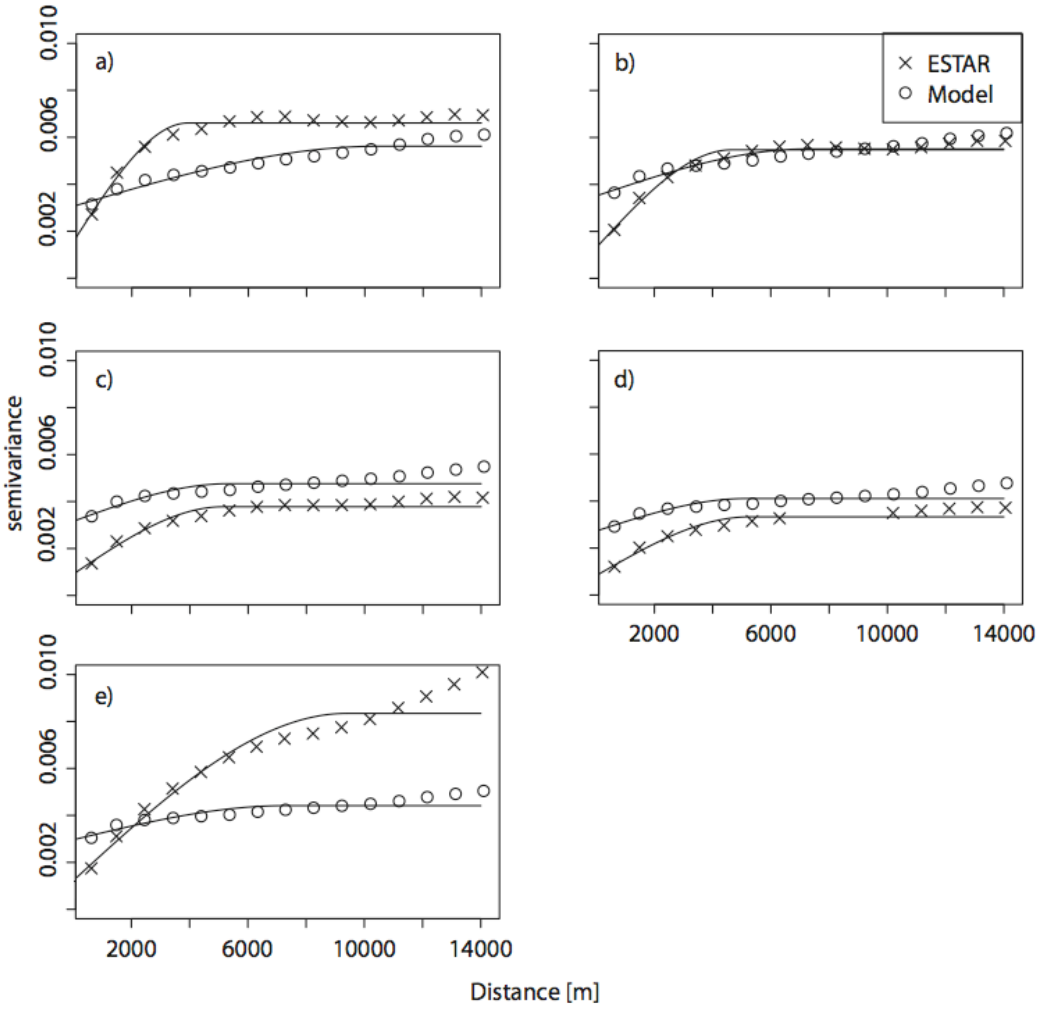

Figure 5.13: Soil moisture variograms of the top 5cm soil layer for the Little Washita watershed for: a) July 11, b) July 12, c) July13, d) July14, and e) July16, 1997.

During the SGP99 (Fig. 5.14 and table 5.2) and similar to what happened during the SGP97, GEOtop simulations show large nugget, implying high subgrid variability, while ESTAR estimates show almost no subgrid variability. In comparison to the GEOtop simulations, ESTAR estimates show very low sill. Although GEOtop simulations show relatively high sills, the variability between the elements (sill - nugget) shown by GEOtop simulations is very similar to the variability between the elements shown by ESTAR estimates. This suggests that the differences between ESTAR estimates and GEOtop simulations are highly affected by the nugget that is mainly attributed to the subgrid variability. GEOtop simulations show that the soil moistures correlate well at small scales, while ESTAR estimates show that the soil moistures correlate well at large scales.

Western et al. (1998) studied the geostatistical characterization of soil moisture patterns in Tarrawarra catchment, and they found that for wet conditions the sill is high and the correlation length is short, and for dry conditions the sill is low and the correlation length is long. This is in agreement with our findings for both ESTAR estimates and GEOtop simulations during the SGP97 and SGP99, but GEOtop simulations show long correlation length for wet conditions; SGP97, and short correlation length for dry conditions; SGP99.

From figures 5.13 and 5.14 and tables 5.1 and 5.2 we observe that the soil moisture correlation range estimated along the transect (see section 5.2) corresponds well with the soil moisture range estimated with variograms.

Table 5.2: Variograms properties of simulated and ESTAR soil moisture during SGP99

Day	GEOtop simulations			ESTAR estimates		
	Nugget	Sill	Range (m)	Nugget	Sill	Range (m)
July 8	0.0018	0.0023	2755.855	0.000038	0.0003	10607.8
July 9	0.0016	0.0020	2624.432	0.00003	0.0004	15241.91
July 14	0.0011	0.0015	3245.392	0.000007	0.0005	12142
July 15	0.0011	0.0015	3360.688	0.000009	0.0004	10308.18
July 19	0.0012	0.0015	4933.548	0.00002	0.0002	10475.55
July 20	0.0012	0.0016	5292.643	0.000018	0.0001	7932.047

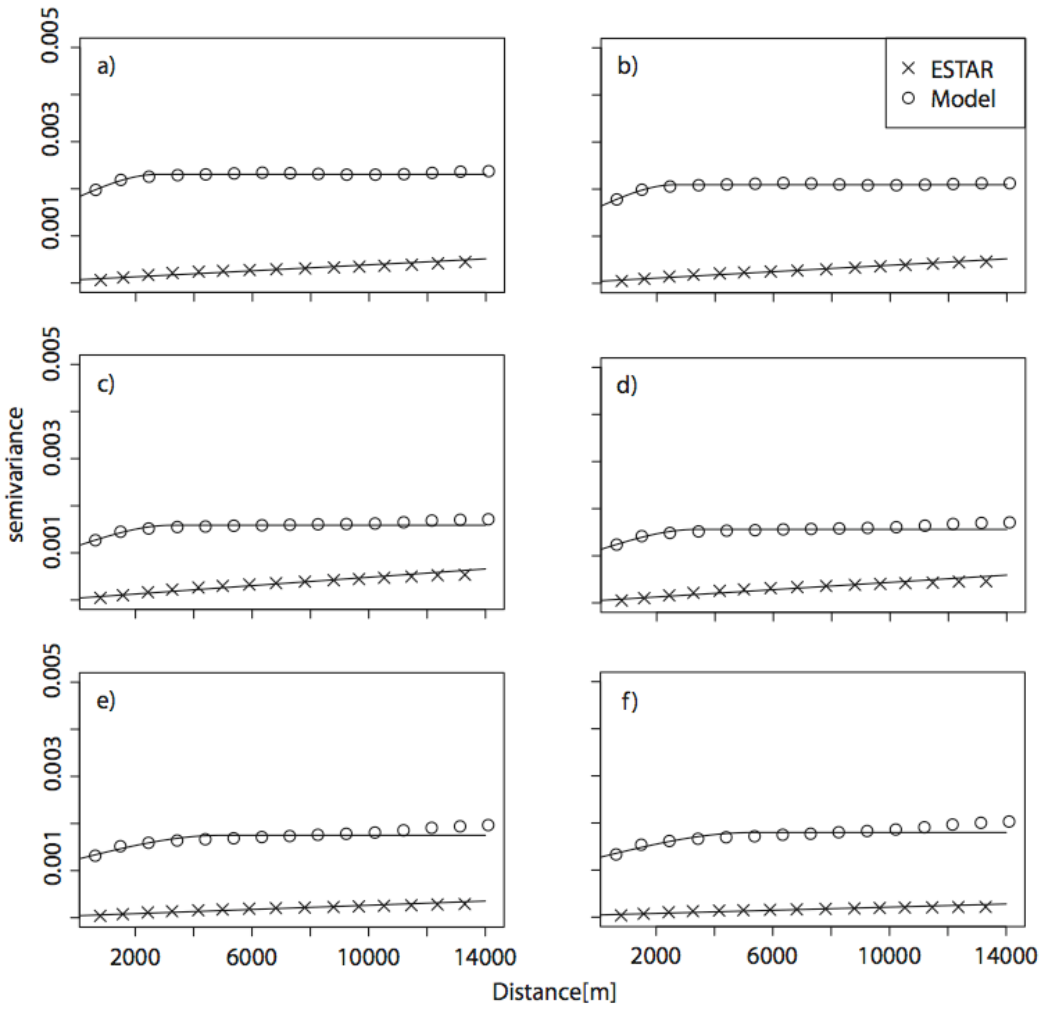

Figure 5.14: Soil moisture variograms of the top 5cm soil layer for the Little Washita watershed for: a) July 8, b) July 9, c) July14, d) July15, e) July19, and f) July 20,1999.

5.4 Re-thinking the soil moisture assessment in SGP experiments

Here, we only compare our findings obtained during the SGP97 with the previous studies that were conducted in the Little Washita watershed. This is because during the SGP97, the soil moisture varies in a large range, while during the SGP99, the soil moisture varies in a short range; the watershed was dry.

According to our results for both soil types (sandy loam and silt loam), GEOtop simulations exhibit a downward quadratic relationship between the spatial STDEV and the spatial mean of near-surface soil moisture (i.e., STDEV is low when the soil is dry, then increases with increasing wetness until a certain threshold of mean soil moisture, beyond which the STDEV decreases with increasing wetness level, becoming low when

the soil is saturated), while ESTAR estimates exhibit a linear increase of the spatial STDEV with the spatial mean. Famiglietti et al. (2008) based on ground-based volumetric soil moisture measurements collected from three field campaigns in the study area (SGP97, SGP99, and SMEX03), Vereecken et al. (2007) based on an analytical stochastic model, Pan and Peters-Lidard (2008) and Pan and Peters-Lidard (2010) based on theoretical approach reported a downward relationship between the spatial STDEV and spatial mean, consistent with our results for the GEOtop simulations. However, Pan and Peters-Lidard (2010) fitted the downward relationship between the standard deviation and the spatial mean of soil moisture with third order polynomial. If the two low ends of the curve are known, the relationship between the standard deviation and the spatial mean can be fitted with second order polynomial. In our GEOtop simulations, we fit this relationship with second order polynomial because the standard deviation is zero at the two low ends of the curve (when the watershed at saturation and wilting point).

According to our results for both soil types, GEOtop simulations show that the spatial frequency distribution of near-surface soil moisture depends on the state of the soil moisture, it has positive skewness at low spatial mean soil moisture, zero skewness at moderate spatial mean soil moisture, and negative skewness at high spatial mean soil moisture. This is consistent with the results reported by Famiglietti et al. (1999) based on ground-based volumetric soil moisture measurements. While our results for ESTAR estimates show that the spatial frequency distribution of near-surface soil moisture has zero skewness regardless of the state of the soil moisture.

According to our results for both soil types, GEOtop simulations show that the soil moisture distribution can be approximated by beta distribution consistent with the findings of Famiglietti et al. (1999), while ESTAR estimates show that the soil moisture distribution can be approximated by normal distribution.

GEOtop simulations are in agreement with the previous findings obtained in the watershed using ground-based measurements. Furthermore, GEOtop simulations are in agreement with the theoretical models of soil moisture. So, we conclude that GEOtop simulations are more accurate than ESTAR estimates.

5.5 Conclusion

In this chapter, we characterized the spatial and temporal variability of the near-surface soil moisture derived from two sources of data: estimation obtained from the L-band ESTAR microwave radiometer observation on board aircraft, and simulation obtained from the physically-based GEOtop hydrological model using SGP97 and SGP99 datasets. During the SGP97 the watershed was relatively wet, while during the SGP99, the watershed was dry. We found that it is important to study soil moisture variability when the soil moisture varies in a large range. Results show that the GEOtop simulations and ESTAR estimates show very different spatial patterns of near-surface soil moisture. Whereas ESTAR estimates do not show any control of river network on the spatial distribution of the near-surface soil moisture, GEOtop simulations clearly show the control of river network on the spatial distribution of the near-surface soil moisture. Whereas ESTAR estimates show a linear functional relationship between the spatial STDEV and spatial mean (and also between the spatial CV and spatial mean) of soil moisture, GEOtop simulations show a downward quadratic relationship. Whereas ESTAR estimates show zero skweness for the spatial frequency distribution regardless of the spatial mean soil moisture level, GEOtop simulations show positive skewness at low spatial soil moisture, zero skewness at moderate spatial mean soil moisture, and negative skewness at high spatial mean soil moisture. Compare to previous findings based on ground-based measurements of soil moisture and theoretical models indicate that the GEOtop simulations are more accurate. It is concluded that the ESTAR estimates do not provide a reliable source of soil moisture data for characterizing the spatial patterns of near-surface soil moisture.

6 Comparison of the geostatistical techniques with dynamical modeling

This chapter uses geostatistical techniques to reproduce the simulated soil moisture patterns obtained by GEOtop model. The objective is to know how well can we reproduce the simulated soil moisture patterns using geostatistical techniques? What is the best kriging technique should be used to reproduce the patterns? Can we use geostatistical techniques to establish sustainable network for soil moisture measurements in the study area? The study area is Little Washita watershed (583 km^2), Oklahoma, USA. The high- resolution (200m) simulated volumetric soil moisture map produced from the SGP97 simulation (see chapter 4) on July 12, 1997, is used as an input map.

Some soil moisture measurement points are carefully selected, considering the effects of the controlling factors of the soil moisture variability in the watershed, to form the network. Different kriging techniques are used: Ordinary kriging (OK) and external drift krigings (EDKs). Using OK, and predictors (e.g., terrain indices) for EDK, soil moisture maps are produced and compared to the simulated soil moisture map (input). Suitability of the proposed soil moisture network is tested. Finally, soil moisture patterns are studied using conditional Gaussian simulations.

6.1 Setup of soil moisture measurement network

The spatial patterns of hydrological processes have high degree of variability and have different degree of spatial organization. The degree of spatial organization can be critically important in hydrological science, for instance, in runoff simulations (Western et al. 1999), risk analyses (e.g., landslide triggering), design measurement strategies, data interpretation, and biogeochemical processes. The spatial patterns of hydrological processes depend on spacing, support, and extent scales of the measurements (Blöschl and Grayson, 2000). Representation of the spatial variability of soil moisture is needed at different scales. An accurate way to represent the spatial variability is to use distributed models (Western et al. 1999). However, distributed models require huge amount of data that is not always available. A relatively simple method is to use

geostatistical techniques (e.g., Bárdossy and Lehmann 1998; Western et al. 1999). The main purpose of this work is to know how well can the geostatistical techniques reproduce the spatial soil moisture patterns that are obtained by distributed models?
Western et al. (1999) show that terrain indices are found to be powerful tools for reproducing the spatial patterns of soil moisture when they used as predictors for kriging algorithms. To explore the potentials of the terrain indices, the terrain indices of the Little Washita watershed are used as predictors for EDK. The role of each terrain index on soil moisture distribution, and the limits of the terrain indices are also discussed in Western et al. (1999). Furthermore, Western et al. (1999) have reviewed the application of terrain indices in other watersheds, and they reported that terrain indices have worked well for some watersheds and have worked poorly for other watersheds. In another study, Bárdossy and Lehmann (1998) concluded that the external drift indicator kriging and Bays Markov updating (BMU) are the best algorithms for reproducing the spatial patterns of soil moisture.

In this study, we used the simulated volumetric soil moisture map for the top 5cm soil layer produced from the SGP97 simulation on July 12, as an input map, and we used OK, and EDK to reproduce the spatial soil moistures. The last rainfall event in the watershed before July 12 was on July 10, 1997. So, on July 12, the watershed is relatively wet, according to Western et al. (1999) in moderately wet watersheds, the soil moisture shows high degree of organization, while in dry watersheds, the soil moisture shows little spatial organization.
The predictors that are used for the EDK are: Digital Elevation Model (DEM), gradient, cosine aspect, wetness index, longitudinal curvature, soil depth, laplacian, coordinates, river network, hydraulic conductivity, and their combinations. The kriging algorithm is called universal kriging (UK) when the coordinates are used as predictors for EDK. All predictors except DEM, soil depth, hydraulic conductivity, and coordinates are derived from DEM using JGRASS-GIS (www.jgrass.org). These indices are chosen because, generally, they play crucial role in soil moisture distribution in watersheds.

In this study, the effect of soil type on OK and EDKs is considered implicitly by taking soil moisture measurement points (actually from GEOtop simulations) in different soil types and for each soil type different values of soil moistures are selected. This is because the soil type is found to be the main controlling factor of the soil moisture

distribution in the watershed (see chapter 4). In addition, the effect of the landuse type on the spatial soil moistures is considered implicitly by taking the soil depth map as predictor for the EDK. The distribution of landuse classes depends on the soil depth to a large extent. 240 soil moisture measurement points are selected to form the soil moisture network. Webster and Oliver (2007) recommend that at least 50 measurement points should be considered to have reliable experimental variogram, while Western et al. (1998) recommend about 300 measurement points to have meaningful sample variogram. The fitted theoretical variogram of the 240-points is used for kriging soil moistures with OK algorithm.

The simulated soil moisture content on July 12, 1997, and the locations of the selected measurement points are shown in figure 6.1. All the analyses are carried out using R programming language (http://www.r-project.org) and the JGRASS-GIS interface (www.jgrass.org).

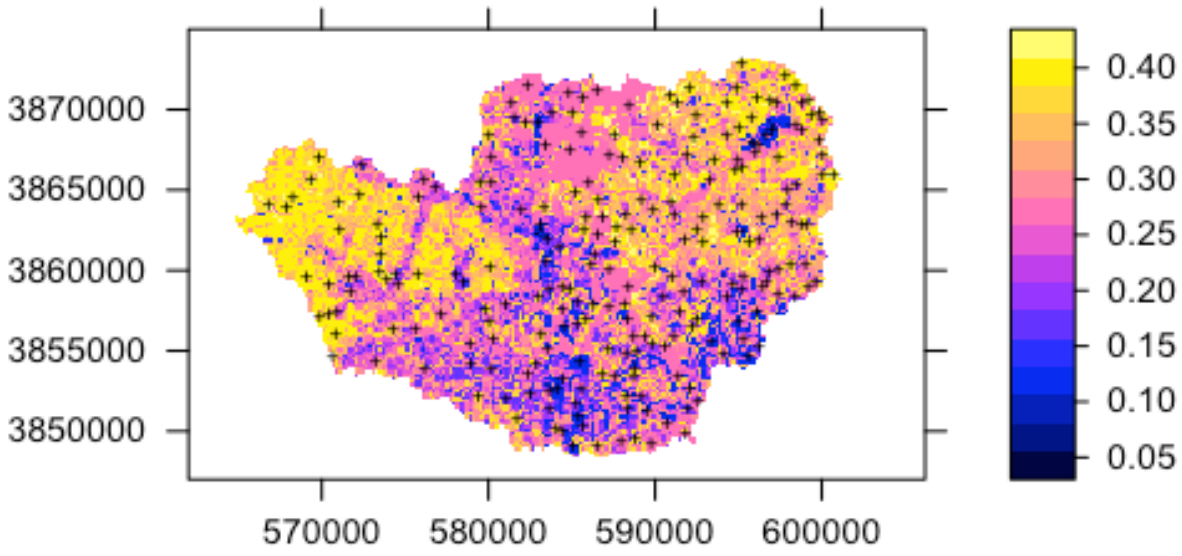

Figure 6.1: Simulated volumetric soil moisture content [-] on July 12, 1997 for the top 5cm soil layer, and the locations of the selected 240 points of the soil moisture network shown in (+).

6.2 Results and discussions

6.2.1 Variogram

Figure 6.2 shows the experimental variograms of the simulated soil moisture and the soil moisture of the selected 240-points fitted with spherical models. The experimental variograms are reasonably fitted with the theoretical models, and the variograms have defined sills and ranges. A defined sill indicates that the soil moisture is stationary. The properties of the fitted variograms of the simulated soil moisture and the selected 240-points are shown in table 6.1. The two variograms differ mainly on the range and nuggets. However, the variabilities between the elements (sill-nugget) are similar. This indicates that the 240-points capture the statistics of the spatial structure of the soil moisture. Furthermore, we investigated soil moisture anisotropy in four directions. If the soil moisture field is anisotropic, this anisotropy has to be considered when computing the soil moisture variograms that are subsequently used by krigings to generate the spatial soil moisture patterns. This analysis of directional variograms shows that the soil moisture field is isotropy. Figure 6.3 shows the directional experimental variogram of the selected 240 points fitted with the same spherical model used in figure 6.2, without considering any anisotropy. As the number and the configuration of the data-points affect the reliability of the experimental variogram, the number and the configuration of the selected points seem reasonably enough to have reliable experimental variogram.

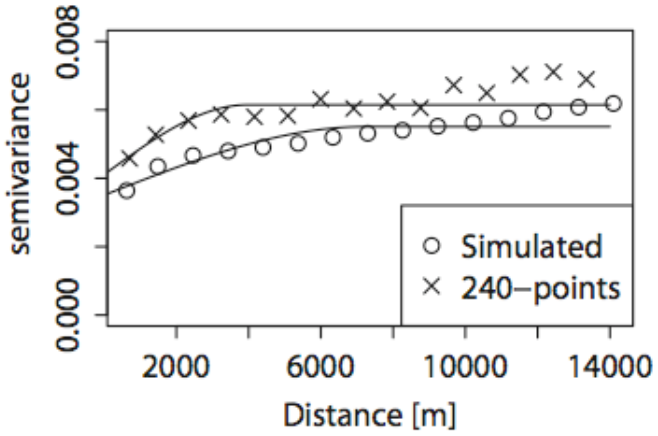

Figure 6.2: Experimental variograms of the simulated soil moisture (original map) and the soil moisture of the selected 240-points fitted with spherical models.

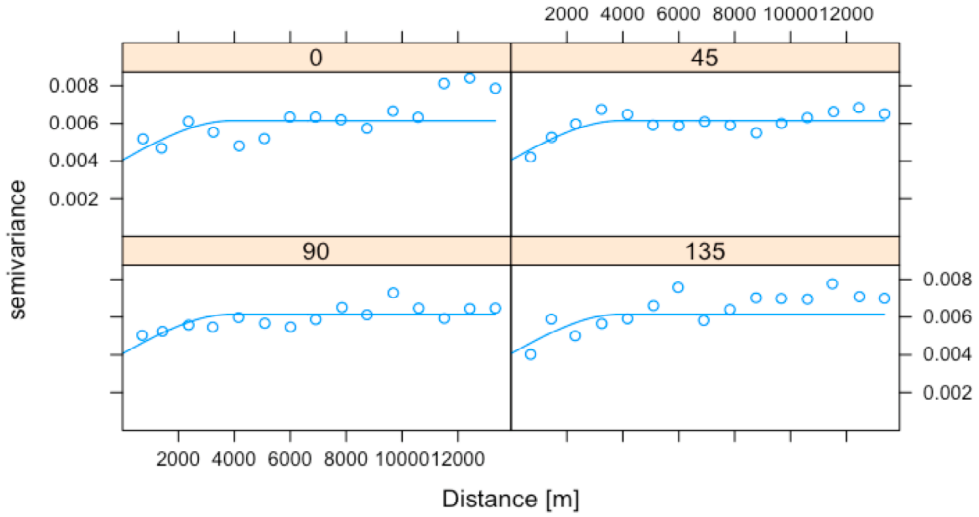

Figure 6.3: Variogram of the soil moisture for the selected 240 points in four directions.

Following the decision tree for selecting the right spatial prediction technique, as proposed by Hengl (2009), the EDK is found to be the right predicting algorithm since all the residuals clearly show spatial autocorrelation. Figure 6.4 shows the variogram of the residuals fitted with spherical model for the case that uses all predictors except river network, hydraulic conductivity, and coordinates for EDK. While the variogram of the residuals of all other predictors of the EDK are presented in appendix B. The properties of the variograms of the residuals are also shown in table 6.1. The nuggets for the variograms of the residuals obtained using gradient, gradient and cosine aspect, and all predictors except river network, hydraulic conductivity and coordinates as predictors for EDK are lower than the nugget of the simulated soil moisture map. It is interesting to note that when using gradient, gradient and cosine aspect, and all predictors except river network, hydraulic conductivity and coordinates as predictors for EDK reproduced the closest patterns to the actual patterns (see section 6.2.2). The nugget in both soil moistures (the case of OK) and residual variograms can be attributed mainly to the subgrid variability. The nugget due to the subgrid variability will disappear if the data are taken at sufficiently small spacing (Blöschl and Grayson, 2000).

According to Western et al. (1999), the value of variogram of the soil moisture at a given lag represents the total variance at that lag, while the value of the variogram of the residuals represents the unexplained variance at that lag. The difference between the value of the variogram of the soil moisture and the residuals at a given lag represents the explained variance at that lag. From table 6.1 it is evident that the variogram of soil moisture is very similar to the variograms of the residuals for all the predictors. So, as

the variogram of the soil moisture is very similar to the variograms of the residuals, meaning that there is no significant variance is being explained considering the above-mentioned predictors for EDK. Furthermore, we observe weak correlation between the soil moisture and the predictors, as shown in table 6.2. In the case of no correlation between the soil moisture and the predictors, the EDK gives results very similar to the OK (e.g., Goovaerts, 1997; Bárdossy and Lehmann, 1998). The weak correlation is likely due to the subgrid variability. Western et al. (1999) have used terrain indices as predictors for EDK, and they reported that the subgrid variability cannot be captured by the terrain indices and can contribute significantly to the performance of the terrain indices.

Table 6.1: Properties of variograms of soil moisture and residuals, and mean of residuals of soil moisture

Predictor	Nugget	Sill	Range (m)	Mean of residuals of soil moisture [%]
Simulated map (original)	0.0035	0.0055	7244.243	-
OK (240-points)	0.0041	0.0061	3959.020	-0.09
Elevations (DEM)	0.0040	0.0060	3136	0.08
Gradient	0.0034	0.0060	2158.4	0.25
Cosine aspect	0.0043	0.0060	3489.2	-0.04
Wetness index	0.0041	0.0061	4046	0.14
Longitudinal curvature	0.0043	0.0061	6243	0.08
Soil depth	0.0042	0.0061	3721.6	-0.03
Laplacian	0.0042	0.0061	4652	-0.02
Coordinates	0.0039	0.0058	2860.083	-0.12
River network	0.0040	0.006	3765.4	0.09
Gradient and cosine aspect	0.0031	0.0059	2187	0.21
Hydraulic conductivity	0.0040	0.0061	3962.4	-0.32
All predictors except river network, hydraulic conductivity, and coordinates	0.0031	0.0056	2083.2	-0.29

For OK, the variogram is for soil moistures, while for others the variograms are for residuals. The mean of residuals is obtained from kriging cross validation.

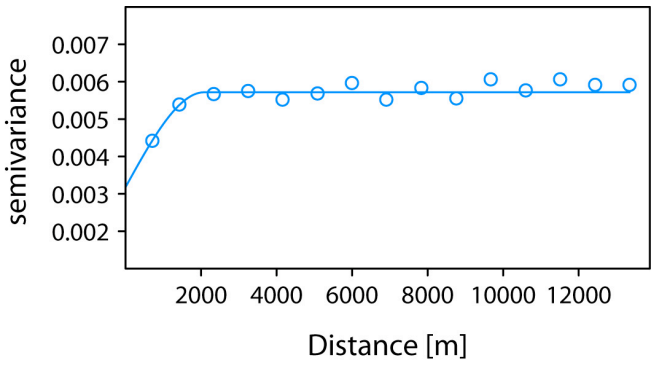

Figure 6.4: Variogram of the residuals combining all predictors except river network, hydraulic conductivity, and coordinates for EDK, fitted with spherical model.

Table 6.2: Correlation coefficient for the relationships between volumetric soil moistures and predictors

Predictor	Correlation coefficient
Elevations (DEM)	-0.207
Gradient	-0.197
Cosine aspect	+0.055
Wetness index	-0.13
Longitudinal curvature	+0.084
Soil depth	-0.084
Laplacian	-0.032
Coordinates	+0.367
River network	+0.158
Gradient and cosine aspect	+0.286
Hydraulic conductivity	-0.095
All predictors except river network, hydraulic conductivity, and coordinates	+0.362

The sign of the correlation is indicated by the plus or minus before the correlation coefficient.

6.2.2 Spatial soil moisture patterns

Figure 6.5 shows soil moisture patterns reproduced by the OK and the EDK using different predictors, and in comparison to the original simulated soil moisture map that has to be reproduced.

From visual comparison, it is evident that when using gradient and to some extent cosine aspect as univariate predictors for EDK, produce the best soil moisture patterns that are more close to the actual patterns. Western et al. (1999) they also used EDK, and found that cosine aspect and potential solar radiation index are the best univariate predictors to reproduce the spatial patterns during dry periods. The combination of gradient and cosine aspect as predictor for EDK has improved the patterns. Nevertheless, the reproduced patterns are very similar to the patterns reproduced using gradient as univariate predictor for EDK. This indicates the strong control of gradient on the soil moisture distribution in the watershed for the current wetness condition.

The combination of all predictors except river network, hydraulic conductivity, and coordinates for EDK reproduced the best spatial patterns. Even though, the reproduced patterns are similar to the patterns reproduced using gradient, cosine aspect, and the combination of gradient and cosine aspect as predictors for EDK. This further indicates the strong influence of gradient and cosine aspect in the reproduced spatial patterns. The uses of the other univariate predictors (elevations, wetness index, longitudinal curvature, soil depth, laplacian, river network, hydraulic conductivity, and coordinates) for the EDK have poorly reproduced the patterns. It is interesting to note that although the soil type controls the soil moisture distribution in the watershed, the soil moisture patterns obtained using hydraulic conductivity (soil type was classified further depending on the hydraulic conductivity) as a univariate predictor for EDK are very different from the actual patterns. This indicates that the soil hydraulic conductivity is not a good predictor for EDK. It is important to note that the hydraulic conductivity map that is used as predictor for EDK is classified for a certain ranges of hydraulic conductivities. This suggests that the hydraulic conductivity is a property of the soil, and it is not appropriate to consider the hydraulic conductivity as an external drift for kriging. However, it is important to include the soil type (also including the hydraulic conductivity) as a categorical variable for indicator kriging, and then combining the indicator kriging with external drifts (predictors) to obtain external drift indicator kriging. In our analyses the EDK implicitly includes indicator kriging.

The spatial patterns reproduced using soil depth as predictor for EDK, are very similar to the patterns reproduced by the OK. The poorly reproduced patterns using soil depth as predictor for EDK indicate that the spatial soil moisture patterns do not depend on vegetation distribution.

Poorly reproduced spatial soil moisture patterns using wetness index as univariate predictor for EDK indicate that the saturation excess is not the dominant runoff process in the watershed. Wetness index is a good predictor for the situations at which the saturation excess is the dominant runoff process (e.g., Blöschl and Grayson, 2000). Furthermore, the UK produces spatial patterns very similar to the patterns reproduced by the OK. Comparing the OK patterns with the EDK patterns, generally, the EDKs show the soil moisture patterns better than the OK, and the OK patterns are very smoothed. When there is no correlation between the soil moistures and the predictors, the EDK tends to OK. Although there are weak correlations between the soil moistures and the predictors, the reproduced spatial patterns of soil moistures are improved very much when using gradient and cosine aspect as univariate or bivariate predictor for EDK.

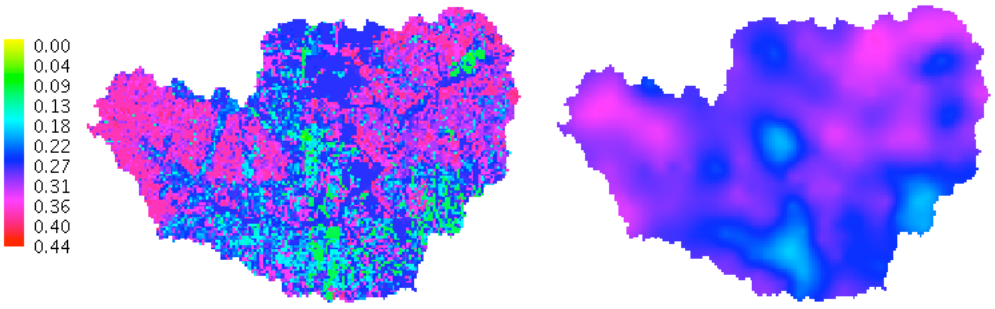

a) Simulated soil moisture b) OK

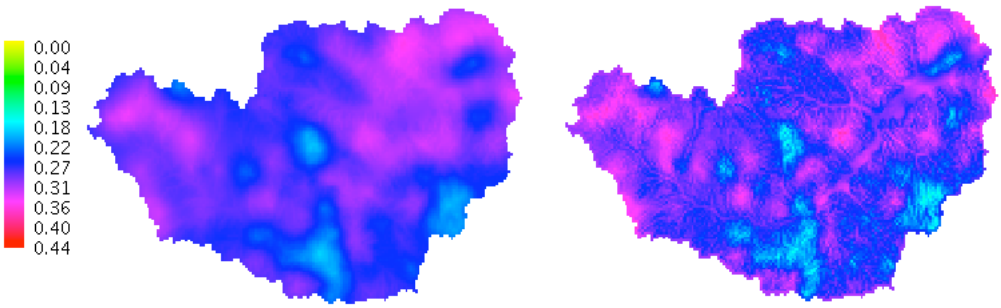

c) Elevations d) Gradient

Figure continues in the next page

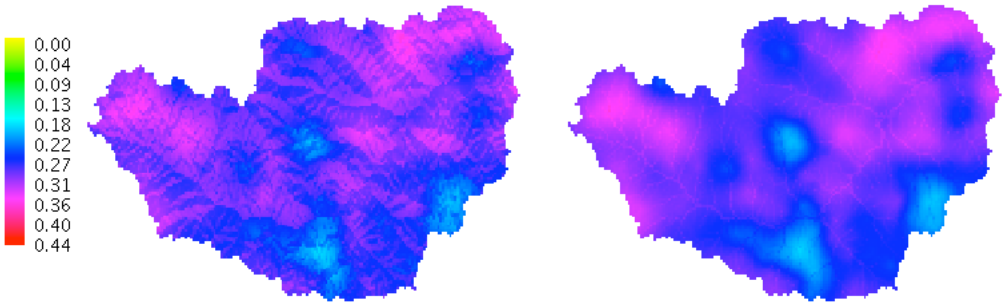

e) Cosine aspect

f) Wetness index

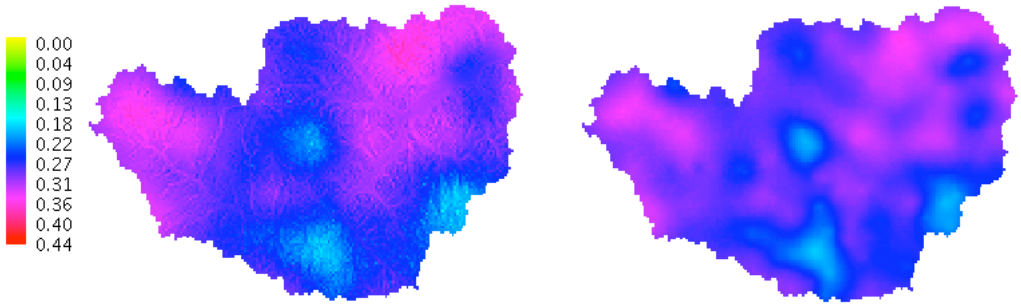

g) Longitudinal curvature

h) Soil depth

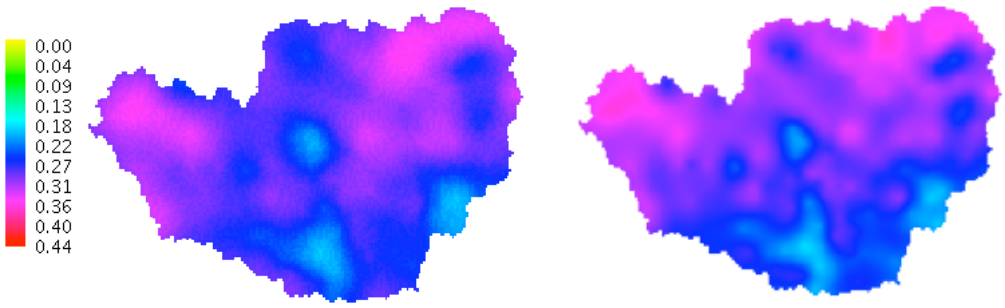

i) Laplacian

j) Coordinates

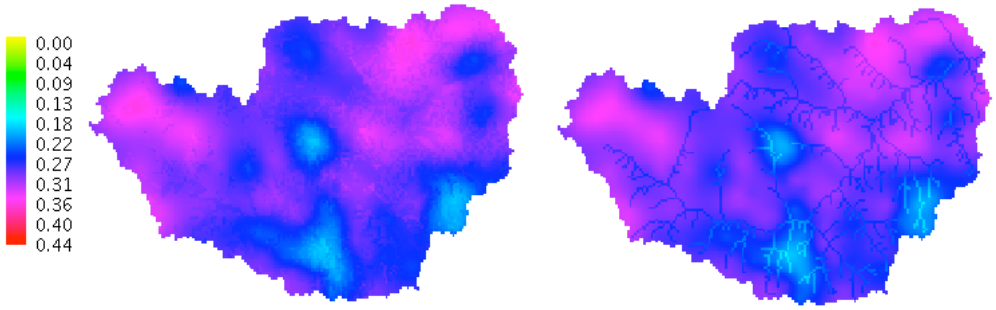

k) Hydraulic conductivity

l) River network

Figure continues in the next page

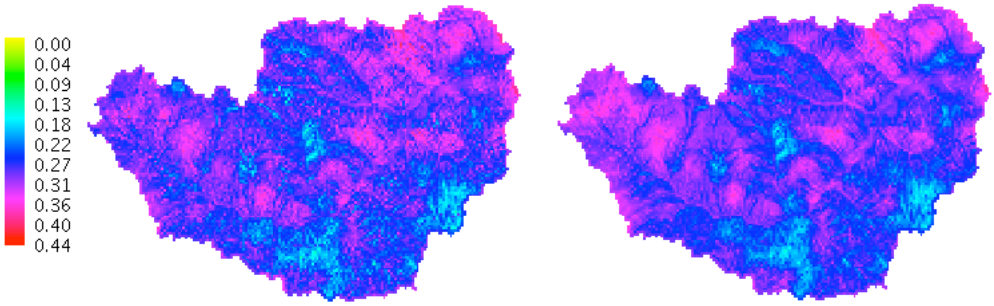

m) All predictors except river network, hydraulic conductivity, and coordinates

n) Combination of gradient and cosine aspect

Figure 6.5: Simulated and Kriged soil moistures for OK and for EDK using different predictors.

Figures 6.6, and 6.7 and table 6.1 show soil moisture variance, soil moisture residuals, and the mean of residuals, respectively. In figures 6.6 and 6.7, the soil moisture variance maps and the soil moisture residuals are shown only for the case in which all predictors except river network, hydraulic conductivity, and coordinates are used for EDK. The soil moisture variance maps and the soil moisture residual maps for all other predictors of EDK are presented in appendix B. Although all krigings show low soil moisture variance, OK, and EDK that uses soil depth as predictor have the highest soil moisture variance. Values around zero of the mean of the residuals indicate that the kriging estimates are unbiased. Western et al. (1999) reported that if the terrain indices captured the key topographic control on soil moisture, the residual maps should appear random. As shown in figure 6.7 and figure B.3 (appendix B), all the maps have similar residuals, and the residuals are randomly distributed. Although there are little differences between the produced residual maps, the soil moisture patterns have improved very much when using gradient and cosine aspect as univariate or bivariate predictor for EDK, and when using all predictors except river network, hydraulic conductivity, and coordinates as multivariate predictor for EDK. The residual maps show that some soil moisture patterns in the southern part of the watershed are not well captured by the EDKs. In these areas more points could be added to further improve the prediction.

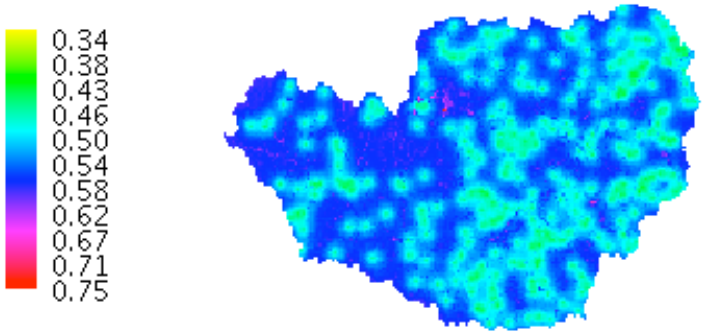

Figure 6.6: Kriged soil moisture variance [%] obtained using the combination of all predictors except river network, hydraulic conductivity and coordinates as predictor for the EDK.

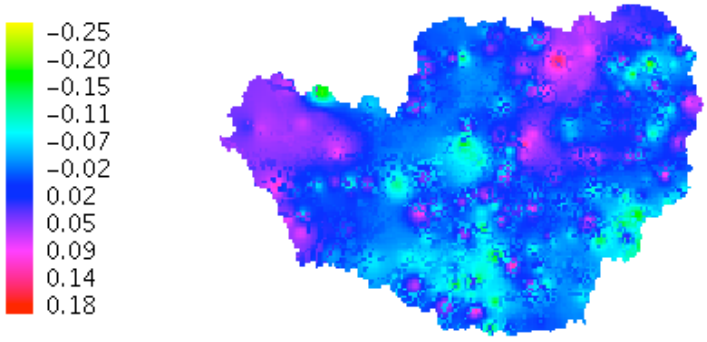

Figure 6.7: Soil moisture residuals obtained applying kriging cross validation. The applied kriging is EDK that uses all predictors except river network, hydraulic conductivity and coordinates as predictor.

Although the OK and EDKs reproduced different soil moisture patterns, all krigings reproduced similar residuals and variances. This indicates that reproducing the soil moisture measurements do not necessarily mean reproducing the actual soil moisture patterns. This is consistent with the findings of Bárdossy and Lehmann (1998) who characterized the spatial distribution of measured soil moistures in an experimental watershed in Germany applying 5 different kriging algorithms. They found that OK and indicator kriging are applicable, but they did not show any spatial distribution of the soil moisture, while EDK shows good spatial soil moisture patterns, but the estimated soil moisture values are often outside the measurement range; only for the extreme measurements. On the other hand, they found that the external drift indicator kriging

and the BMU that also considers the effects of landuse and soil type are the best algorithms for reproducing the spatial soil moisture patterns. Consistent with our findings, they concluded that all kriging algorithms are unbiased.

In this study, the indictor kriging is included implicitly in the OK and in the EDKs by considering the effects of landuse and soil type on the soil moisture distribution. As mentioned above, the uses of soil depth (landuse) as predictor for EDK is poorly reproducing the soil moisture patterns. Considering the external drift indicator kriging as the best algorithm for reproducing the spatial soil moisture patterns, and as the soil depth (as surrogate of landuse) is poorly reproducing the patterns, the soil type is the only categorical variable that is used for the indicator kriging. Therefore, the uses of the soil type as indicator for EDK is reasonably reproducing the spatial soil moisture patterns if the right predictor accompanies it. This means the spatial soil moisture patterns in the Little Washita watershed are controlled by topography and heterogeneity of soil porosity, at least for the considered wetness condition.

Thus it concluded that the selection of the right predictor for the external drift (indicator) kriging is the best way to reproduce the spatial soil moisture patterns. Although the selection of the 240 points with their existing coordinates is reasonably enough to establish soil moisture measurement network, it is recommended to add new measurement points in the southern part of the watershed to further improve the prediction of the soil moisture patterns. It is also recommended to repeat this procedure several times using different soil moisture levels to establish permanent soil moisture measurement network.

6.2.3 Soil moistures frequency distributions

To further investigate the capabilities of the predictors for reproducing the spatial soil moisture patterns, the frequency distribution of soil moistures that are reproduced using different indicators for the EDK and using OK are plotted and compared to the frequency distribution of the simulated soil moistures as well as to the frequency distribution of the soil moisture of the selected 240 points.

Figure 6.8 shows the frequency distribution of the simulated soil moistures, soil moisture of the selected 240 points, and the kriged soil moistures. The frequency distribution of the simulated map is very similar to the frequency distribution of the selected 240 points. This indicates the representation of the selected 240 points to the

watershed soil moistures. All the kriged soil moistures showed to have normal distribution, while the simulated soil moistures and the soil moistures of the selected 240 points somehow showed to have bimodal distributions. The frequency distribution obtained using gradient as predictor for EDK has captured part of the high soil moistures and fails to capture the low soil moistures. The frequency distribution reproduced using all predictors (multivariate) except river network, hydraulic conductivity, and coordinates for the EDK is similar to the frequency distribution reproduced using gradient and cosine aspect as univariate predictors for EDK. This indicates that the gradient and cosine aspect are significantly influencing the frequency distribution of the soil moisture, when they used as predictors for EDK. The frequency distribution reproduced using all predictors except river network, hydraulic conductivity, and coordinates for EDK is the only frequency distribution has soil moisture class higher than 0.4. It is noted that the closer the frequency distribution, that reproduced using a predictor for the EDK and using OK, to the simulated frequency distribution, the good the reproduced the soil moisture patterns. This is in disagreement with Western et al. (1999) who reported that a terrain index can well reproduce the soil moisture distribution function, but it is not necessarily reproducing the spatial soil moisture patterns. From figure 6.8 it is also evident that no frequency distribution is well capturing the low values of soil moisture. Even when multivariate predictor is used for EDK, the reproduced frequency distribution is partially capturing the high soil moisture values. This concludes that kriging algorithms should be used with caution for extreme values. This is consistent with the findings of Goovaerts (1997) who reported that the kriging algorithms typically overestimate the low values and underestimate the high values.

For the current wetness condition in the watershed, the use of gradient and cosine aspect as predictors for EDK showed to have the greatest influence on the reproduced soil moisture patterns. Under different wetness conditions, other controlling factors might have significant influence on the spatial distribution of the soil moisture patterns.

The main uncertainties in the analyses are associated to the quality of the DEM; DEM is always obtained by interpolation, and to the derived geomorphological maps. Other uncertainties depend on the type of the fitted variograms. Blöschl and Grayson (2000) reported that the type of the fitted variogram is highly influencing the interpolated soil moistures.

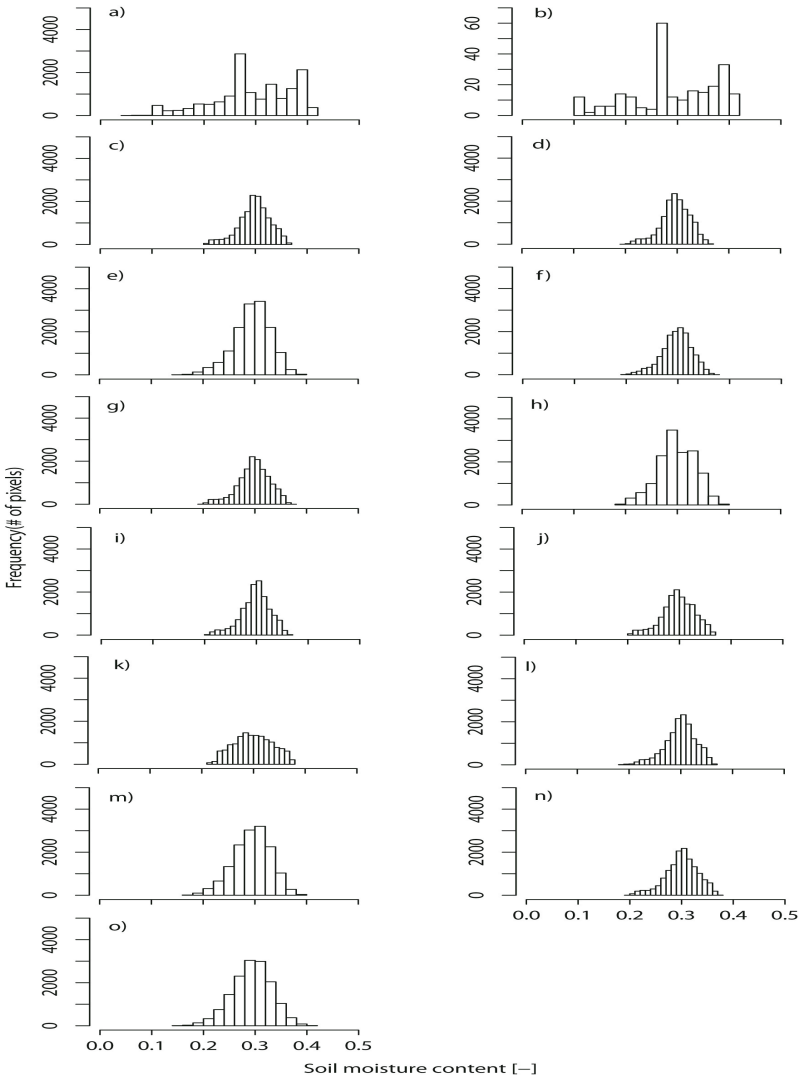

Figure 6.8: Soil moisture frequency distributions of the top 5cm soil layer for: a) Simulated soil moisture, b) Selected 240 points, c) OK, d) Elevations, e) Gradient, f) Cosine aspect, g) Wetness index, h) Longitudinal curvature, i) Soil depth, j) Laplacian, k) UK, l) River network, m) Combination of gradient and cosine aspect, n) Hydraulic conductivity, and o) All predictors except river network, hydraulic conductivity, and coordinates.

6.3 Sensitivity analysis of the soil moisture network

The purpose of this section is to know whether the spatial soil moisture patterns change when the locations of the soil moisture measurement points change, considering the same approach that was applied in section 6.1. This is to test the robustness of the applied approach. In what follow, we called the soil moisture network described in section 6.1 and figure 6.1 network A, while the new soil moisture network that is

formed after changing the locations of the measurement points of network A, network B. So, both networks are composed of 240-points.

The soil moisture measurement points of network A are selected in different soil types, and for each soil type different values of soil moistures are selected. To form network B, for each soil type, we considered the same number of soil moisture measurement points; the same number used for network A, and for each soil type different values of soil moistures are selected. The watershed authority has created soil moisture measurement network in the watershed and is known as Vitel. The network is composted of stations: 111, 133, 134, 136, 144, 146, 149, 154, 159, 162, Berg, and NOAA. Stations 111 and Berg are outside the watershed. Furthermore, we aim to test the suitability of Vitel network for reproducing the spatial soil moisture patterns. Note that network B also includes Vitel stations inside the watershed. The spatial locations of network A, network B, and Vitel are shown in figure 6.9.

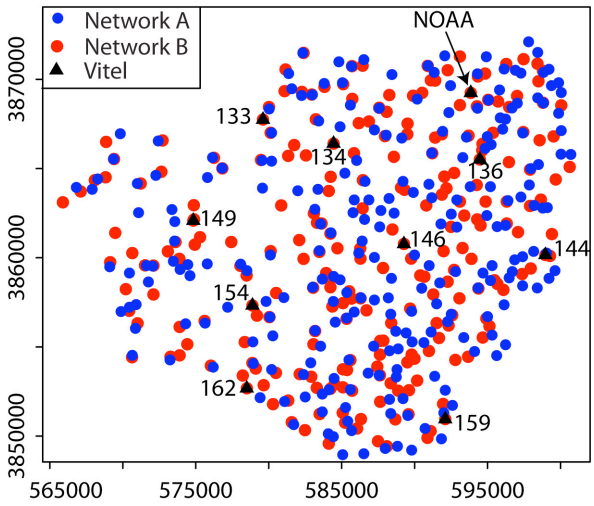

Figure 6.9: Locations of soil moisture measurement points for: network A, network B, and Vitel. Network B also includes Vitel network. Vitel network compose of stations: 111, 133, 134, 136, 144, 146, 149, 154, 159, 162, Berg, and NOAA. Stations 111 and Berg are outside the watershed.

In order to reproduce the spatial soil moisture patterns, it is important that the soil moisture variograms of the soil moisture measurement networks are similar to the variogram of the simulated soil moisture map (input). Furthermore, the experimental variograms of soil moisture networks should be well fitted with the theoretical models. Figure 6.10 shows the experimental variograms of the soil moisture measurement

networks and the simulated soil moisture map fitted with spherical theoretical models, while the properties of the variograms are shown in table 6.3. Except for Vitel network, all the experimental variograms are reasonably fitted with the theoretical models, and the well-fitted variograms can be used for soil moisture krigings. The variogram of Vitel network is poorly fitted with spherical model, and this is obviously due to the small number of the soil moisture measurement points that forms Vitel network. As the experimental variogram of the Vitel network is poorly fitted with theoretical model, the Vitel network is not used for reproducing the spatial soil moisture patterns. The variability between the elements (sill-nuggets) for both network A and network B are similar to the variability between the elements for the simulated soil moisture map. This indicates that both network A and network B have captured the spatial variability of soil moisture. Therefore, both networks can be used to reproduce the spatial soil moisture patterns using EDKs.

Table 6.3: Properties of variograms of soil moisture and residuals for the simulated soil moisture map, network A, network B, and Vitel network, and the mean of residuals of soil moisture.

Predictor	Nugget	Sill	Range (m)	Mean of residuals of soil moisture [%]
Simulated map (original)	0.0035	0.0055	7244.243	-
240-points (Network A)	0.0041	0.0061	3959.020	-
240-points (Network B)	0.004	0.0061	2706.0	-
Vitel network	0.0032	0.0041	6796	-
Gradient	0.004	0.0062	2633.7	+0.111
Cosine aspect	0.0049	0.0064	12263	-0.017
Gradient and cosine aspect	0.0037	0.0058	2075.7	+0.118
All predictors except river network, hydraulic conductivity, and coordinates	0.003	0.0055	1417.6	-0.067

For the simulated soil moisture map, network A, network B, and Vitel network, the variograms are for soil moistures, while for others, the variograms are for residuals. The mean of residuals of soil moisture is obtained from kriging cross validation.

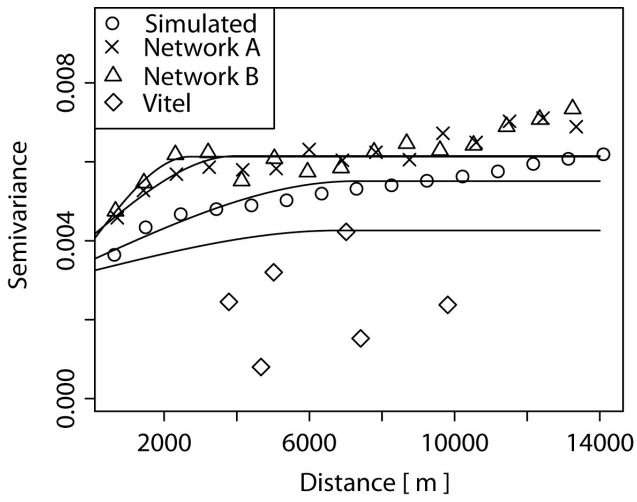

Figure 6.10: Experimental variograms of soil moisture for simulated soil moisture map, network A (network illustrated in section 6.1 and Fig. 6.1), network B (shown in Fig. 6.9), and Vitel network (shown in Fig. 6.9) fitted with spherical models.

For network A, results show that when using gradient, cosine aspect, combination of gradient and cosine aspect, and all predictors except river network, hydraulic conductivity, and coordinates as predictors for EDK have clearly showed the spatial soil moisture patterns (see section 6.2.2). So in this section, the above-mentioned predictors are used as predictors for EDKs and using network B to reproduce the spatial soil moisture patterns. Figure 6.11 shows the simulated soil moisture map in comparison to the kriged soil moistures obtained using soil moisture network B. Results shows that all the kriged soil moisture maps are somehow similar to the simulated soil moisture (input), and all the kriged soil moisture patterns are very similar to their corresponding patterns shown in figure 6.5. The properties of the variograms of the residuals obtained from EDKs that are used for reproducing the spatial soil moisture patterns (Fig. 6.11) are also shown in table 6.3. Table 6.3 also shows the mean of residuals of soil moisture as obtained from kriging cross validation. Values around zero of the mean of the residuals indicate that the kriging estimates are unbiased. The properties of the variograms of residuals for network B are very similar to their corresponding values

obtained for network A except for the soil moisture range obtained using cosine aspect as predictor for EDK.

Figure 6.12 shows the frequency distribution of soil moisture for the simulated soil moisture map, network A, network B, and kriged soil moistures using gradient, cosine aspect, combination of gradient and cosine aspect, and all predictors except river network, hydraulic conductivity, and coordinates as predictors for EDK. The frequency distributions of the simulated soil moisture map, network A, and network B somehow showed to have bimodal distributions, while the frequency distributions obtained using all EDKs showed to have normal distributions. The frequency distributions obtained in this section (see Fig. 6.12) are very similar to their corresponding frequency distributions obtained using network A (see Fig. 6.8). This indicates the robustness of the approach used for characterizing the spatial soil moisture patterns. Furthermore, we compared the main quantiles of soil moistures for the simulated soil moisture map, network A, network B, and kriged soil moistures. Figure 6.13 shows the main quantiles of soil moisture for the simulated soil moisture map, network A, and network B. While figure 6.14 shows the main quantiles of soil moisture for network B and kriged soil moistures obtained using gradient, cosine aspect, combination of gradient and cosine aspect, and all predictors except river network, hydraulic conductivity, and coordinates as predictors for EDK. Figure 6.13 shows the representativeness of both network A and network B to the simulated soil moisture map. As shown in figure 6.14, it is interesting to note that all krigings are well reproducing average soil moisture, and the differences between the simulated and kriged soil moistures increase monotonically as the soil moisture level drop or rise from the average soil moisture. This indicates that krigings should be used with cautions when dealing with extremes; both low and high.

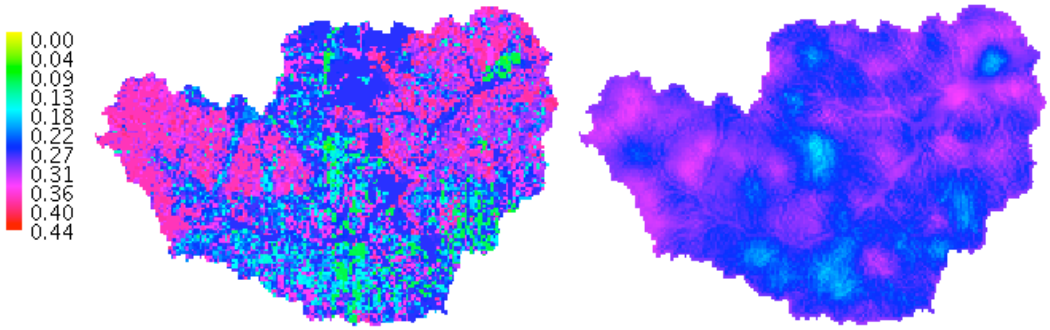

a) Simulated soil moisture

b) Gradient

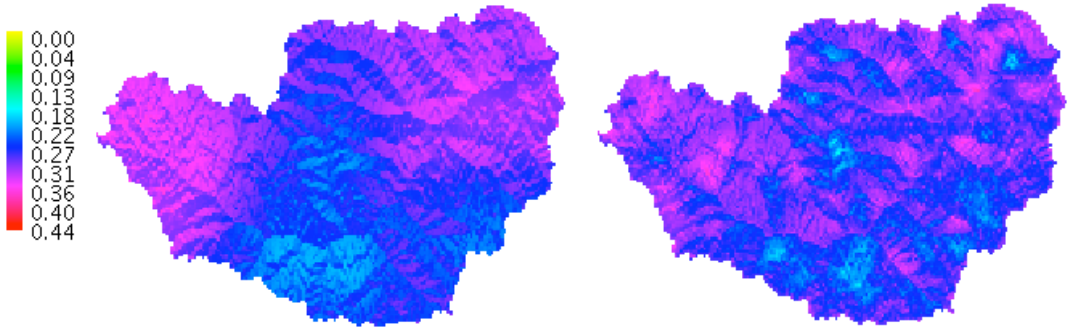

c) Cosine aspect

d) Combination of gradient and cosine aspect

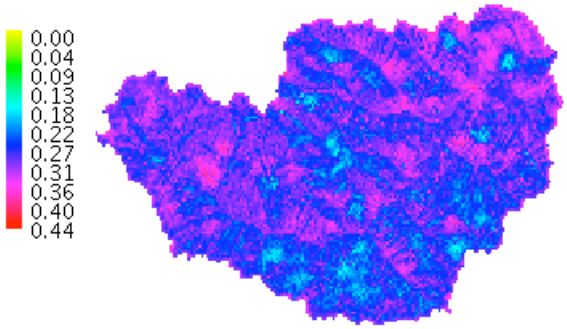

e) All predictors except river network, hydraulic conductivity, and coordinates

Figure 6.11: Simulated and kriged soil moistures for EDKs obtained using soil moisture network B.

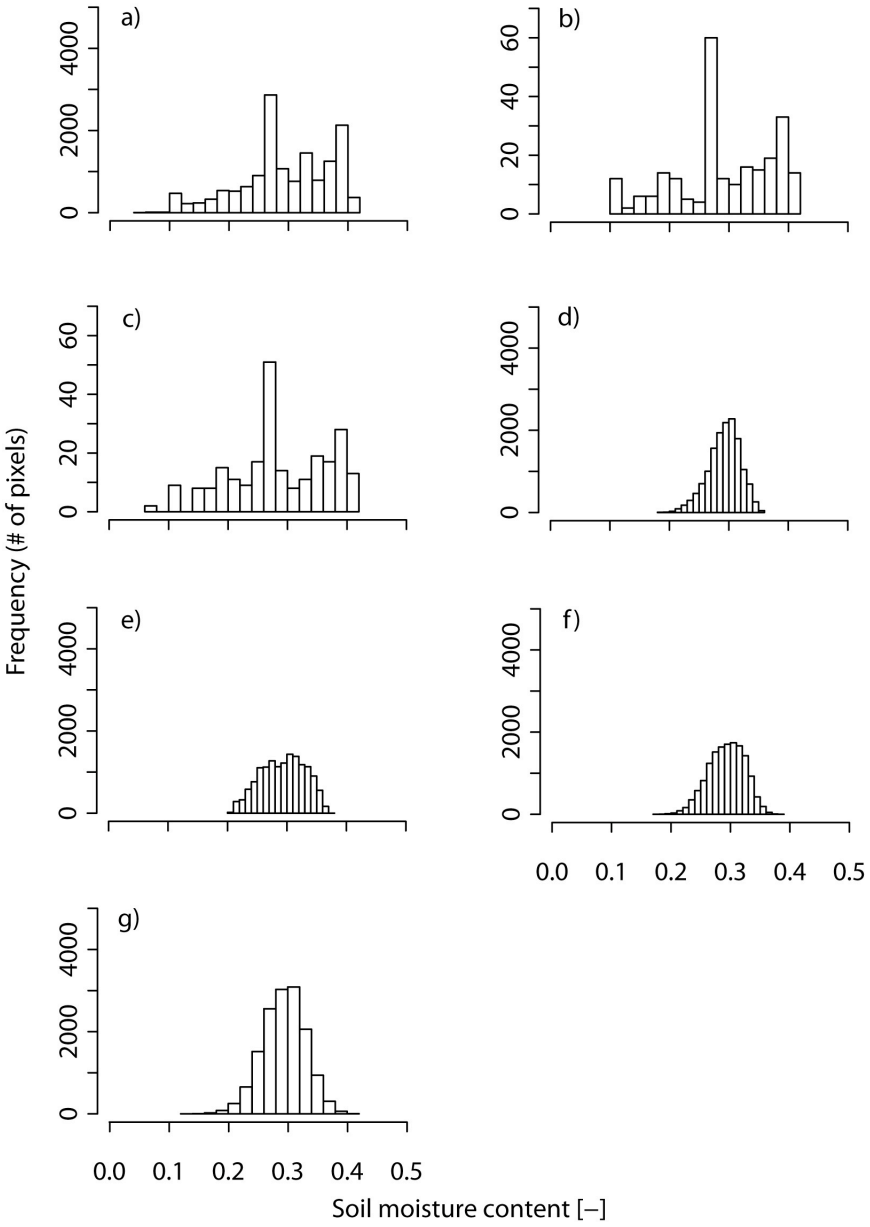

Figure 6.12: Soil moisture frequency distributions of the top 5cm soil layer for: a) Simulated soil moisture, b) 240-points of soil moisture network A, c) 240-points of soil moisture network B, d) Gradient, e) Cosine aspect, f) Combination of gradient and cosine aspect, h) All predictors except river network, hydraulic conductivity, and coordinates.

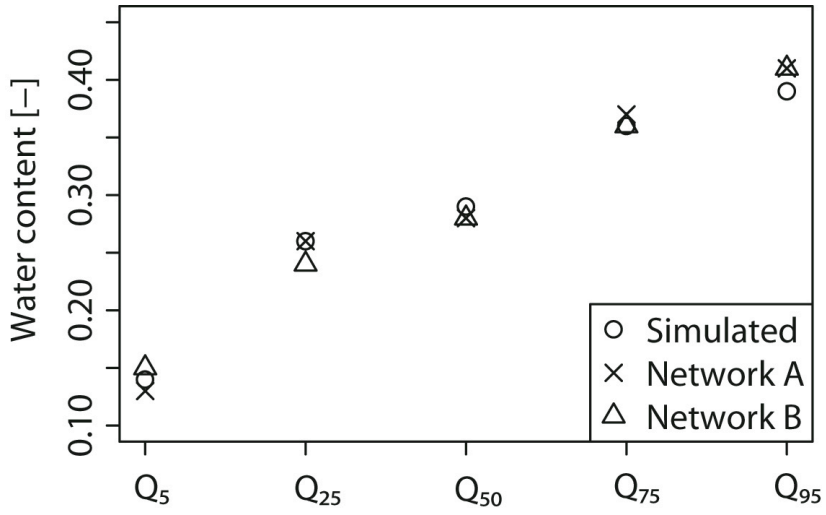

Figure 6.13: Main quantiles of soil moisture for simulated soil moisture map, 240-points of network A, and 240-points of network B.

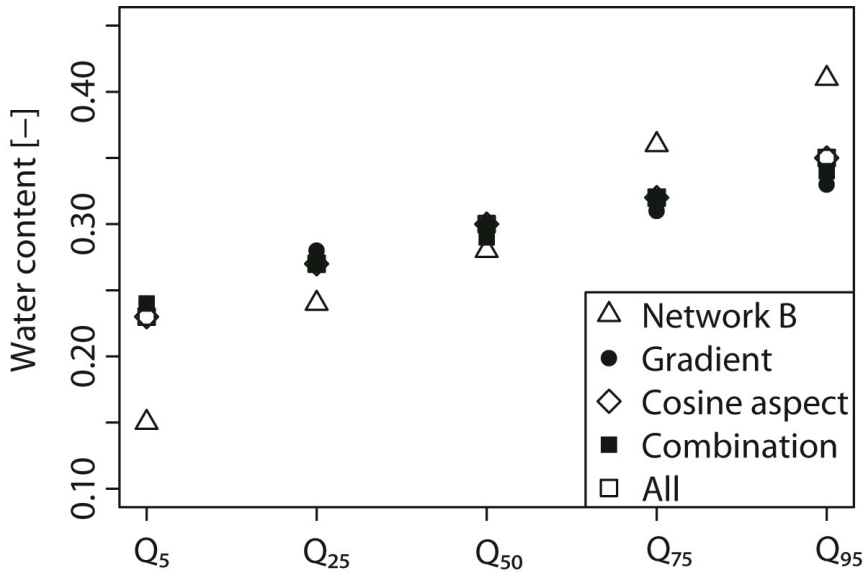

Figure 6.14: Main quantiles of soil moisture for 240-points of network B and kriged soil moistures obtained using gradient, cosine aspect, combination of gradient and cosine aspect, and all predictors except river network, hydraulic conductivity, and coordinates as predictors for EDK. In the legend combination refers to the combination of gradient and cosine aspect, while all refers to all predictors except river network, hydraulic conductivity, and coordinates.

6.4 Spatial soil moisture using defined neighbourhood

In the previous sections all the measurement points are used for kriging interpolations. Looking at the simulated soil moisture map it is evident that we have very fine soil moisture patterns, and it might not be appropriate to use all the measurement points in the interpolation. It might be appropriate to use only the closest measurement points in kriging interpolations. In this section, we used the closest 40 measurement points in kriging interpolation and using soil moisture network B. We chose the closest 40 pints in kriging interpolation because it gives reasonable estimates of spatial soil moisture patterns, using less than 40 points often gives unrealistic values (negative) of soil moistures. The spatial soil moisture patterns obtained using OK and EDKs using different predictors are shown in figure 6.15, while the frequency distributions of simulated and kriged soil moistures are shown in figure 6.16. It is evident that when using all predictors except hydraulics conductivity, coordinates and river network for EDK produces soil moisture patterns that are more close to the simulated patterns (input). Using combination of gradient and cosine aspect as a predictor for EDK also shows the patterns. OK and EDK that uses coordinates as predictor produce smoothed patterns. Using other univariate predictors for EDK somehow show the patterns. We observe that the patterns reproduced by krigings using the closest 40 measurement points in the interpolation are slightly better that the patterns reproduced by krigings when all the measurement points are used in interpolations by krigings. Nevertheless, the results obtained using the closest 40 points in kriging interpolations are similar to the results obtained using all the measurements in the interpolations. The frequency distributions obtained using cosine aspect and river network as predictors for EDK showed to have bimodal distributions, similar to the frequency distribution of the simulated soil moisture map, while the frequency distributions obtained for all other krigings showed to have normal distributions. Only the frequency distributions obtained using longitudinal curvature and all predictors except hydraulic conductivity, coordinates and river network for EDK have soil moisture class lower than 0.1. On the other hand, only the frequency distributions obtained using wetness index, longitudinal curvature, coordinates, and all predictors except hydraulic conductivity, coordinates and river network for EDK have soil moisture class higher than 0.4. In general, we observe that the frequency distributions obtained using all the measurement points in kriging

interpolations are more close to the normal distribution than the frequency distributions obtained using the closest 40 measurement points in kriging interpolations.

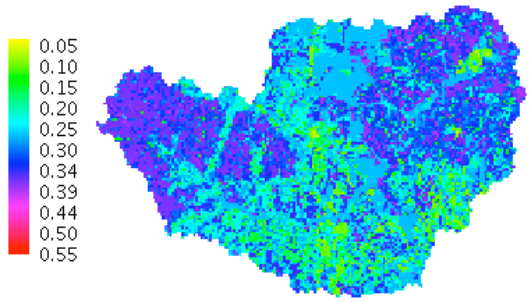

a) Simulated map

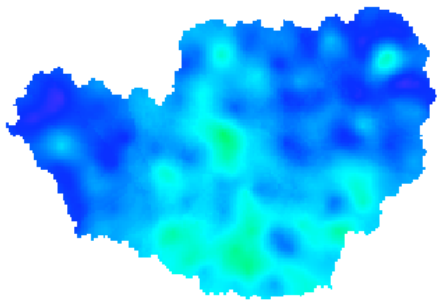

b) OK

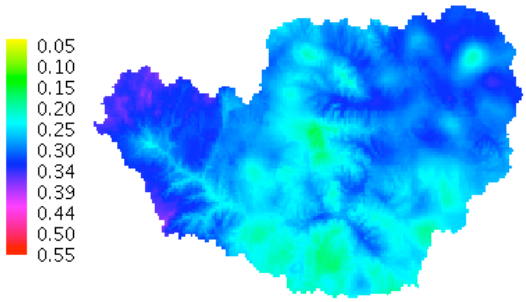

c) Elevations

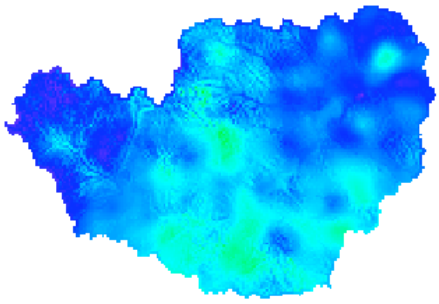

d) Gradient

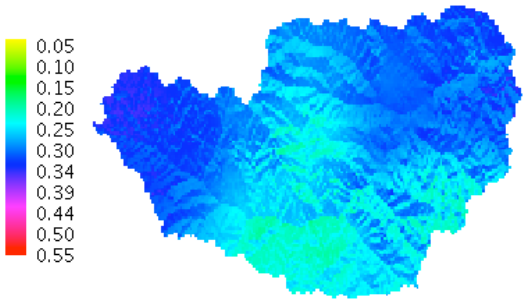

e) Cosine aspect

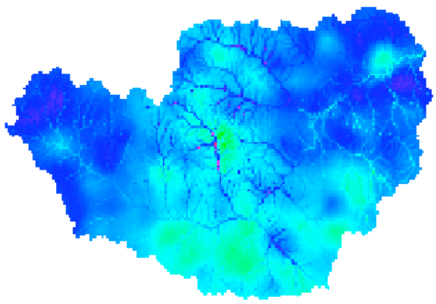

f) Wetness index

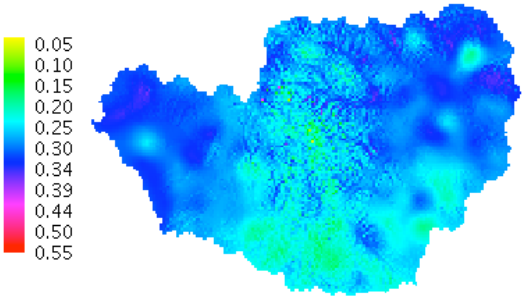

g) Longitudinal curvature

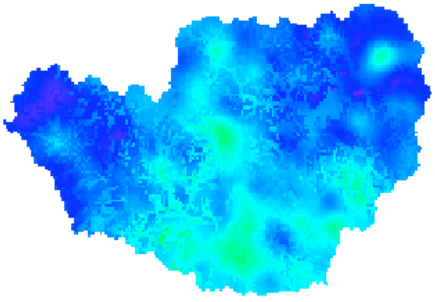

h) Soil depth

Figure continues in the next page

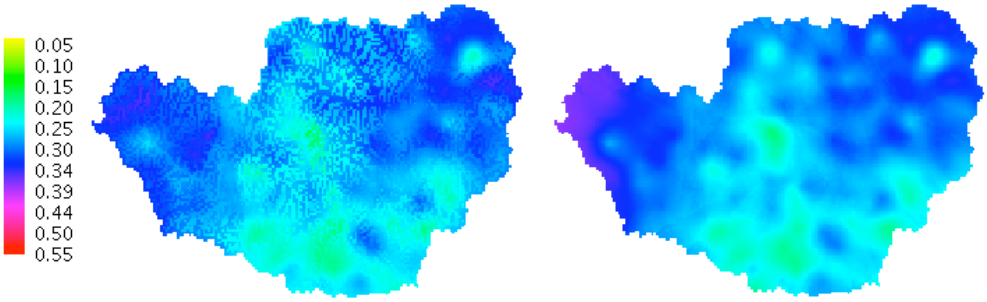

i) Laplacian

j) Coordinates

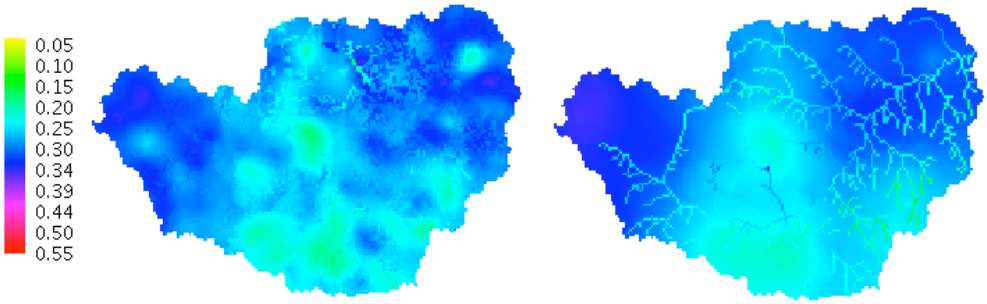

k) Hydraulic conductivity

l) River network

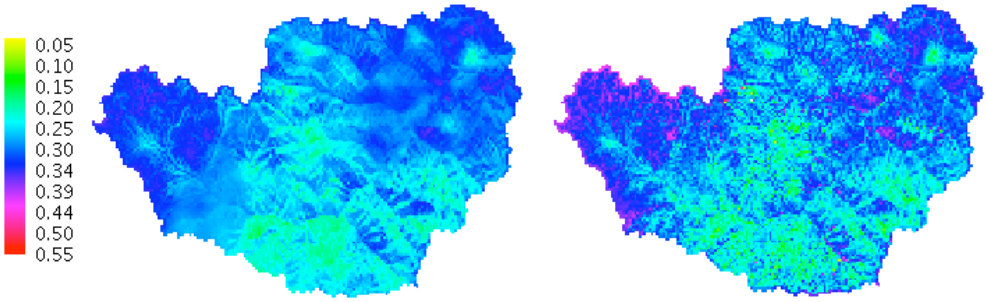

m) Combination of gradient and cosine aspect

n) All predictors except river network, hydraulic conductivity and coordinates

Figure 6.15: Simulated and kriged soil moistures for OK and EDK using different predictors. Kriged soil moistures are obtained using 40 nearest measurement points.

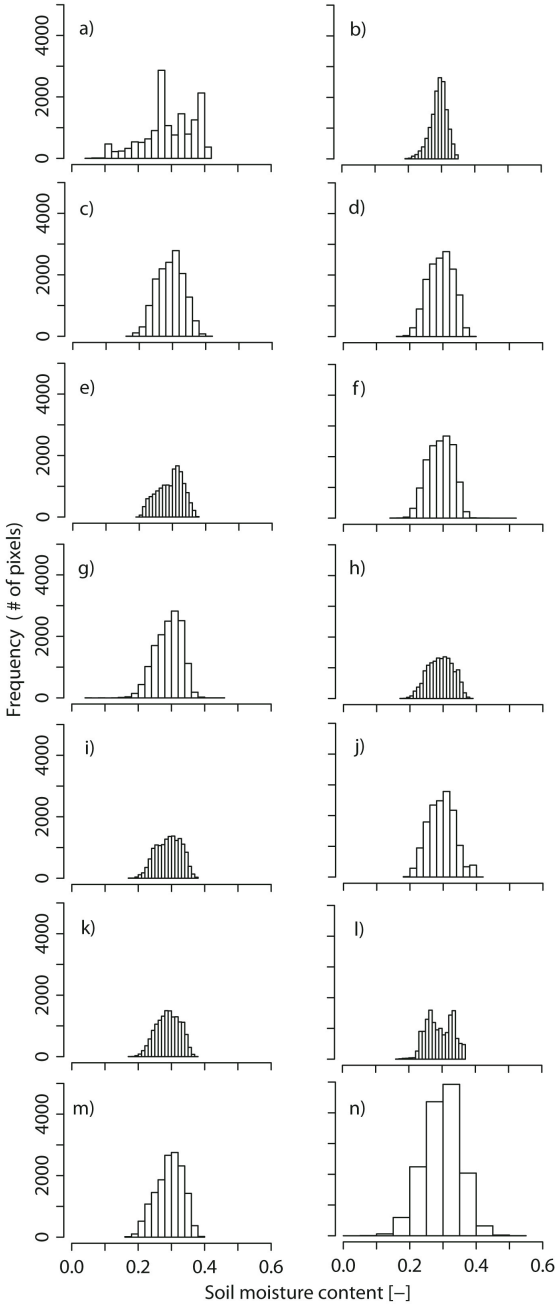

Figure 6.16: Soil moisture frequency distributions of the top 5cm soil layer for: a) Simulated soil moisture, b) OK, c) Elevations, d) Gradient, e) Cosine aspect, f) Wetness index, g) Longitudinal curvature, h) Soil depth, i) Laplacian, j) UK, k) Hydraulic conductivity, l) River network, m) Combination of gradient and cosine aspect, and n) All predictors except river network, hydraulic conductivity, and coordinates.

6.5 Conditional Gaussian simulations

The purpose of this section is to use conditional Gaussian simulations (CGSs) to reproduce the spatial soil moisture patterns. CGSs are performed using the closest 40 measurement points and using soil moisture network B. Furthermore, CGSs are performed using the predictors that are used for EDKs as secondary data. Figure 6.17 shows the spatial soil moisture patterns obtained using CGSs including and excluding secondary data in the simulations and in comparison to GEOtop simulated soil moisture map (input), while figure 6.18 shows the frequency distributions of soil moisture maps of figure 6.17. Figure 6.17 shows that when using gradient as secondary data to CGSs produces spatial soil moisture patterns that are more close to the actual patterns. Using secondary data from only one source (e.g., cosine aspect) to the CGSs also somehow show soil moisture patterns (figures 6.17c – 6.17l). In addition, performing CGSs without considering any secondary data (figure 6.17b) also somehow show the patterns. When using secondary data from two sources to the CGSs (figure 6.17m) produce spatial soil moisture patterns worse than the patterns reproduced without including secondary data or including secondary data from one source to the CGSs. On the other hand, when secondary data from multi sources are used in the CGSs, produce the worst soil moisture patterns (figure 6.17n). Therefore, we conclude that the more the secondary data sources are incorporated in CGSs, the worse the reproduced the patterns. Therefore, care should be taken when incorporating secondary data in CGSs. In general, all CGSs reproduce spatial soil moisture patterns better than the soil moisture patterns reproduced by kriging algorithms.

Figure 6.18 shows that all CGSs produce bimodals soil moisture frequency distributions, similar to the frequency distribution of GEOtop simulated soil moisture map. This is due to the fact that in CGSs the data (input) is first transformed into normal score, then the CGSs are performed on the transformed data, and finally simulated normal scores are back-transformed into simulated soil moisture patterns (e.g., Goovaerts 1997). In the previous sections we show that kriging algorithms are poorly reproducing soil moisture frequency distribution of the input. In this section we show that all CGSs are well reproducing soil moisture frequency distribution of the input. As the soil moisture patterns reproduced by CGSs are much better than the soil moisture patterns reproduced by kriging algorithms, this indicates that reproducing the frequency

distribution of the input is necessary to reproduce the actual spatial soil moisture patterns.

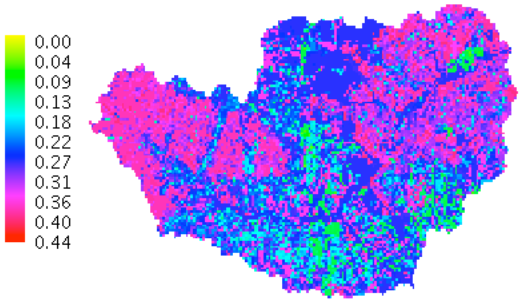

a) GEOtop simulated map

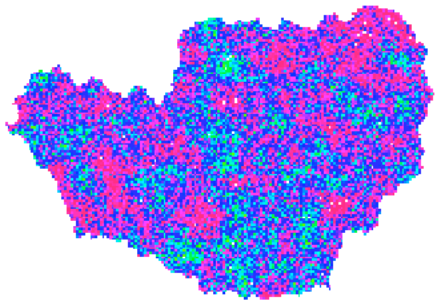

b) No secondary data

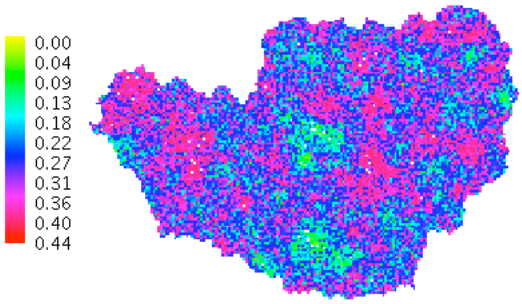

c) Elevations

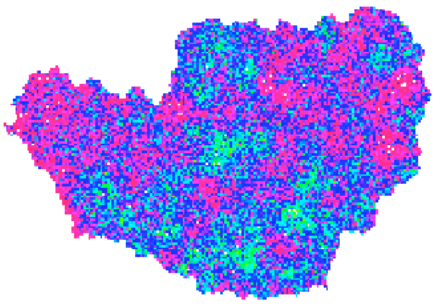

d) Gradient

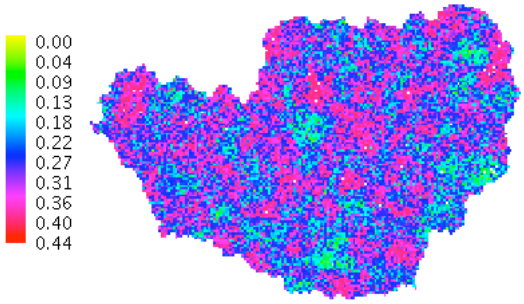

e) Cosine aspect

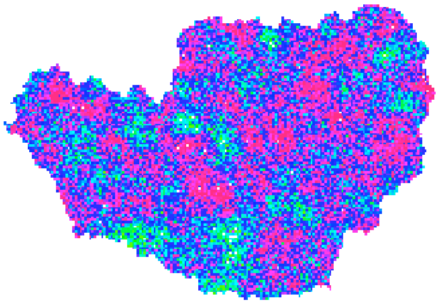

f) Wetness index

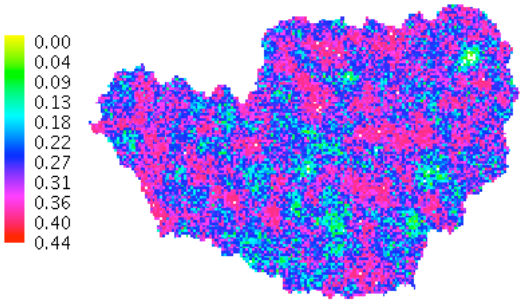

g) Longitudinal curvature

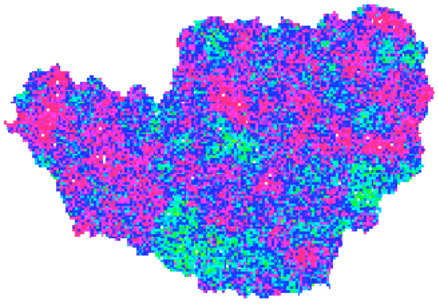

h) Soil depth

Figure continues in the next page

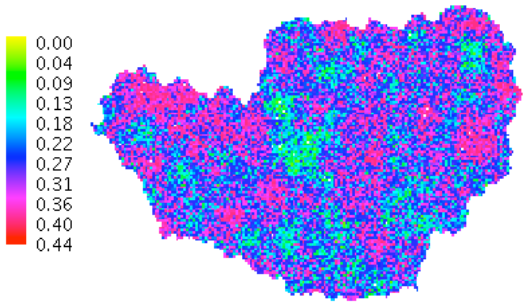

i) Laplacian

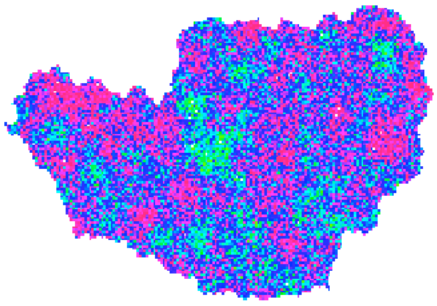

j) Coordinates

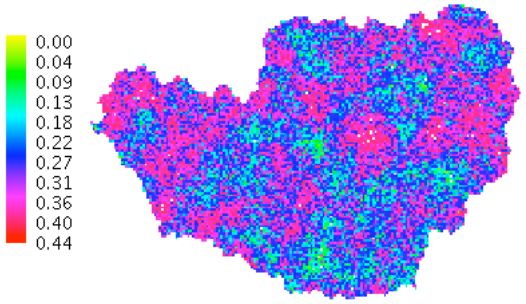

k) Hydraulic conductivity

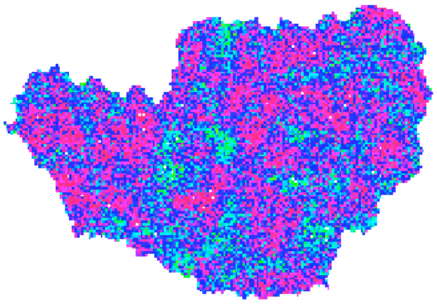

l) River network

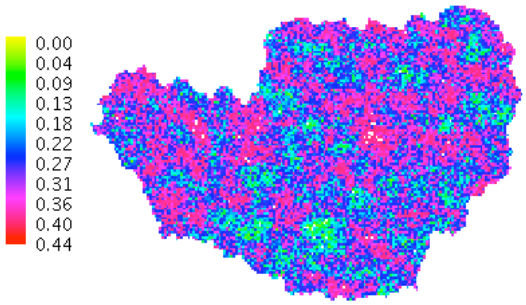

m) Combination of gradient and cosine aspect

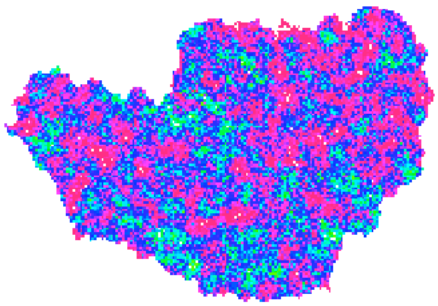

n) All predictors except river network, hydraulic conductivity and coordinates

Figure 6.17: Soil moisture maps obtained using conditional Gaussian simulations and in comparison to the simulated soil moisture map (input).

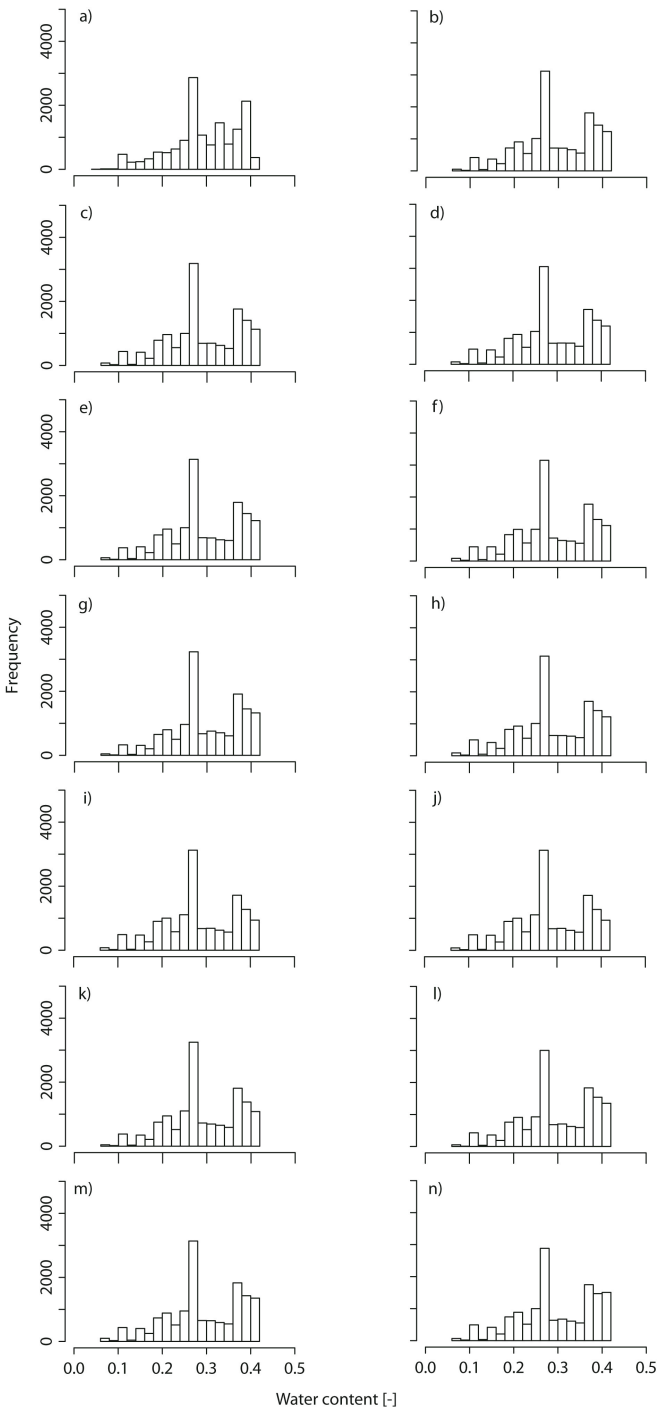

Figure 6.18: Frequency distribution of the top 5cm soil layer obtained using conditional Gaussian simulations in comparison to the simulated soil moistures: a) Simulated soil moisture, b) No secondary data is used, c) Elevations, d) Gradient, e) Cosine aspect, f) Wetness index, g) Longitudinal curvature, h) Soil depth, i) Laplacian, j) Coordinates, k) River network, l) Hydraulic conductivity, m) Combination of gradient and cosine aspect, n) All predictors except coordinates, river network and hydraulic conductivity.

6.6 Conclusion

Soil moisture patterns are studied using OK, and external drift indicator kriging (EDIK). The soil type is used as indicator for krigings, while the following indices: DEM, gradient, cosine aspect, wetness index, longitudinal curvature, soil depth, laplacian, coordinates, river network, hydraulic conductivity, and their combinations are used as drifts (predictors) for EDIK. Furthermore, CGSs are used to reproduce soil moisture patterns.

Analysis of directional variogram of soil moisture shows that there is no anisotropy. Results show that all krigings reproduced unbiased soil moisture estimates. Although all krigings reproduced unbiased soil moisture estimates, OK, and UK reproduced very smoothed patterns and are very different from the actual patterns. The patterns reproduced using DEM, wetness index, soil depth, river network, hydraulic conductivity, and laplacian as predictors for EDIK, are similar to the patterns reproduced by the OK and UK. While using gradient and cosine aspect as predictors for EDIK have clearly showed the patterns. The combination of all predictors except river network, hydraulic conductivity, and coordinates for EDIK, reproduced the closest patterns to the actual patterns. The frequency distribution and the variogram of soil moisture of the selected 240 points are very similar to the frequency distribution and the variogram of the simulated soil moisture map, respectively. The frequency distribution of the simulated soil moisture somehow showed to have bimodal distribution, while the frequency distributions obtained using all kriging algorithms showed to have normal distributions. Result shows that the closer the frequency distribution to the simulated frequency distribution, the better the reproduced the soil moisture patterns. Nevertheless, none of the above krigings is able to capture the extreme values of soil moisture. The residual soil moisture maps, as obtained from kriging cross validation, and the frequency distributions of soil moisture show that the 240-soil moisture measurement points are reasonably enough to establish permanent soil moisture network in the watershed. On the other hand, CGSs show that when using gradient as secondary data, reproduced the best patterns (similar to the actual patterns). In general, all CGSs clearly show the spatial soil moisture patterns and all CGSs reproduce soil moisture histogram of the input. Therefore, CGSs are preferred than krigings in studying spatial patterns.

7 Utility of remotely-sensed precipitation products for hydrological simulations

In this chapter, we investigated the utility of remotely sensed rainfall products (Climate Prediction Center's MORPHing technique (CMORPH), Precipitation Estimation from Remotely Sensed Information using Artificial Neural Networks - Cloud Classification System (PERSIANN-CCS), and Next Generation Weather Radar (NEXRAD) stage III) for hydrological simulations at basin scale in the Little Washita (583 km^2) watershed, Oklahoma, USA. The distributed hydrological model, GEOtop (Rigon et al. 2006) is used to simulate the streamflows. We simulated the streamflows for the years 2003 and 2007, for which we have complete measurements, including remotely-sensed precipitation, raingauge, and streamflow data. Results show that, in general, all remotely-sensed precipitation products have value for streamflow simulations.

7.1 Remotely-sensed precipitation products

The National Weather Service Next Generation Weather Radar (NEXRAD) precipitation is considered as an important and reliable source of ground-based precipitation in USA. The spatial and temporal scales of NEXRAD are 4km and 1hour, respectively. NEXRAD Stage III version is the most important precipitation product. In Stage I, precipitation is estimated by finding the relationship between radar-measured reflectivity (Z) and precipitation rate (R). Stage II, multiple raingauges observations are used for bias adjustment. Stage III is mosaicking of Stage II products using multiple radars.

Satellite precipitation is estimated using visible (VIS) and infrared (IR) spectral bands of Geostationary Earth Orbiting (GEO) satellites and microwave (MW) spectral bands from Low Earth Orbiting (LEO) satellites. MW sensors on LEO are accurately estimating precipitation, but at the cost of limited sampling, while IR sensors on GEO are less accurate for estimating precipitation, but with high sampling frequency. Satellite precipitation products combine the MW and IR to take the advantage of complementary strengths.

CMORPH (Joyce et al. 2004) estimates precipitation using the most accurate, but not frequent passive microwave (PMW) data and the less accurate but more frequent IR data. IR data are used only to derive cloud motion field that is subsequently used to propagate raining pixels. CMORPH products are available every 30 minutes at 0.0727^0 latitude and longitude (8km at the equator) grid resolution.

Precipitation Estimation from Remotely Sensed Information using Artificial Neural Network-Cloud Classification System (PERSIANN-CCS) uses artificial neural network to derive relationship between IR and PMW data for the IR data to estimate precipitation.

7.2 Setup of simulations

GEOtop model (Rigon et al. 2006) is used for streamflow simulations. All the calibration parameters obtained during the SGP97 for the GEOtop model were kept fixed for the streamflow simulations for the years 2003 and 2007 except the initial temperatures, initial water contents, and the coefficient of the uniform of the motion of the surface to account for possible landuse changes are modified. Simulated streamflows for both years are continuous simulations. Streamflow simulations for years 2004, 05 and 06 were not carried out because there are only one or two significant measured streamflow events.

For 2003, the streamflows are simulated using precipitation data from: raingauge, CMORPH (Joyce et al. 2004), PERSIANN-CCS (Hsu et al. 1997), NEXRAD Stage III (e.g., Fulton et al. 2007), and bias-adjusted CMORPH. Precipitation data from 45 raingauges (meteorological stations) along with other measured meteorological forcing data (i.e., air temperature, relative humidity, solar radiation, air pressure, wind speed and wind direction) are used for raingauges streamflow simulations in the watershed (Fig. 1.1). As the meteorological forcing are given as point measurements to the GEOtop model, the values of precipitation estimated by NEXRAD, CMORPH, and PERSIANN-CCS are extracted at these 45 meteorological stations (same stations used for raingauges) and they used along with other measured meteorological forcing data for GEOtop streamflow simulations. In GEOtop model, point precipitation data are spatially distributed using either krigings or MicroMet (Liston and Elder 2006). In this chapter, point precipitation data are spatially distributed using kriging algorithm.

For 2007, the streamflows are simulated using raingauge and CMORPH precipitations. Precipitation data from 17 raingauges are used for raingauge simulations (Fig. 7.1), along with other measured meteorological forcing data. The CMORPH precipitation data are extracted from the CMORPH precipitation grids at the same locations of the 17 raingauges, and then the extracted precipitation data are used for the streamflow simulations, along with other measured meteorological forcing data at these 17 meteorological stations. Only storms that produce streamflows greater than $15m^3/s$ are selected. Figure 7.1 shows the raingauge network and the CMORPH precipitation grids over the Little Washita watershed.

The temporal resolution of all precipitation products that are used for forcing the GEOtop model is 1 hour. The spatial resolution of CMORPH is 8km, while the spatial resolutions of PERSIANN-CCS and NEXRAD are 4km. For more details about model initialization and simulation setup, please see section 2.3.

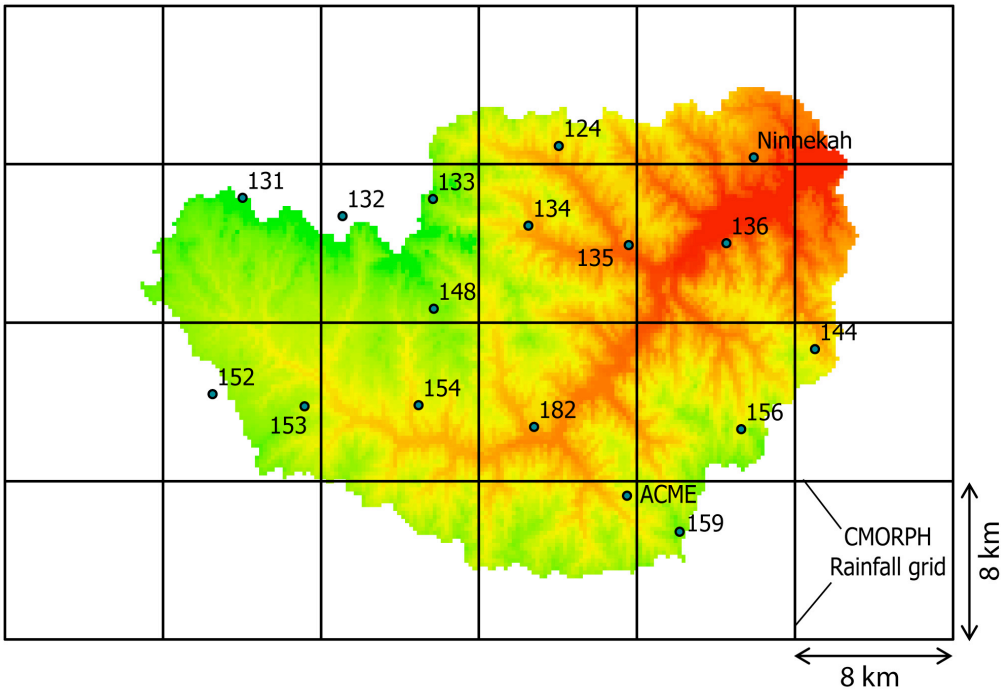

Figure 7.1: Raingauge network and CMORPH grids that are used for the 2007 simulations.

7.3 Performance statistics

7.3.1 Bias ratio and root mean square error

We used bias ratio and the root mean square error (RMSE) to evaluated the performance of the model. The bias ratio for the simulated streamflows is calculated as follows:

$$Bias\ ratio = \frac{simulated}{observed} \tag{7.1}$$

While the RMSE of the simulated streamflows is calculated as follows:

$$RMSE = \sqrt{\frac{1}{n}\sum_{i}^{i=n}\left(Q_i^{obs} - Q_i^{sim}\right)^2} \tag{7.2}$$

Where n is the number of discharge values, Q is the runoff discharge, and superscrips *obs* and *sim* are for observed and simulated, respectively.

7.3.2 Error in peaks

This statistic performance criterion is applied only to the 2007 simulations. Quantitative performance statistics for each peak is performed. For each peak, the peak magnitudes are compared to the measured peaks, error in peaks for both raingauge and CMORPH simulations are calculated, and peak flows time lag for both raingauge and CMORPH simulations are also calculated. The error in peaks is calculated using the following relationship:

$$Error\ in\ peaks = \frac{P^{sim} - P^{obs}}{P^{obs}} \tag{7.3}$$

Where P is runoff peak, and superscripts *sim* and *obs* are for simulated and observed, respectively.

7.4 Streamflow simulation for 2003

First, we have calculated total precipitation that falls in the watershed during March 26 - July 6, 1997 as estimated by raingauge, NEXRAD, PERSIANN-CCS, CMORPH, and bias-adjusted CMORPH. The period March 26- July 6, 1997 is selected because we have complete streamflow measurements, and the simulated streamflows obtained using all the above precipitation products will be evaluated at this period. The bias-adjusted CMORPH precipitation is calculated as follows:

$$x_{opt1} = x_1 + w_1[x_2 - x_1] \tag{7.4}$$

$$x_{opt2} = x_2 + w_2[x_1 - x_2] \tag{7.5}$$

$$w_1 = \frac{\sigma_1^2}{[\sigma_1^2 + \sigma_2^2]} \tag{7.6}$$

$$w_2 = \frac{\sigma_2^2}{[\sigma_1^2 + \sigma_2^2]} \tag{7.7}$$

Where x_1 is raingauge precipitation and x_2 is CMORPH precipitation, σ_1, σ_2 are the standard deviations of raingauge and CMORPH precipitations, respectively. For both raingauge and CMORPH precipitation time series the standard deviations are calculated for the whole time series of precipitation. The optimal generated hourly precipitation is the average of x_{opt1} and x_{opt2}.

The total precipitation falls in the watershed during March 26 - July 6, 1997 that is estimated using different precipitation products is shown in figure 7.2. Raingauge and NEXRAD estimated the same amount of precipitation. This is not surprising since in stage II of NEXRAD multiple raingauges observations are used for bias adjustment. PERSIANN-CCS also estimates precipitation similar to raingauges and NEXRAD. On the other hand, CMORPH is highly overestimating precipitation compared to the raingauges, NEXRAD and PERSIANN-CCS. Bias-adjusted CMORPH precipitation is much less than the precipitation estimated by the CMORPH, but it is larger than the precipitation estimated by raingauges, NEXRAD and PERSIANN-CCS. This indicates the robustness of the method used for the bias adjustment of precipitation.

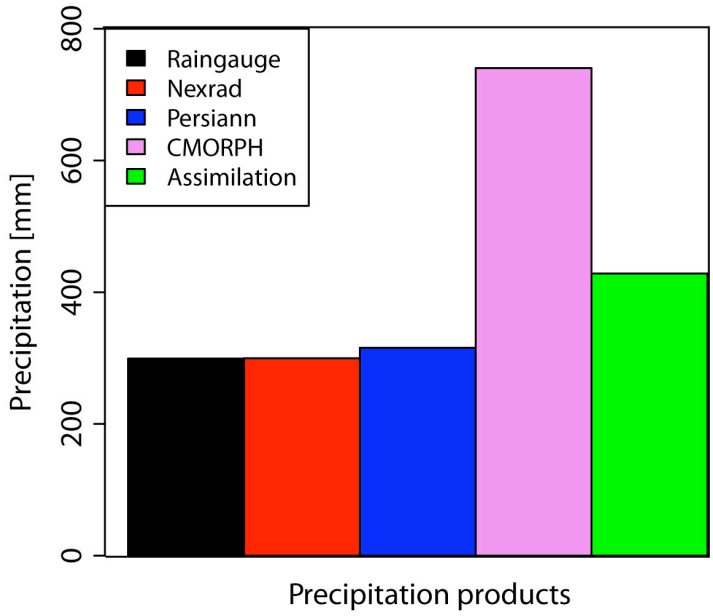

Figure 7.2: Watershed total precipitation for the period March 26 - July 6, 1997 estimated using different precipitation products. Assimilation refers to bias-adjusted CMORPH precipitation.

The streamflows simulated using raingauge precipitation are presented in figure 7.3, in comparison to the measured streamflows. Both measured and simulated streamflows are taken every 15 minutes. Furthermore, the streamflows are simulated using precipitation data from: NEXRAD, CMORPH, PERSIANN-CCS, and bias-adjusted CMORPH. The simulated streamflows obtained using all these products are also shown in figure 7.3, and in comparison to the measured streamflows. The measured and the simulated streamflows are also printed every 15 minutes.

We used bias ratio (equation 7.1) and RMSE (equation 7.2) to evaluate the performance of simulated streamflows obtained using all precipitation products for the period March 26 - July 6, for which we have complete streamflow measurements. The mean bias ratios for the simulated streamflows obtained using precipitation data from raingauge, NEXRAD, PERSIANN-CCS, CMORPH, and bias-adjusted CMORPH are 1.76, 1.65, 1.71, 11.71, and 4.09, respectively, while the calculated RMSEs for the same precipitation products are 2.74, 3.14, 2.33, 10.81, and 5.61, respectively. The raingauge seems reasonably reproducing the streamflows. Nevertheless, raingauge slightly overestimating streamflows, i.e., bias ratio = 1.76, and often there is phase shift between the measrured and the simulated streamflows. NEXRAD performs similar to the raingauge, and it perform slightly better than the raingauge in terms of mean bias ratio,

but worse than raingauge in terms of RMSE. PERSIANN-CCS seems to reasonably reproduce the streamflows. Surprisingly, it performs slightly better than the raingauge in terms of both bias ratio and RMSE, and it performs a bit worse than NEXRAD in terms of mean bias ratio. CMORPH is significantly overestimating streamflows. This is obviously due to the large amount of precipitation estimated by CMORPH (see Fig. 7.2). Bias-adjusted CMORPH is also overestimating the streamflows, but it performs better than the CMORPH and worse than the all other precipitation products, including raingauge that are used for bias-adjustment of CMORPH.

From figure 7.3, it is evident that the streamflows are fairly simulated using precipitation data from all the above-mentioned products except for CMORPH simulation that is significantly overestimating the streamflows for the period from March to June. Also note that except for the simulation of CMORPH precipitation, all products are reasonably reproducing the watershed baseflows. CMORPH streamflow simulations have improved very much when the CMORPH precipitations combined with raingauge precipitations. The mismatch between the measured and the simulated streamflows obtained using all the above-mentioned precipitation products is partly attributed to the operation of flow retarding structures (FRSs) that are used in flood control during precipitation storms (Allen and Naney 1991; Tortorelli and Bergman 1985). In the watershed there are about 42 FRSs (Allen and Naney 1991). The ponds behind these FRSs cover different areas and have different storage capacities. The area varies from about 137ha to 2860ha, and the storage capacity varies from about 0.158 to 2.97 million m^3.

Since the measured streamflow is not continuous throughout the year, the simulated streamflows obtained using all the above-mentioned precipitation products are compared, and shown in figure 7.4. From figure 7.4, it is clear that the streamflow simulations obtained using precipitation products of PERSIANN-CCS, NEXRAD, and bias-adjusted CMORPH produce streamflows very close to the streamflows obtained using raingauges. CMORPH clearly overestimates streamflows during the period from March to June, and it seems that something goes wrong with the CMORPH algorithm during this period; however, after June, CMORPH produces streamflows very close to the streamflows obtained using other precipitation products. Nevertheless, CMORPH often overestimates streamflows after June compared to the streamflows obtained using other precipitation products.

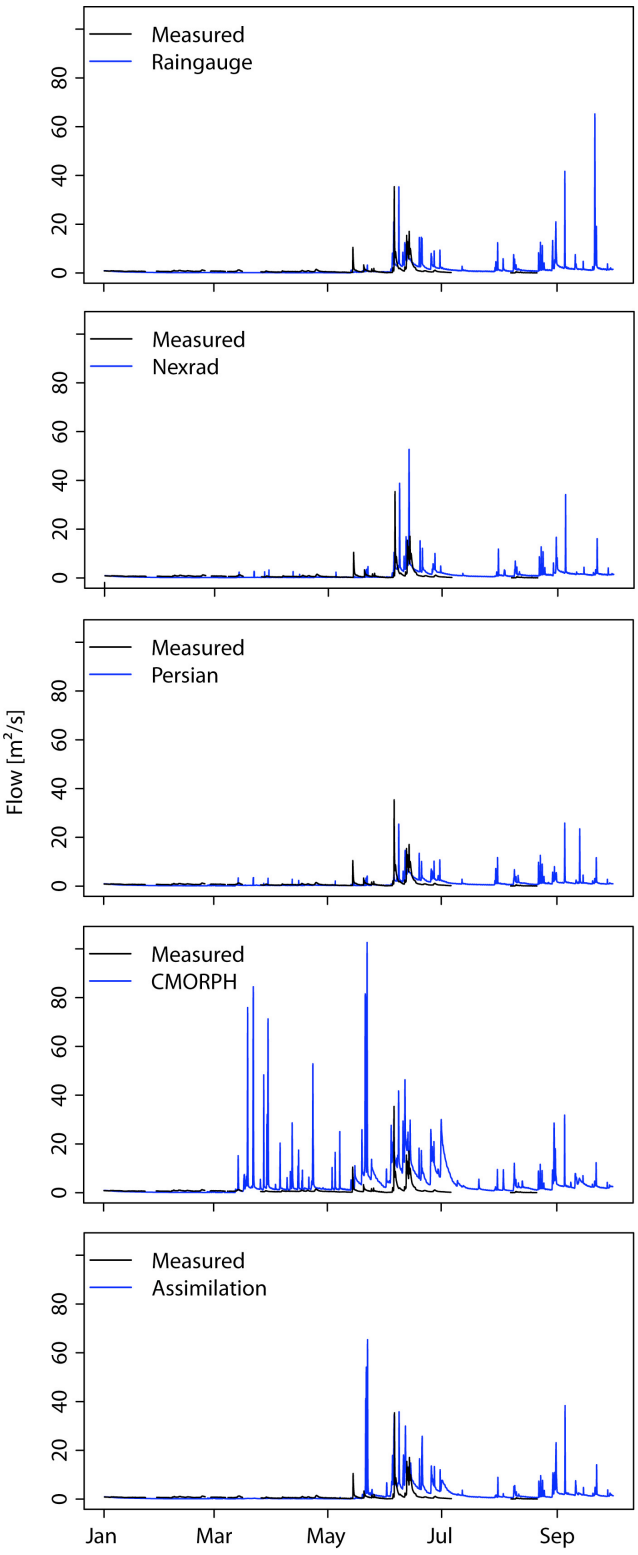

Figure 7.3: Comparison of measured streamflows with the simulated streamflows using precipitation data from: raingauge, NEXRAD, PERSIANN-CCS, CMORPH, and bias-adjusted CMORPH (assimilation), from top to bottom, respectively.

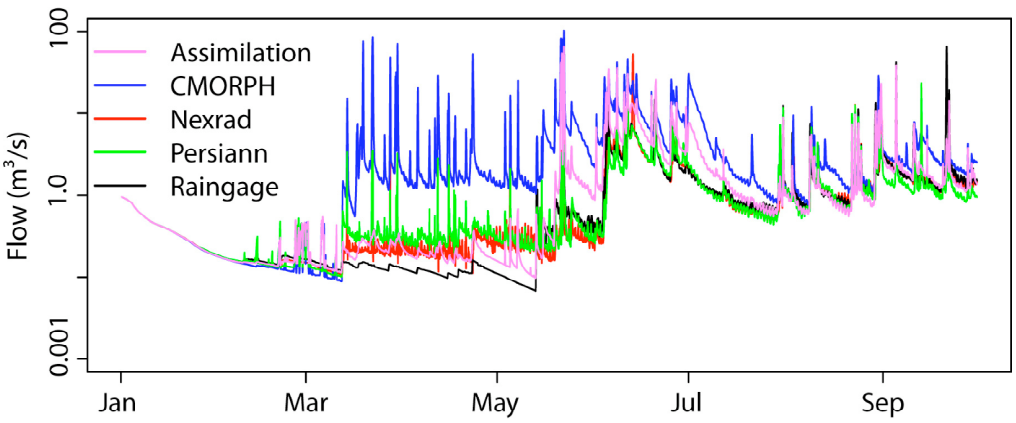

Figure 7.4: Comparison of simulated streamflows obtained using precipitation data from: raingauge, NEXRAD, CMORPH, PERSIANN-CCS, and bias-adjusted CMORPH (assimilation), in semi-log scale.

7.5 Streamflow simulation for 2007

Raingauge and CMORPH precipitations are used to simulate streamflows for warm storms (June - September). Figure 7.5 shows the amount of precipitation [mm] for each of the storms as estimated by Raingauge and CMORPH. For storms 2, 6, and 7, the amount of precipitations estimated by raingagues are higher than that estimated by CMORPH. Only for storm 4, the amount of precipitations estimated by CMORPH is greater than that estimated by raingagues. For other storms, i.e., storms 1, 3, and 5, both CMORPH and raingagues produce similar amount of precipitation.

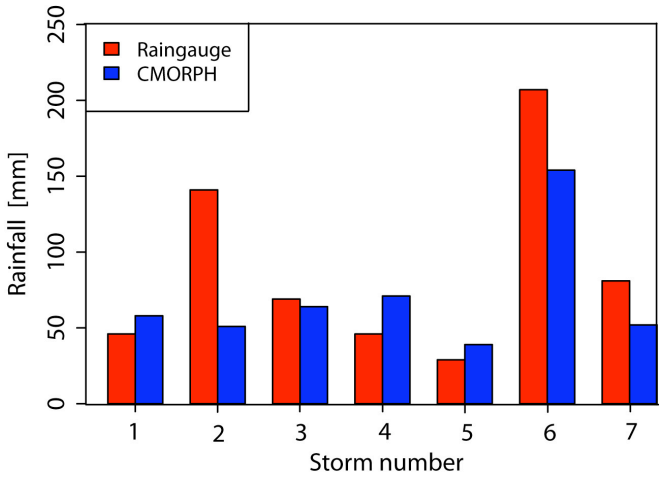

Figure 7.5: Watershed total precipitation for each storm

Figure 7.6 shows the simulated runoff depth for each storm obtained using precipitation data from raingauges and CMORPH in comparison to the measured runoff depth, while figure 7.7 shows the simulated and the measured streamflows for the main storms during the study period. From figure 7.7 it is clear that both raingauge and CMORPH precipitations produce comparable streamflow hydrographs, and both hydrographs, in general, very close to the measured streamflow hydrographs. However, the simulated runoff depth for storms 4 and 6 that are obtained using precipitation data from both raingauge and CMORPH are significantly lower than the measured runoff depth. One possible scenario for this underestimation is that both raingauge and CMORPH underestimate the actual precipitation.

For most of storms, CMORPH produces streamflow hydrographs higher than the streamflow hydrographs produced by raingauge precipitations. As the CMORPH estimates precipitation from clouds, it seems that some water evaporates below the cloud base before reaching the ground surface, resulting on high CMORPH streamflows compared to the raingauge streamflows. Comparing CMORPH simulations in 2003 with the CMORPH simulations in 2007, it is evident that CMORPH simulations in 2007 are pretty good, while they were not so good during the warm period of 2003. Zeweldi and Gebremichael (2008) have evaluated CMORPH precipitation product over the Little Washita watershed using data from 2003 to 2005, and found that CMORPH overestimates precipitation significantly during the warm seasons compared to the NEXRAD Stage III precipitation. It seems that in 2007, CMORPH algorithm has undergone significant improvements. For instance, if there is difference in the amount of precipitation measured by raingauge and CMORPH, but both precipitations are not effective, there would be no difference in streamflows obtained using raingauge and CMORPH precipitations.

In general, all storms are reasonably simulated. In spite of that, we observe that there is mismatch between the measured and the simulated streamflows for storms 2 and 4. The time lag between storm 1 and storm 2 is about 3 days, while the time lag between storm 3 and storm 4 is only few hours. This mismatch between the measured streamflows and the simulated streamflows for storm 2 and storm 4, is most likely due to the operation of flow retarding structures (FRSs) that are use to control floods during storms. Tortorelli and Bergman (1985) reported that the released stored water in ponds that are regulated by FRSs lasts some days after the storms. It seems that the ponding water on the upstream of the FRSs is released while another storm is coming, resulting on earlier

peaks of streamflows, and it seems that the second peak of storm 4 is delayed because of the operation of the FRSs. Tortorelli and Bergman (1985) showed that the FRSs could have significant influence on the shape of the recession part of the hydrographs; depending on whether the ponds (of the FRSs) are spilling or not. Furthermore, they showed that the hydrograph peaks are reduced significantly due to the operation of the FRSs. They also observed composite peak of hydrograph in the watershed due to the operation of these FRSs. We note that the measured hydrograph of storm 7 tend to have composite peak.

Although the GEOtop model is reasonably calibrated and validated using raingauge precipitation data, and although the measured and the simulated streamflows are printed every 15 minutes, CMORPH produces streamflows comparable to both raingauge streamflows and to the measured streamflows. Therefore, it can be concluded that CMORPH products are suitable for streamflow simulations at finer time steps, at least in the study period in the watershed.

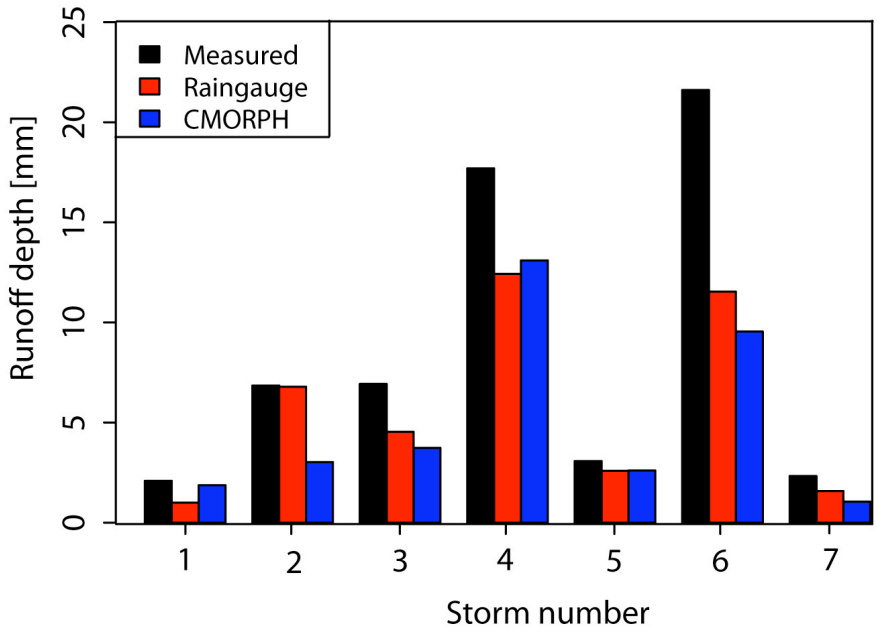

Figure 7.6: Runoff depth for each storm

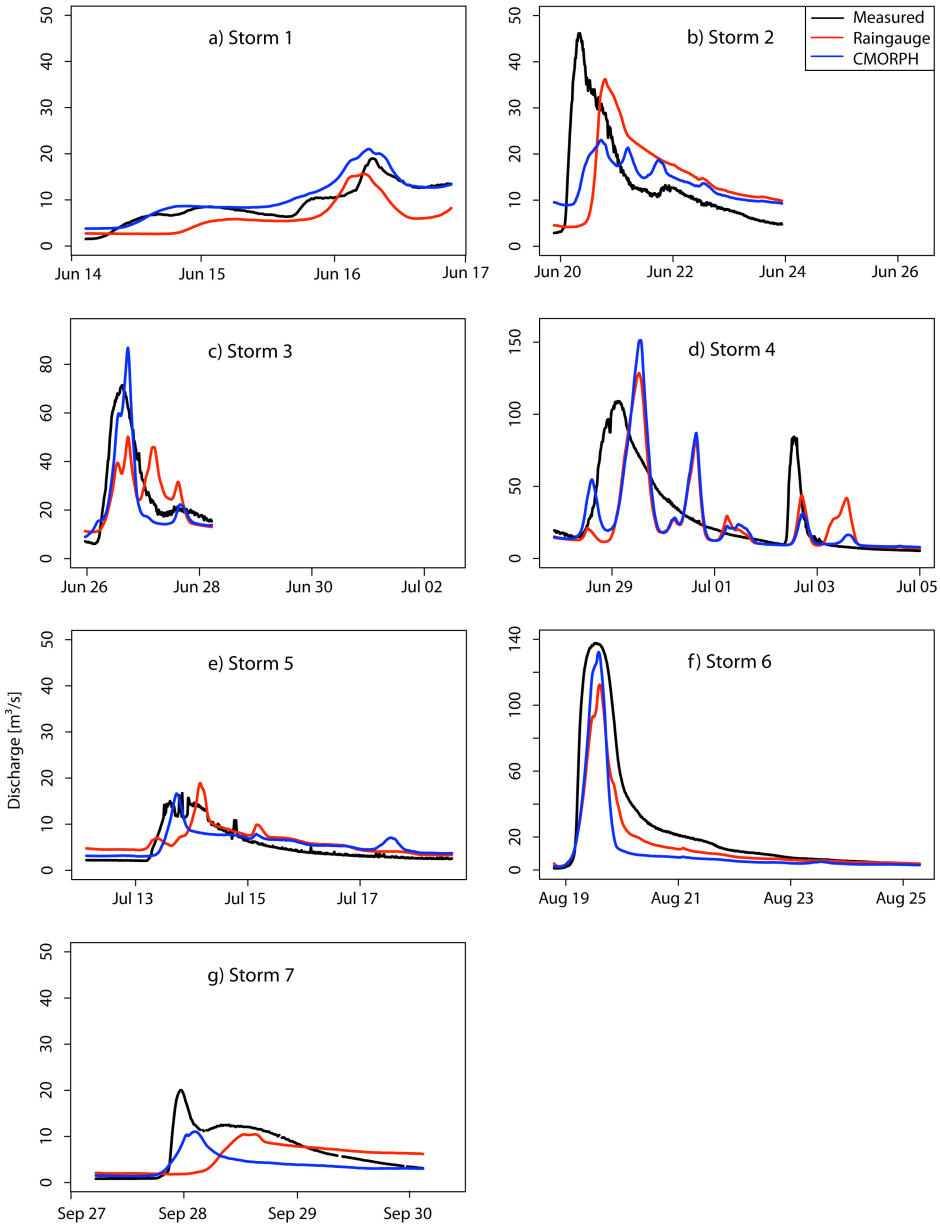

Figure 7.7: Simulated and measured streamflow hydrographs that are greater than 15m^3/s.

Figure 7.8 shows the bias ratio and the RMSE for each storm. Using the bias ratio as an evaluation criterion, both CMORPH and raingauge simulations produce comparable results, except for small storms: storm 1 and storm 7, for which the differences are noticeable.

With regard to the RMSE, also both CMORPH and raingauge simulations are comparable. Nevertheless, CMORPH simulations are slightly better than raingauge simulations; low values of RMSE. The worst simulation is obtained for storm 4; high RMSE for both CMORPH and raingauge simulations, while the best simulation is obtained for storm 1; low RMSE for both CMORPH and raingauge simulations.

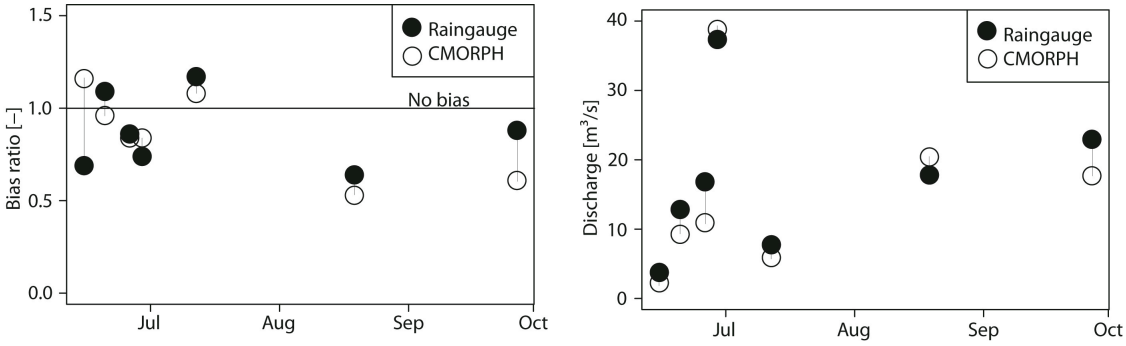

Figure 7.8: Bias ratio (left) and RMSE (right) for each storm.

Figure 7.9 shows the peak magnitudes and the error in peaks, while figure 7.10 shows the peak flow time lag from the measured peak flow. Note that storm 4 has double peak. The peak magnitudes of both CMORPH and raingauge simulations are very close to the measured peaks except for storm 4, and this is more likely due to the operation of the FRSs. Similarly, both raingauge and CMORPH simulations display similar error in peaks. Nevertheless, raingauge simulations seem to underestimate the peaks.

From figure 7.10, it is evident that except for storms 5 and 7 which are very small storms, the peak flow time lags for both CMORPH and raingauge simulations are very similar. Note that the max peak flow time lag is for storm 7 (for raingauge simulations), and it is about half day. In spite of the presence of the FRSs, and despite the fact that the measured and the simulated streamflows are printed every 15 minutes, the max peak flow time lag is about 12 hours (half day). This indicates the suitability of GEOtop

model for flood forecasting on sub-daily time scales at watershed scale using both CMORPH and raingauge data.

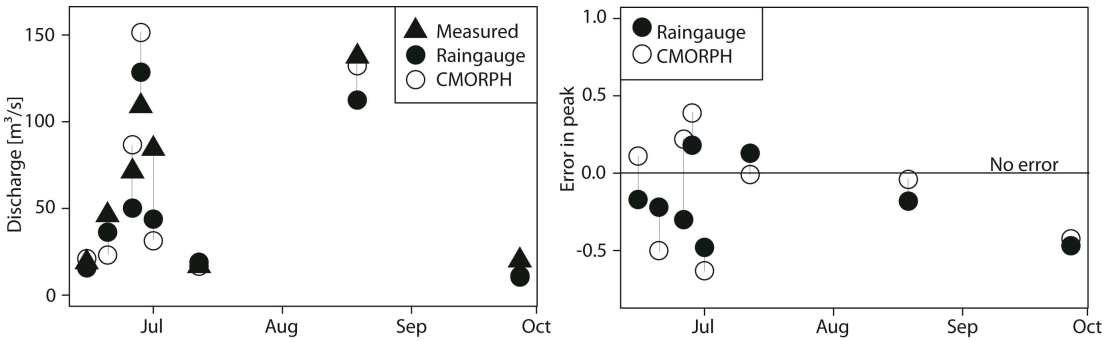

Figure 7.9: Peak magnitudes (left), and error in peaks (right).

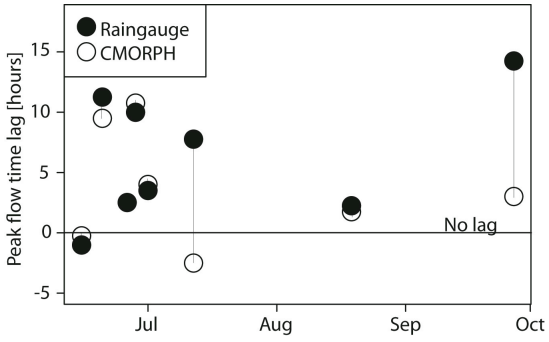

Figure 7.10: Peak flow time lag from the measured peak flow, negative time lag means the peak occurred before the measured peak flow and positive time lag means the peak occurred after the measured peak flow.

7.6 Conclusion

First, the GEOtop model is calibrated and validated for the energy fluxes (sensible heat, latent heat, ground heat, and net radiation), soil temperature and moisture profiles, and streamflows, using SGP97 and SGP99 datasets (see chapters 2 and 3). Using this calibrated model, simulated streamflows are obtained using CMORPH, PERSIANN-CCS, and NEXRAD precipitation data and compared to the measured streamflows and to the simulated streamflows obtained using raingauge measurements. Simulated streamflows from a further CMORPH precipitation product, bias-adjusted by us based on the raingauge measurements, are also tested.

Results show that overall the remotely-sensed precipitation products all produce comparable streamflows, and the streamflows they produce are very similar to the streamflows produced using the raingauge data and to the measured streamflows. However, during one period (Mar-Jun, 2003) CMORPH overestimates streamflows compared to the streamflows produced by the other precipitation products and the measured streamflows. Thus it is concluded that all the above mentioned remotely-sensed precipitation products have value for streamflow simulations at the watershed scale.

8 Conclusion

This study is conducted with two main objectives. First, to study the spatial and temporal variability of near-surface soil moisture derived from two sources of data: estimation obtained from the L-band ESTAR microwave radiometer observation on board aircraft, and simulation obtained from the physically-based GEOtop hydrological model. Furthermore, the spatial soil moisture patterns are characterized at the watershed scale using different geostatistical techniques: different kriging algorithms and conditional Gaussian simulations. Second, to examine the utility of remotely-sensed precipitation products for hydrological simulations. The study region is the Little Washita watershed (583km^2) in the USA, characterized by humid climate and gently rolling topography. The main findings of the study are as follows:

1. GEOtop simulations show that the soil moisture distribution can be approximated by beta distribution consistent with the findings of Famiglietti et al. (1999) who used ground-based measurements of soil moistures during SGP97, while ESTAR estimates show that the soil moisture distribution can be approximated by normal distribution.

2. ESTAR estimates show a linear functional relationship between spatial standard deviation and spatial mean (and also between spatial coefficient of variation and spatial mean), while GEOtop simulations show a downward quadratic relationship.

3. ESTAR estimates did not show any control of river network on the spatial distribution of the near-surface soil moisture, while GEOtop simulations clearly show the control of river network on the spatial distribution of the near-surface soil moisture.

4. ESTAR estimates show zero skewness for the spatial frequency distribution regardless of the spatial mean soil moisture level, whereas GEOtop simulations

show positive skewness at low spatial mean soil moisture, zero skewness at moderate spatial mean soil moisture, and negative skewness at high spatial mean soil moisture.

5. GEOtop simulations and ESTAR estimates give very different spatial patterns of near-surface soil moisture. Spatial patterns derived from GEOtop simulations are in agreement with previous findings obtained from the same study area using ground-based measurements of soil moisture and theoretical model simulations. Therefore, we conclude that GEOtop simulation results are more accurate and that ESTAR estimates are not a reliable source of data for characterizing the spatial variability of near-surface soil moisture.

6. For moderately wet watersheds, the soil moisture variance shows an increasing power law relationship as a function of the support, while for dry watersheds, the soil moisture variance is spatially uniform and is independent of scale.

7. In agreement with Rodriguez-Iturbe et al. (1995), GEOtop simulations show that the spatial correlation of the near-surface soil moisture follows power law decay up to about 1km. For scales larger than 1km, the near-surface soil moisture shows to have multiscaling behaviour.

8. Using gradient, cosine aspect, and all predictors (multivariate) except river network, hydraulic conductivity, and coordinates as predictors for the EDK, clearly show the spatial soil moisture patterns. On the other hand, CGSs show that when using gradient as secondary data to CGSs, reproduce the best patterns. Comparing kriging algorithms with CGSs, CGSs produce spatial soil moisture patterns better than kriging algorithms.

9. All remotely-sensed precipitation products (CMORPH, PERSIANN-CCS, and NEXRAD Stage III) have proved to have considerable value for streamflow simulations at the watershed scale.

9 References

Allen, P.B., and J.W. Naney, 1991. Hydrology of the Little Washita river watershed, Oklahoma: Data and analyses. USDA/ARS-90, USDA Agricultural Research Service, Durant, OK, 74 pp. [Available from National Agricultural Water Quality Laboratory, Durant, OK 74702/]

Bárdossy A., and Lehmann, 1998. Spatial distribution of soil moisture in a small catchment. Part 1: geostatistical analysis. *J. hydrol.*, 206, 1-15.

Barnes, S. L., 1964. A technique for maximizing details in numerical weather map analysis. *J. Appl. Meteor*., 3, 396–409.

Barré de Saint-Venant, A. J. C., 1871. Theorie du mouvement non-permanent des eaux avec application aux crues des rivières et à l'introduction des marees dans leur lit, *C. R. Acad. Sci. Paris* 73, 148–154, 237–240.

Bertoldi, G., 2004. The water and energy balance at watershed scale: a distributed modeling approach. PhD thesis, University of Trento, Italy.

Bertoldi, G., and R. Rigon, 2004. GEOTOP: A hydrological balance model: Technical description and programs guide. Tech. Rep. DICA-04-001, University of Trento.

Blöschl, G., and R. Grayson, 2000. Spatial patterns in catchment hydrology: Observations and modelling. Edited by Rodger Grayson and Gunter Blöschl. Cambridge University press. UK

Bohren, C. F. and B. A. Albrecht, 1998. Atmospheric thermodynamics. Oxford university press, New York, USA.

Brutsaert, W., 1982. Evaporation into the Atmosphere: Theory, Hystory and Applications. Kluver Academic Publisher.

Bushara, A., and R. Rigon, 2010. Surface soil moisture scaling: Model and remote sensing results. *Geophysical Research*. Vol. 12, EGU2010-4877-2.

Bushara, A., M. Gebremichael, T. Over, R. Rigon, and C. D. Peters-Lidard, 2011b. Utility of remotely-sensed precipitation products for hydrological simulations at basin scale. *Geophysical Research*. Vol. 13, EGU2011-7761-4.

Bushara, A., R. Rigon, T. Over, and M. Gebremichael, 2010. Intercomparison between model and ESTAR soil moistures during the Southern Great Plain Hydrology Experiments-1997 and 1999. *Geophysical Research*. Vol. 12, EGU2010-4841-6.

Bushara, A., R. Rigon, T. Over, M. Gebremichael, and C. D. Peters-Lidard, 2011a. Estimates of near-surface soil moistures during SGP97 and SGP99: ESTAR passive microwave radiometer and GEOtop model results. *Geophysical Research*. Vol. 13, EGU2011-10494-1.

Cosh, M. H., and W. Brutsaert, 1999. Aspects of soil moisture variability in the Washita 92 study region. *J Geophys. Res*., 104 (16), 19,751-19,757.

Crosson, W., A. S. Limaye, and C. A. Laymon, 2005. Parameter sensitivity of soil moisture retrivals from airborne L-band radiometer measurements in SMEX02, *IEEE Trans. Geosci. Remote Sens*., 43, 1517-1528.

Dall'Amico, M., 2010. Coupled water and heat transfer in permafrost modeling. PhD thesis, University of Trento, Italy.

Dingman, S. L., 1994. Physical hydrology. Prentice Hall.

Drusch, M., E. F. Wood, and T. J. Jackson, 2001. Vegetation and atmospheric corrections for the soil moisture retrieval from passive microwave remote sensing data: results from the Southern Great Plains Hydrology Experiment 1997, *J. Hydromet.*, 2, 181-192.

Endrizzi, S., 2007. Snow cover modelling at a local and distributed scale over complex terrain. PhD thesis, University of Trento, Italy.

Famiglietti, J. S., D. Ryu, A. A. Berg, M. Rodell, and T. J. Jackson, 2008. Field observations of soil moisture variability across scales, *Water Resour. Res.*, 44, W01423, doi:10.1029/2006WR005804.

Famiglietti, J. S., J. A. Devereaux, C. Laymon, T. Tsegaye, P. R. Houser, T. J. Jackson, S. T. Graham, M. Rodell, and P. J. van Oevelen, 1999. Ground-based investigation of soil moisture variability within remote sensing footprints during the Southern Great Plains 1997 (SGP97) Hydrology Experiment. *Water Resour. Res*., 35, 1839 –1851.

Flores, A. N., V. Y. Ivanov, and D. Entekhabi, 2009. Impact of hillslope-scale organization of topography, soil moisture, soil temperature, and vegetation on modeling surface microwave radiation emission, *IEEE Trans. Geosci. Remote Sens*., 47 (8), 2557-2571.

Fulton, R. A., J. P. Breidenbach, D. Seo, D.A. Miller, and T. O'Bannon, T., 1998. The WSR-88D rainfall algorithm. *Weather Forecast*, 13,377-395.

Garratt, J. R., 1992. The Atmospheric Boundary Layer. Cambridge University Press.

Gebremichael, M., R. Rigon , G. Bertoldi , and T. M. Over, 2009. On the scaling characteristics of observed and simulated spatial soil moisture fields. *Nonlin. Processes Geophys*., 16, 141–150.

Goovaerts. P., 1997. Geostatistics for natural resources evaluation. New York: Oxford university press.

Hengl, T., 2009. A practical guide to geostatistical mapping of environmental variable. The Netherlands.

Hsu, K., X. Gao, S. Sorooshian, and H. V. Gupta, 1997. Precipitation estimation from remotely sensed information using artificial neural networks. *Journal of applied meteorology*, 36,1176-1190

Jackson, T. J., 2002. Soil moisture experiments 2003 (SMEX03). American Geophysical Union, 2002, EOS Trans. Of AGU, 83: F508

Jackson, T. J., and D. M. LeVine, 1996. Mapping of soil moisture using an aircraft-based passive microwave instrument: Algorithm and example. *J. Hydrol*., 184, 85-99.

Jackson, T. J., D. Chen, M. Cosh, F. Li, M. Anderson, C. Walthall, P. Doriaswamy, E.R. Hunt, 2004. Vegetation water content mapping using landsat data derived normalized difference water index for corn and soybeans. *Remote Sens. Environ*, 92, 475-482.

Jackson, T. J., D. M. LeVine, A. Hsu, A. Oldak, P. Starks, C. Swift, J. Isham, and M. Haken, 1999. Soil moisture mapping at regional scales using microwave radiometry: The Southern Great Plains Hydrology Experiment, *IEEE Trans. Geosci. Remote Sens*., 37, 2136– 2151.

Jackson, T. J., D. M. Levine, C. T. Swift, T. J. Schmugge, and F. R. Schiebe, 1995. Large area mapping of soil moisture using the ESTAR passive microwave radiometer in Washita ’92. *Rem. Sens. Environ*., 53, 27-37.

Jackson, T. J., M. S. Moran, P. E. O’Neill, 2008. Introduction to soil moisture experiments 2007 (SMEX04). *Remote sensing of Environment*, 112, 301-303.

Joyce, R., J. E. Janowiak, P. A. Arkin, and P. Xie, 2004. CMORPH: a method that produces global precipitation estimates from passive microwave and infrared data at high spatial and temporal resolution. *J. Hydromet.,* 5(3), 487-503.

LeVine, D. M., A. J. Griffiths, C. T. Swift, and T. J. Jackson, 1994. ESTAR; A synthetic aperture microwave radiometer for remote sensing applications. *Proc. IEEE*, 82, 1787-1801.

Liston, G. E., and K. Elder, 2006. A Meteorological Distribution System for High-Resolution Terrestrial Modeling (MicroMet). *J. Hydromet*., 7, 217-234.

Mohanty, P., 1999. Southern great plains 1997 hydrology experiment (SGP97). Durant OK. Soils Campaign.

Mohr, K. I., J. S. Famiglietti, A. Boone, and P. Starks, 2000. Modeling soil moisture and surface flux variabilitywith an untuned land surface scheme: A case study from the Southern Great Plains 1997 hydrology experiment. *J. Hydromet*., 1, 154-169.

Monin, A. S., and A. M. Obukhov, 1954. Basic laws of turbulent mixing in the ground layer of the atmosphere. Trans. Geophys .Inst. Akad., 151, 163-187.

Mualem, Y., 1976. A new model for predicting the hydraulic conductivity of unsaturated porous media. *Water Resour. Res*., 12, 513–522 .

Nash, J. E. and J. V. Sutcliffe, 1970. River flow forecasting through conceptual models part1- A discussion of principles. *J. Hydrol*., 10 (3), 282 – 290.

Njoku, E. G., P. Ashcroft, T.K. Chan, and L. Li, 2005. Global survey and statistics of radio-frequency interface in AMSR-E, *IEEE Trans. Geosci. Remote Sens*., 43 (5), 938-947.

Pan, F. and C.D. Peters-Lidard, 2010. Inverse method for estimating the spatial variability of soil particle size distribution from observed soil moisture. Journal of hydrologic engineering, doi:10.1061/(ASCE) HE.1943-5584.000074.

Pan, F., and C. D. Peters-Lidard, 2008. On the relationship between mean and variance of soil moisture fields. *JAWRA*, 44 (1): 235-242. DOI: 10.1111/j.1752.

Rawls, W., D. L. Brakensiek, and K. E. Saxton, 1982. Estimation of soil properties. *Trans. ASAE*, 25(5), 1316-1326.

Richards, L. A., 1931. Capillary conduction of liquids through porus mediums. *Physics*., 1, 318-333.

Rigon, R., G. Bertoldi, and T. M. Over, 2006. GEOtop; A distributed hydrological model with coupled water and energy budgets. *J. Hydromet*., 7, 371-388.

Rodriguez-Iturbe, I., G. K. Vogel, R. Rigon, D. Entekhabi, F. Castelli, and A. Rinaldo, 1995. On the spatial organization of soil moisture fields. *Geophys. Res. Lett*., 22(20), 2757 –2760.

Schmugge, T. J., B. J Choudhury, 1981. A comparison of radiative transfer models for predicting the microwave emission from soils. *Radio science*., 16 (5), 927-938.

Simoni S., F. Zanotti, G. Bertoldi , R. Rigon, 2008. Modelling the probability of occurrence of shallow landslides and channelized debris flows using geotop-fs. *Hydrol. Proc*., 22(4), 532-545.

Starks, P. J. and K. S. Humes, Eds, Hydrology Data report, 1996. WASHITA94, NAWQL-96-1, National Agricultural water quality laboratory, USDA-Agricultural Research Service, Durant, Oklahoma.

Tortorelli, R. L. and D. L. Bergman, 1985. Techniques for estimating flood peak discharges for unrequlated streams and streams regulated by small floodwater retarding structures in Oklahoma. U.S. Geological survey, water-resources investigation report 84-4358.

Ulaby, F. T., M. Razani, and M. C. Dobson, 1983. Effects of vegetation cover on the microwave radiometric sensitivity to soil moisture, *IEEE Trans. Geosci. Remote Sens*., 21, 51-61.

Van Genuchten, M. T., 1980. A closed –form equation for predicting the hydraulic conductivity of unsaturated soils. *Soil Sci. Soc. Amer. J*., 44, 892-898.

Vanmarcke, E., 1983. Random fields: Analysis and synthesis. MIT Press, Cambridge MA, USA.

Vereecken, H., J. Maes, J. Feyen, and P. Darius, 1989. Estimating the soil moisture retention characteristics from texture, bulk density and carbon content. *Soil Sci*., 148, 389-403.

Vereecken, H., T. Kamai, T. Harter, R. Kasteel, J. Hopmans, and J. Vanderborght, 2007. Explaining soil moisture variability as a function of mean soil moisture: A stochastic unsaturated flow perspective. *Geophys. Res. Lett*., 34, L22402, doi:10.1029/2007GL031813

Webster, R., M. A. Oliver, 2007. Geostatistics for Environmental Scientists. Wiley, Chichester, UK.

Western, A. W. and G. Blöschl, 1999. On the spatial scaling of soil moisture. *J.Hydrol*., 217, 203-224.

Western, A. W., G. Blöschl , and R. B. Grayson., 1998. Geostatistical characterization of soil moisture patterns in Tarrawarra catchment, *J.hydrol*., 205, 20-37.

Western, A. W., R. B. Grayson, G. Blöschl , G. R. Willgoose, and T. A. McMahon, 1999. Observed spatial organization of soil moisture and its relation to terrain indices, *Water Resour. Res*., 35(3), 797-810.

Yilmaz, M. T., E. R. Hunt Jr, T. J. Jackson, 2008. Remote sensing of vegetation water content from equivalent water thickness using satellite imagery. *Remote Sens. Environ*, doi:10.1016/j.rse.2007.11.01

Zeweldi, D. A. and M. Gebremichael, 2008. Evaluation of CMORPH precipitation products at fine space-time scales. *J. Hydromet*., 10, 300-307.

10 Appendices

Appendix A: Simulated and measured soil temperature profiles during SGP97

The presented stations in this appendix are stations144, and 159.

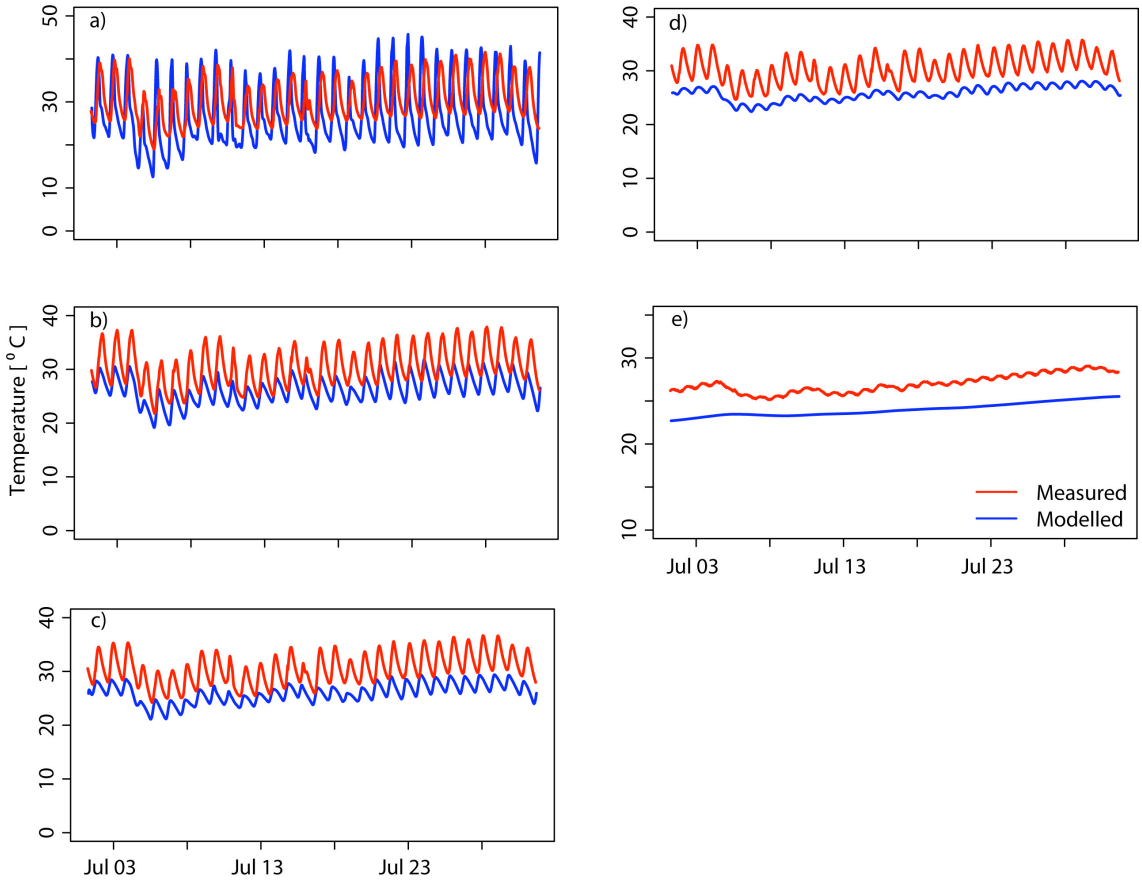

Figure A. 1: Simulated and measured soil temperature profile at station 144, at depths: a) 2.5cm, b) 10cm, c) 15cm, d) 20cm, and e) 60cm from the ground surface.

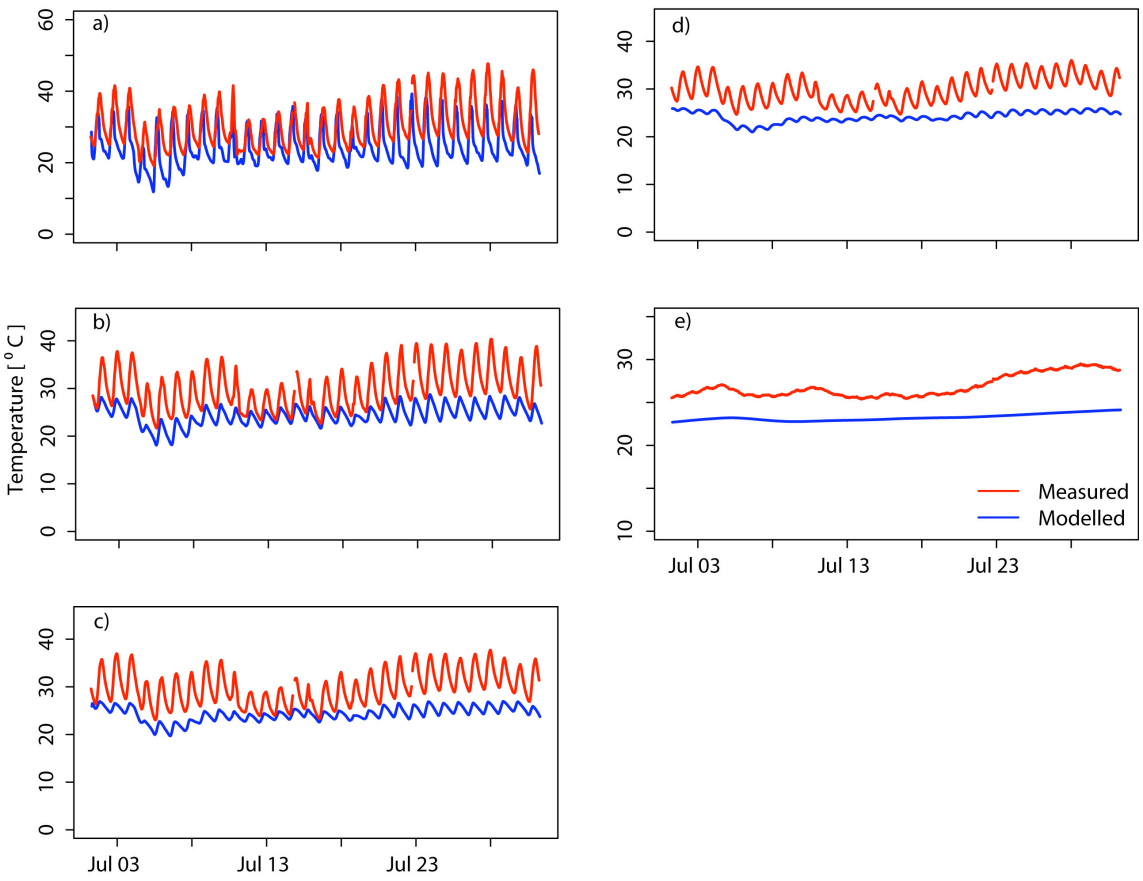

Figure A. 2: Simulated and measured soil temperature profile at station 159, at depths: a) 2.5cm, b) 10cm, c) 15cm, d) 20cm, and e) 60cm from the ground surface.

Appendix B: Comparison of the geostatistical techniques with dynamical modeling

This section presents the variograms of residuals, kriged soil moisture variance, and soil moisture residuals.

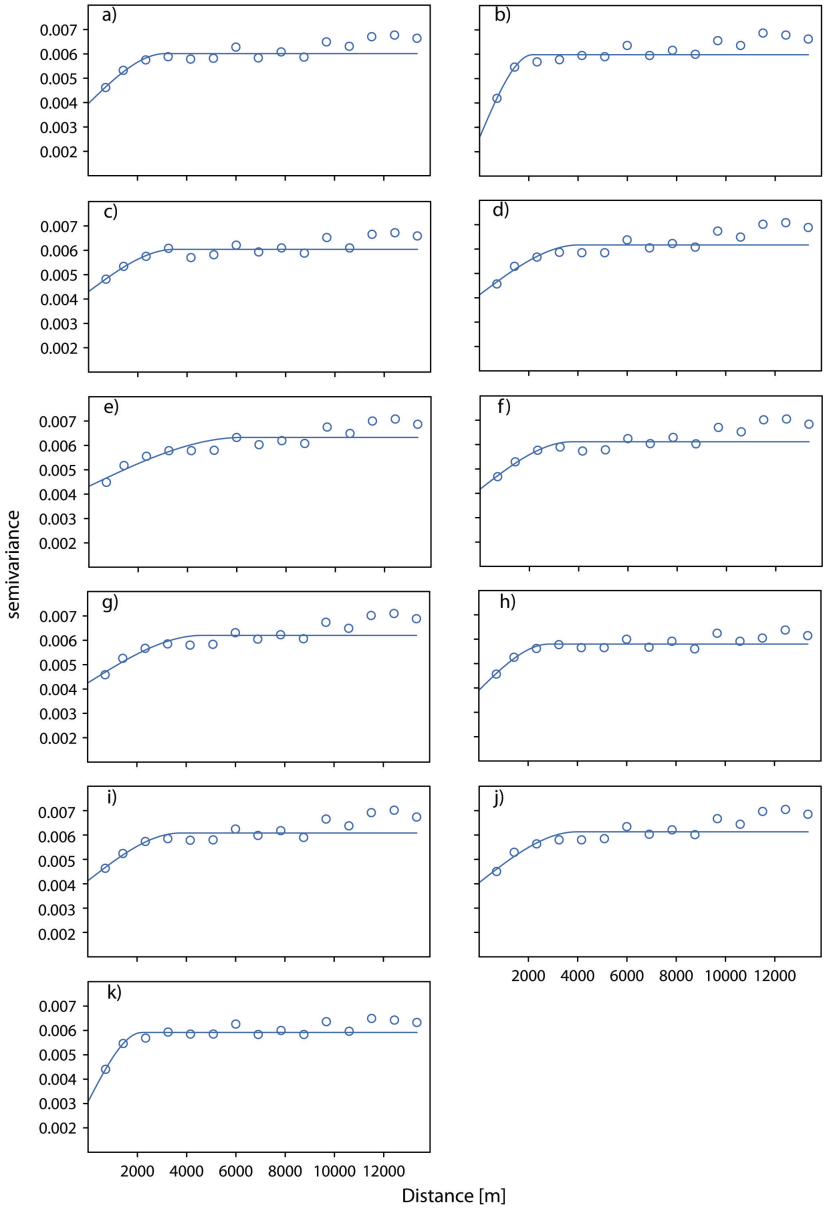

Figure B. 1: Variograms of the residuals fitted with spherical models for the following predictors: a) Elevations, b) Gradient, c) Cosine aspect, d) Wetness index, e) Longitudinal curvature, f) Soil depth, g) Laplacian, h) Coordinates (UK), i) River network, j) Hydraulic conductivity, and k) Combination of gradient and cosine aspect.

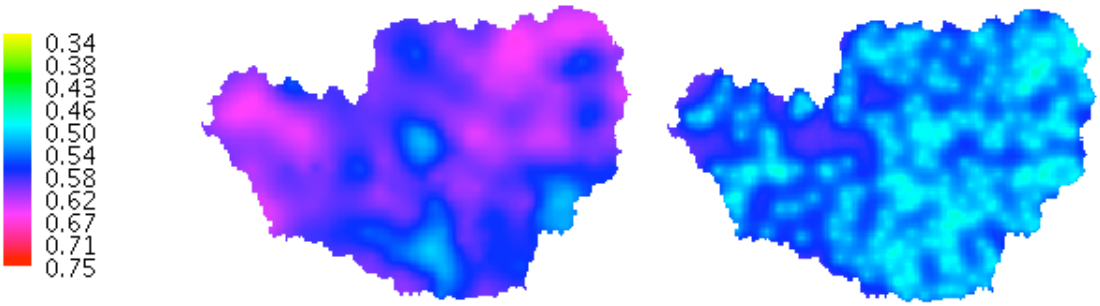

a) OK b) Elevations

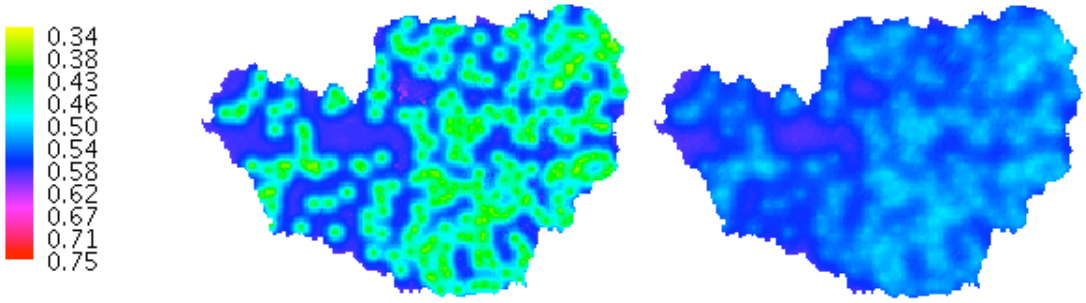

c) Gradient d) Cosine aspect

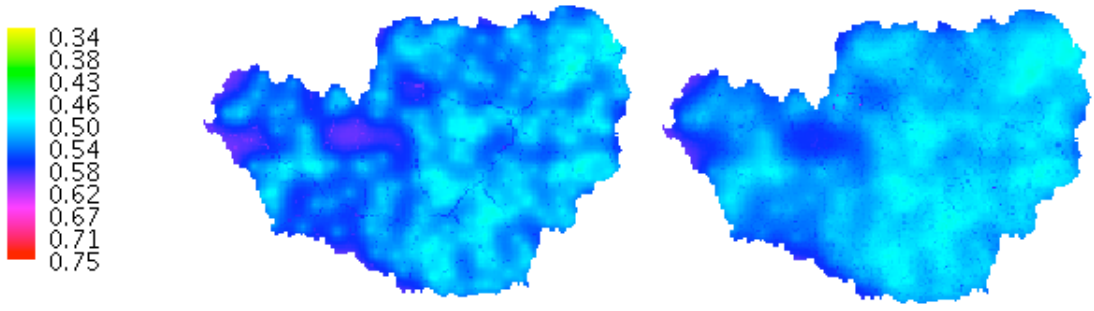

e) Wetness index f) Longitudinal curvature

Figure continues in the next page

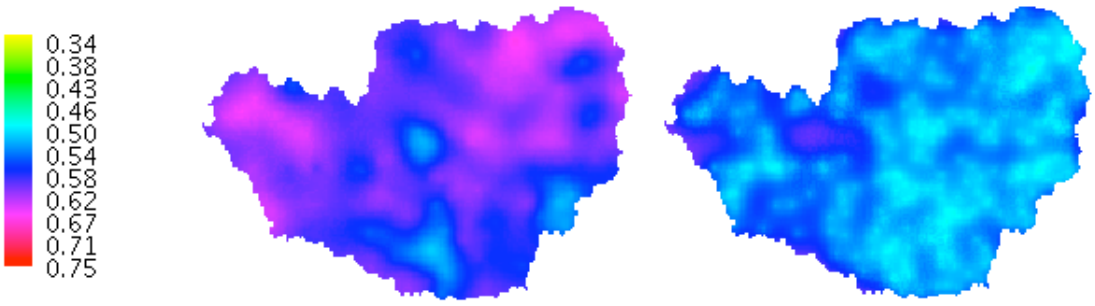

g) Soil depth h) Laplacian

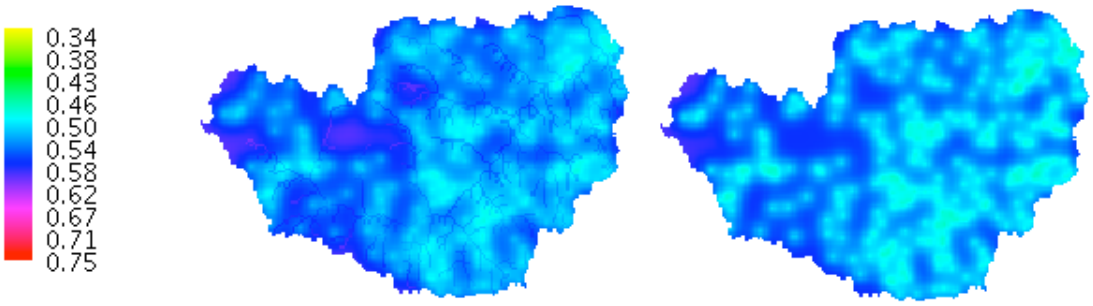

i) River network j) Coordinates

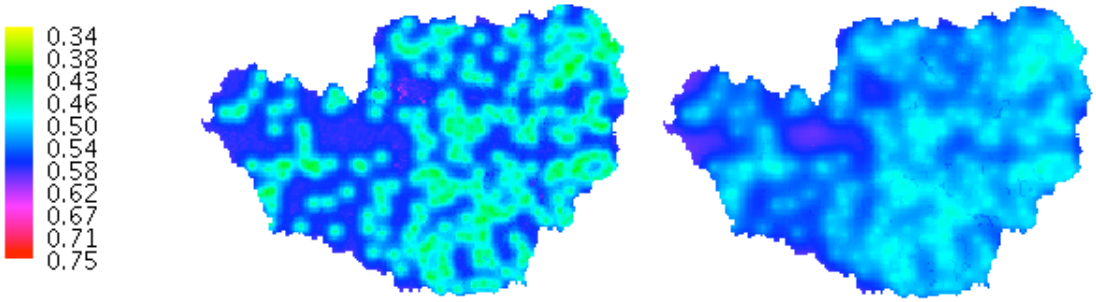

k) Combination of gradient and cosine aspect l) Hydraulic conductivity

Figure B. 2: Soil moisture variance [%] for ordinary kriging and external drift krigings for different predictors.

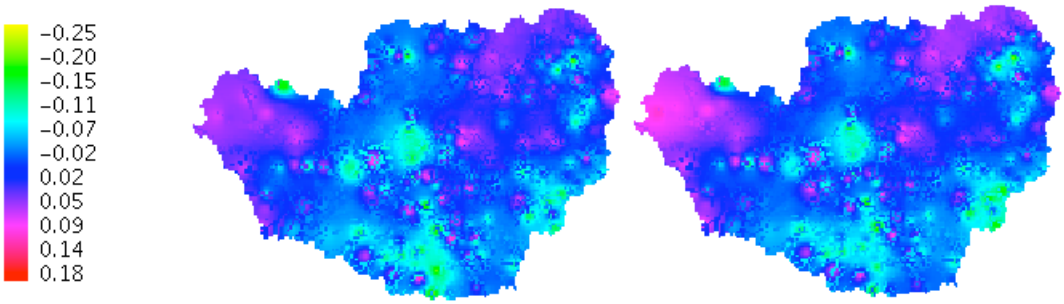

a) OK b) Elevation

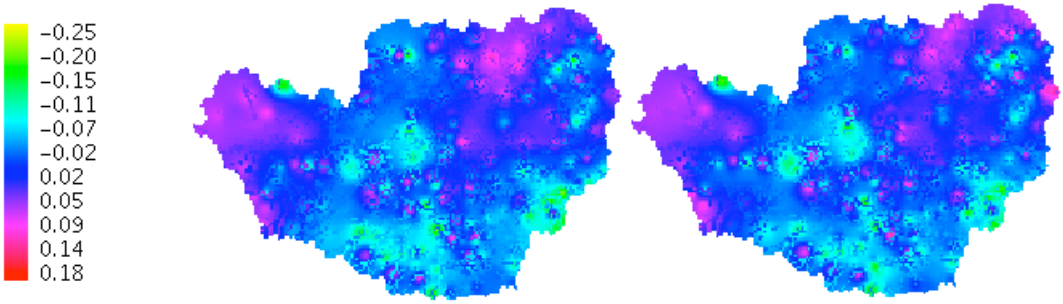

c) Gradient d) Cosine aspect

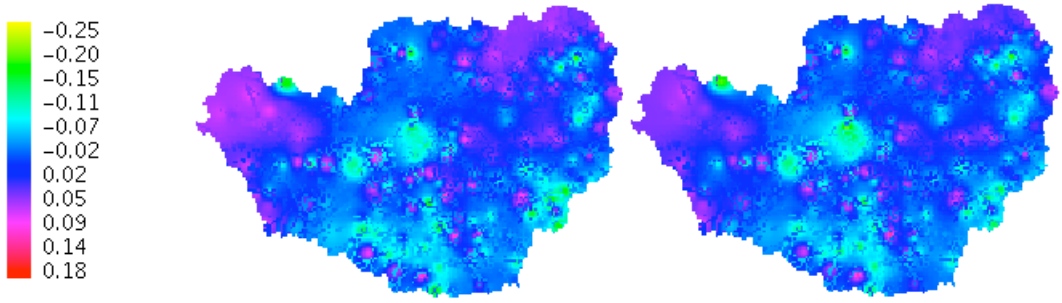

e) Wetness index f) Longitudinal curvature

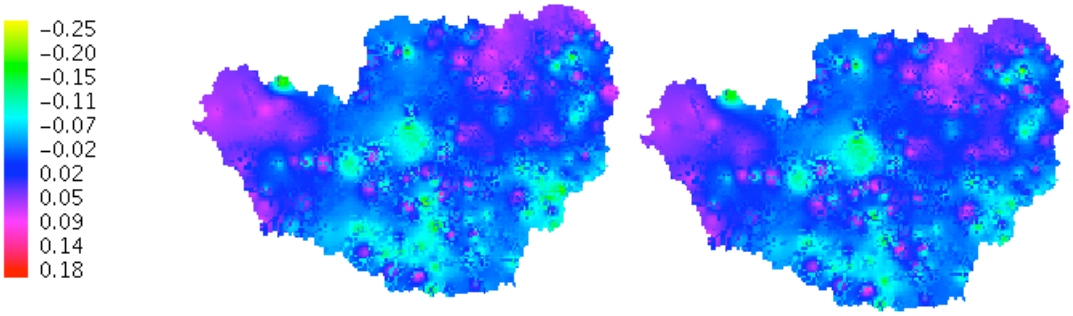

g) Soil depth h) Laplacian

Figure continues in the next page

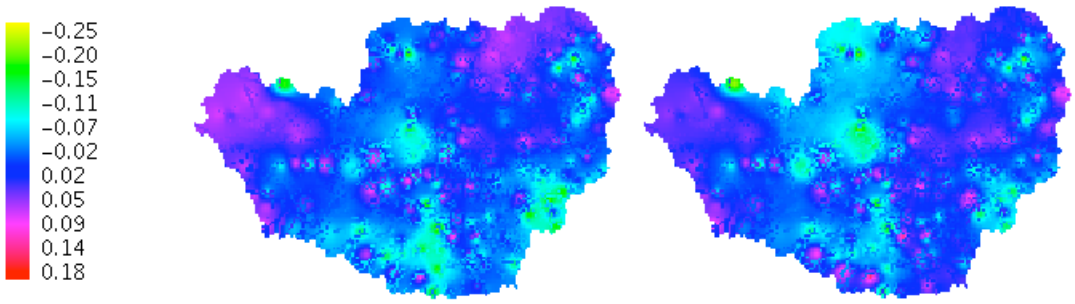

i) River network

j) Coordinates

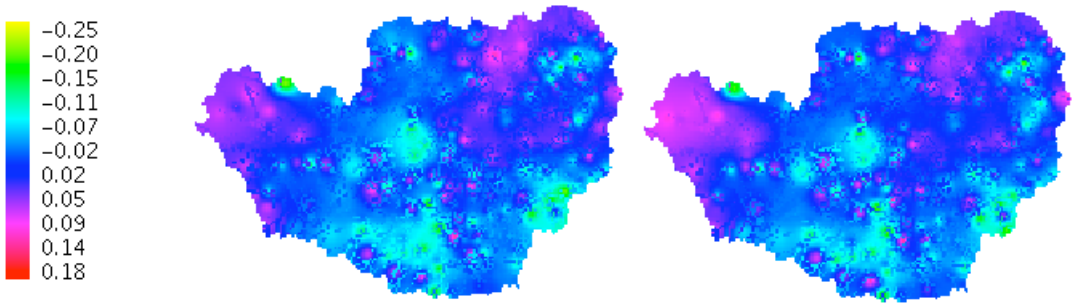

k) Combination of gradient and cosine aspect

l) Hydraulic conductivity

Figure B. 3: Soil moisture residuals from the kriging cross validation, for both ordinary kriging and krigings with external drift using different predictors.